

# REPORT DOCUMENTATION PAGE

Form Approved  
OMB No. 0704-0188

Public reporting burden for this collection of information is estimated to average 1 hour per response, including the time for reviewing instructions, searching existing data sources, gathering and maintaining the data needed, and completing and reviewing the collection of information. Send comments regarding this burden estimate or any other aspect of this collection of information, including suggestions for reducing this burden, to Washington Headquarters Services, Directorate for Information Operations and Reports, 1215 Jefferson Davis Highway, Suite 1204, Arlington, VA 22202-4302, and to the Office of Management and Budget, Paperwork Reduction Project (0704-0188), Washington, DC 20503.

1. AGENCY USE ONLY (Leave blank)		2. REPORT DATE		3. REPORT TYPE AND DATES COVERED FINAL REPORT 01 Feb 92 - 15 Mar 95	
4. TITLE AND SUBTITLE Plasma Microwave Electronics: Studies of High Power Plasma-Loaded Backward Wave Oscillators				5. FUNDING NUMBERS  61102F  2301/ES  AFOSR-TR-95  0535	
6. AUTHOR(S) Professor Granatstein					
7. PERFORMING ORGANIZATION NAME(S) AND ADDRESS(ES) Institute for Plasma Research University of Maryland College Park, MD 20742-3511					
9. SPONSORING / MONITORING AGENCY NAME(S) AND ADDRESS(ES) AFOSR/NE 110 Duncan Avenue Suite B115 Bolling AFB DC 20332-0001				10. SPONSORING / MONITORING AGENCY REPORT NUMBER  F49620-92-J-0152	
11. SUPPLEMENTARY NOTES					
12a. DISTRIBUTION STATEMENT (If appropriate) APPROVED FOR PUBLIC RELEASE: DISTRIBUTION UNLIMITED					
12b. DISTRIBUTION STATEMENT (If appropriate)					
13. ABSTRACT (Maximum 200 words)  SEE FINAL REPORT ABSTRACT  <div data-bbox="966 1281 1356 1585" data-label="Image"> </div> <div data-bbox="1015 1659 1404 1690" data-label="Text"> <p>DTIC QUALITY INSPECTED 5</p> </div>					
14. SUBJECT TERMS				15. NUMBER OF PAGES	
				16. PRICE CODE	
17. SECURITY CLASSIFICATION OF REPORT UNCLASSIFIED		18. SECURITY CLASSIFICATION OF THIS PAGE UNCLASSIFIED		19. SECURITY CLASSIFICATION OF ABSTRACT UNCLASSIFIED	
				20. LIMITATION OF ABSTRACT UNCLASSIFIED	

Final Report

**PLASMA MICROWAVE ELECTRONICS: STUDIES OF  
HIGH POWER PLASMA-LOADED BACKWARD WAVE OSCILLATORS**

For the period February 1, 1994 to March 15, 1995

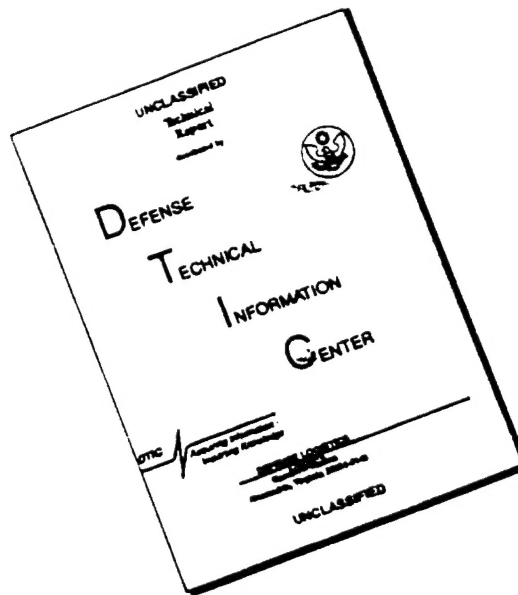
AFOSR Grant Number F49620-92-J-0152

Submitted to  
Air Force Office of Scientific Research

Submitted by  
Electrical Engineering Department  
and  
Institute for Plasma Research  
University of Maryland, College Park, MD 20742-3511

19950824 198

# DISCLAIMER NOTICE



THIS DOCUMENT IS BEST  
QUALITY AVAILABLE. THE COPY  
FURNISHED TO DTIC CONTAINED  
A SIGNIFICANT NUMBER OF  
PAGES WHICH DO NOT  
REPRODUCE LEGIBLY.

## Contents

<b>Executive Summary</b>	<b>1</b>
<b>Papers Published or Submitted for Publication</b>	<b>3</b>
<b>Appendix: Copies of Selected Papers</b>	<b>5</b>

Application For

NEW MAIL ☒

DEAD END ☐

OTHER ☐

2. ☐

3. ☐

4. ☐

5. ☐

6. ☐

7. ☐

8. ☐

9. ☐

10. ☐

11. ☐

12. ☐

13. ☐

14. ☐

15. ☐

16. ☐

17. ☐

18. ☐

19. ☐

20. ☐

21. ☐

22. ☐

23. ☐

24. ☐

25. ☐

26. ☐

27. ☐

28. ☐

29. ☐

30. ☐

31. ☐

32. ☐

33. ☐

34. ☐

35. ☐

36. ☐

37. ☐

38. ☐

39. ☐

40. ☐

41. ☐

42. ☐

43. ☐

44. ☐

45. ☐

46. ☐

47. ☐

48. ☐

49. ☐

50. ☐

51. ☐

52. ☐

53. ☐

54. ☐

55. ☐

56. ☐

57. ☐

58. ☐

59. ☐

60. ☐

61. ☐

62. ☐

63. ☐

64. ☐

65. ☐

66. ☐

67. ☐

68. ☐

69. ☐

70. ☐

71. ☐

72. ☐

73. ☐

74. ☐

75. ☐

76. ☐

77. ☐

78. ☐

79. ☐

80. ☐

81. ☐

82. ☐

83. ☐

84. ☐

85. ☐

86. ☐

87. ☐

88. ☐

89. ☐

90. ☐

91. ☐

92. ☐

93. ☐

94. ☐

95. ☐

96. ☐

97. ☐

98. ☐

99. ☐

100. ☐

101. ☐

102. ☐

103. ☐

104. ☐

105. ☐

106. ☐

107. ☐

108. ☐

109. ☐

110. ☐

111. ☐

112. ☐

113. ☐

114. ☐

115. ☐

116. ☐

117. ☐

118. ☐

119. ☐

120. ☐

121. ☐

122. ☐

123. ☐

124. ☐

125. ☐

126. ☐

127. ☐

128. ☐

129. ☐

130. ☐

131. ☐

132. ☐

133. ☐

134. ☐

135. ☐

136. ☐

137. ☐

138. ☐

139. ☐

140. ☐

141. ☐

142. ☐

143. ☐

144. ☐

145. ☐

146. ☐

147. ☐

148. ☐

149. ☐

150. ☐

151. ☐

152. ☐

153. ☐

154. ☐

155. ☐

156. ☐

157. ☐

158. ☐

159. ☐

160. ☐

161. ☐

162. ☐

163. ☐

164. ☐

165. ☐

166. ☐

167. ☐

168. ☐

169. ☐

170. ☐

171. ☐

172. ☐

173. ☐

174. ☐

175. ☐

176. ☐

177. ☐

178. ☐

179. ☐

180. ☐

181. ☐

182. ☐

183. ☐

184. ☐

185. ☐

186. ☐

187. ☐

188. ☐

189. ☐

190. ☐

191. ☐

192. ☐

193. ☐

194. ☐

195. ☐

196. ☐

197. ☐

198. ☐

199. ☐

200. ☐

201. ☐

202. ☐

203. ☐

204. ☐

205. ☐

206. ☐

207. ☐

208. ☐

209. ☐

210. ☐

211. ☐

212. ☐

213. ☐

214. ☐

215. ☐

216. ☐

217. ☐

218. ☐

219. ☐

220. ☐

221. ☐

222. ☐

223. ☐

224. ☐

225. ☐

226. ☐

227. ☐

228. ☐

229. ☐

230. ☐

231. ☐

232. ☐

233. ☐

234. ☐

235. ☐

236. ☐

237. ☐

238. ☐

239. ☐

240. ☐

241. ☐

242. ☐

243. ☐

244. ☐

245. ☐

246. ☐

247. ☐

248. ☐

249. ☐

250. ☐

251. ☐

252. ☐

253. ☐

254. ☐

255. ☐

256. ☐

257. ☐

258. ☐

259. ☐

260. ☐

261. ☐

262. ☐

263. ☐

264. ☐

265. ☐

266. ☐

267. ☐

268. ☐

269. ☐

270. ☐

271. ☐

272. ☐

273. ☐

274. ☐

275. ☐

276. ☐

277. ☐

278. ☐

279. ☐

280. ☐

281. ☐

282. ☐

283. ☐

284. ☐

285. ☐

286. ☐

287. ☐

288. ☐

289. ☐

290. ☐

291. ☐

292. ☐

293. ☐

294. ☐

295. ☐

296. ☐

297. ☐

298. ☐



## EXECUTIVE SUMMARY

This final report summarizes work done under AFOSR Grant Number F49620-92-J-0152 during the period February 1, 1994 to March 15, 1995 on the three-year research program entitled "Plasma Microwave Electronics: Studies of High Power Plasma-Loaded Backward Wave Oscillators".

The purpose of our research in Plasma Microwave Electronics was to study the fundamental concepts of high power, efficient-microwave generation by using relativistic electron beams in plasma loaded microwave devices. The thrust was to carry out an intensive experimental and theoretical study of improved plasma-filled Backward Wave Oscillators (BWOs) operating at X-Band (frequency of 8.5 GHz) in order to identify the nature of the interaction in the three component system (beam/plasma/e.m. wave) and optimize it. We wished to develop a systematic understanding of the operation of these devices and their scaling with parameters that would allow for the future design of larger diameter overmoded devices to obtain even higher output powers (1-10 GW).

During this reporting period, significant progress was made both in the experimental and theoretical aspects of the program.

A brief summary of the work performed during this reporting period:

- 1) We successfully developed and implemented a technique to determine the reflection and the electromagnetic field profile in an empty cavity which is open, i.e. couples to an antenna.
- 2) A wide band microwave matching section was designed and fabricated. It will be installed between the cavity and the output antenna in order to improve the coupling between the two. This novel matching section is now being tested.
- 3) A novel, long Langmuir probe was developed in order to accurately measure the background plasma density and temperature inside the backward wave oscillator tube. A series of experiments was completed successfully in order to accurately map the density profile in both the axial and radial direction.
- 4) We successfully developed and implemented a microwave technique to measure the dispersion characteristics of smooth and corrugated cavities loaded with time varying, radially inhomogeneous plasma. Using this technique, the dispersion characteristics of  $TM_{01}$  modes in a plasma loaded cavity were measured over a wide range of background plasma densities, from  $10^9$  to  $10^{13} \text{ cm}^{-3}$ .
- 5) A code was developed to analyze the frequency upshifts of  $TM_{0n}$  modes in a corrugated cavities due to the presence of a radially inhomogeneous plasma background.
- 6) We began a series of hot tests of an improved plasma loaded backward wave oscillator. The improvements include: a) preventing microwave breakdown near the collector, which can cause microwave pulse shortening, using an improved output section; b) novel techniques for plasma injection and filling of the tube; and c) electron gun protection against adverse plasma effects.

- 7) We developed the nonlinear model of the parametric excitation of plasma mode in the relativistic BWO. This model was used to compare with experimental results. Particular attention was paid to confirmation of the parametric decay hypothesis. Predictions of the model with regard to the output spectrum of the device, the excitation of plasma waves, and the dependence on plasma density were determined. The development of the model proceeded through stages. Particle methods were introduced. A code was developed in which the plasma electron motion is one-dimensional owing to the strong applied magnetic field. The radiation is still modeled by an envelope equation allowing the code to run much faster than a full PIC simulation. Results of this code indicated that parametric decay was possible in principle, but not likely for the parameters of the experiments.
- 8) We undertook an extensive comparison of the results of model simulations of the type discussed above, and full PIC calculations using MAGIC. This work is ongoing. We have developed numerical tools which extract the EM fields from MAGIC and integrate the orbits of beam electrons in these fields. This effort will ultimately determine the range of validity of various models of BWO operation.

#### Publications and Conference Proceedings:

- 1 invited paper
- 5 papers in refereed journals
- 7 papers at scientific meetings
- 1 article in conference proceedings

#### Student Involvement

The following students were engaged in the research: Susanne Miller participated in the theoretical work while James Weaver and Satoru Kobayashi participate in the experimental work.

## Papers Published or Submitted for Publication (November 1993–May 1995)

### Invited Papers

1. Can Plasma Microwave Devices Revitalize and Broaden the Scientific and Technical Base of Microwave Devices. Y. Carmel, T. Antonsen, B. Levush, G. Nusinovich, W.W. Destler, V.L. Granatstein, IEEE International Conference on Plasma Science, June 6–8, 1994, Santa Fe, NM.

### Articles in Refereed Journals

1. Analysis of the Electromagnetic Waves in an Overmoded Finite Length Slow Wave Structure. M. Amin, K. Ogura, H. Kitamura, K. Minami, T. Watanabe, Y. Carmel, W. Main, J. Weaver, W.W. Destler, V. L. Granatstein, IEEE Trans. on Microwave Theory and Techniques **43**, 4 (1995), pp. 815-822.
2. Starting Energy and Current for a Large Diameter Finite Length Backward Wave Oscillator Operated at the Fundamental Mode. K. Minami, K. Ogura, Y. Aiba, M. Amin, X. Zheng, T. Watanabe, Y. Carmel, W. Main, J. Weaver, W.W. Destler, V.L. Granatstein, IEEE Trans. on Microwave Theory and Techniques **43**, 4 (1995) pp. 124-132.
3. The Electromagnetic Properties of Open and Closed Overmoded Slow Wave Resonators for Interaction with Relativistic Electron Beams. W. Main, Y. Carmel, K. Ogura, G. Nusinovich, J. Tate, J. Rodgers, A. Bromborsky, S. Watanabe, M. Amin, K. Minami, W.W. Destler, V.L. Granatstein, IEEE Trans. Plasma Science, Special Issue on High Power Microwave Generation **22**, 5 (1994), pp. 556-577.
4. Theory of Relativistic Backward Wave Oscillators Operating Near Cutoff. S.M. Miller, T.M. Antonsen, Jr., A. Bromborsky, D.K. Abe, Y. Carmel, Physics of Plasmas **1**, 3 (1994) pp. 730-740.
5. Parametric Effect of a Spatially Periodic Voltage Depression on the Operation of Cerenkov Sources of Electromagnetic Radiation. G. Nusinovich, A. Vlasov, Phys. Plasmas **1**, 3 (1994) pp. 774-779.

### Articles in Conference Proceedings

1. High Efficiency Relativistic BWO: Theory and Design. B. Levush, T. Antonsen, A. Vlasov, G. Nusinovich, Y. Carmel, V.L. Granatstein, W.W. Destler, A. Bromborsky, A. Schezinger, D.K. Abe, 7th National Conference on High Power Microwave Technology, Naval Post-Graduate School, Monterrey, CA, October 1994.

### Presentations at Scientific Meetings

1. Characterization of the Plasma Column Used in Studies of a Plasma-Loaded Relativistic Backward Wave Oscillator. J. Weaver, S. Kobayashi, A. Shkuvarunets, Y. Carmel, J. Rodgers, W. W. Destler, and V. L. Granatstein. IEEE Conference on Plasma Science, June 5-8, 1995, Madison, WI.
2. Studies of Low Q Slow Wave Structures for Relativistic Backward Wave Devices. J. Weaver, S. Kobayashi, Y. Carmel, W. Main, G. Nusinovich, K. Ogura, M.R. Amin, S. Wanatabe, K. Minami, J.P. Tate, A. Bromborsky, W.W. Destler, V.L. Granatstein, IEEE Conference on Plasma Science, June 6-8, 1994, Sante Fe, NM.
3. Recent Results from the Plasma Microwave Electronics Program at the University of Maryland. Y. Carmel, T.M. Antonsen, J. Rodgers, B. Levush, G. Nusinovich, J. Weaver, S. Miller, S. Kobayashi, W.W. Destler, V.L. Granatstein, IEEE Conference on Plasma Science, June 6-8, 1994, Sante Fe, NM.
4. Starting Energy and Current for an Overmoded Finite Length Backward Wave Oscillator. K. Minami, K. Ogura, Y. Aiba, M.R. Amin, T. Wanatabe, Y. Carmel, W.W. Destler, V.L. Granatstein, IEEE Conference on Plasma Science, June 6-8, 1994, Sante Fe, NM.
5. Introduction of High Power Microwave with Plasma in a Corrugated Wall Waveguide. K. Minami, S. Sugawara, Y. Naito, K. Ogura, Y. Carmel, W.W. Destler, V.L. Granatstein, IEEE Conference on Plasma Science, June 6-8, 1994, Sante Fe, NM.
6. Experimental Demonstration of a High Power Slow Wave Electron Cyclotron Maser Utilizing Corrugated Metal Structures. K. Minami, K. Ogura, K. Kurashina, W. Kim, Y. Carmel, W.W. Destler, V.L. Granatstein, IEEE Conference on Plasma Science, June 6-8, 1994, Sante Fe, NM.
7. Demonstration of High Power Microwave Source Utilizing a Large Diameter Corrugated Open Resonator. K. Ogura, K. Minami, X. Zhang, M.R. Amin, T. Wanatabe, S. Sugite, Y. Carmel, 19th International Conference on Infrared and Millimeter Waves, October 17-21, 1994, Sendai, Japan.
8. Raman Decay in Plasma Filled Backward Wave Oscillators, S.M. Miller, T.M. Antonsen Jr., B. Levush, Y. Carmel, 35th Annual Meeting of the Division of Plasma Physics, November 1-5, 1993, St. Louis, MO.

## APPENDIX

### COPIES OF SELECTED PAPERS

1. The Electromagnetic Properties of Open and Closed Overmoded Slow Wave Resonators for Interaction with Relativistic Electron Beams. W. Main, Y. Carmel, K. Ogura, G. Nusinovich, J. Tate, J. Rodgers, A. Bromborsky, S. Watanabe, M. Amin, K. Minami, W.W. Destler, V.L. Granatstein, IEEE Trans. Plasma Science, Special Issue on High Power Microwave Generation **22**, 5 (1994), pp. 556-577.
2. Theory of Relativistic Backward Wave Oscillators Operating Near Cutoff. S.M. Miller, T.M. Antonsen, Jr., A. Bromborsky, D.K. Abe, Y. Carmel, Physics of Plasmas **1**, 3 (1994) pp. 730-740.
3. Parametric Effect of a Spatially Periodic Voltage Depression on the Operation of Cerenkov Sources of Electromagnetic Radiation. G. Nusinovich, A. Vlasov, Phys. Plasmas **1**, 3 (1994) pp. 774-779.
4. Characterization of the Plasma Column Used in Studies of a Plasma-Loaded Relativistic Backward Wave Oscillator. J. Weaver, S. Kobayashi, A. Shkuvarunets, Y. Carmel, J. Rodgers, W. W. Destler, and V. L. Granatstein. IEEE Conference on Plasma Science, June 5-8, 1995, Madison, WI.
5. Starting Energy and Current for a Large Diameter Finite Length Backward Wave Oscillator Operated at the Fundamental Mode. K. Minami, K. Ogura, Y. Aiba, M. Amin, X. Zheng, T. Watanabe, Y. Carmel, W. Main, J. Weaver, W.W. Destler, V.L. Granatstein, IEEE Trans. on Microwave Theory and Techniques **43**, 4 (1995) pp. 124-132.

# Electromagnetic Properties of Open and Closed Overmoded Slow-Wave Resonators for Interaction with Relativistic Electron Beams

W. Main, Y. Carmel, *Senior Member, IEEE*, K. Ogura, J. Weaver, G. S. Nusinovich, *Senior Member, IEEE*, S. Kobayashi, J. P. Tate, J. Rodgers, A. Bromborsky, *Member, IEEE*, S. Watanabe, M. R. Amin, K. Minami, W. W. Destler, *Fellow, IEEE*, and V. L. Granatstein, *Fellow, IEEE*

**Abstract**—Specific slow wave structures are needed in order to produce coherent Cherenkov radiation in overmoded relativistic generators. The electromagnetic characteristics of such slow wave, resonant, finite length structures commonly used in relativistic backward wave oscillators have been studied both experimentally and theoretically. In experiments, perturbation techniques were used to study both the fundamental and higher order symmetric transverse magnetic (TM) modes. Finite length effects lead to end reflections and quantization of the wave number. The effects of end reflections in open slow wave structures were found from the spectral broadening of the discrete resonances of the different axial modes. The measured axial and radial field distributions are in excellent agreement with the results of a 2-D code developed for the calculation of the fields in these structures.

**Index Terms**— Periodic structures, slow waves, dispersion curve, resonators.

## I. INTRODUCTION

VARIOUS electrodynamic structures capable of supporting the propagation of slow electromagnetic waves are widely used for microwave generation and for the acceleration of charged particles. These slow-wave structures are designed to match the phase velocity of the propagating electromagnetic waves to the speed of electrons in the same structure in order to facilitate an effective beam/wave interaction. For interaction with weakly relativistic electron beams it is therefore necessary to slow down the wave's phase velocity significantly while for interaction with relativistic electron beams the phase velocity required is only slightly smaller than the speed of light. The electromagnetic properties of structures with very different phase velocities, obviously, would also be expected to be very different. Therefore, in spite of the availability of detailed studies of structures intended for operation in conventional, weakly relativistic microwave tubes [1], [2] there is still a need

for more detailed studies of slow wave structures intended for operation with relativistic electron beams.

A second motivation for the work presented in this paper is the recent interest that has developed around the generation of high power microwave radiation in devices employing overmoded slow wave structures. Despite traditional concerns about mode competition in overmoded devices, recent experiments [3], [4] have shown that efficient, high power operation can be achieved in such devices operating in a single mode. The present study, therefore, has been undertaken in part to accurately determine the electromagnetic characteristics of overmoded slow wave structures to aid in the linear and nonlinear analysis of advanced microwave sources employing such circuits.

Finally, such issues as finite length of the periodic structures and finite reflections at both ends should be studied in more detail. For example, in a finite length structure the axial wave numbers of the electromagnetic modes are quantized affecting the spectral characteristics of device operation. Also, the amount of reflection at both ends of the structure affects the quality factor of each of the quantized axial modes in the multiple resonance "slow-wave" cavity in a unique way. This, in turn, strongly influences the interaction of the electrons with the electromagnetic waves associated with each mode. Especially important is the effect of reflections on the non-stationary operation of short pulse relativistic backward wave oscillators (BWO's) [5], [6].

Perturbation techniques are available for measuring the spatial distribution of fields in resonant cavities [1], [2]. These techniques have been primarily applied to the fundamental modes in accelerator cavities, which are electromagnetically closed (shorted) at both ends and typically have quality factors (Q) over 4000. In contrast, the Q factors of spatially periodic slow-wave structures intended for operation with intense relativistic electron beams are much lower ( $\sim$  several hundred) and the electromagnetic properties of these structures have not been studied in detail until recently [7]–[11]. Due to the high fields achieved in these devices, microwave power is usually extracted via open-ended matching sections that lower the total Q and can cause asymmetric axial field distributions. To accurately model this type of device it is important to know the reflection coefficient at the end of the structure and the field

Manuscript received September 30, 1993; revised May 30, 1994. Part of this work was presented as an invited talk at the IEEE ICOPS 1993. This work was supported in part by the Air Force Office of Scientific Research and the Army Research Laboratory.

The authors are with the Institute for Plasma Research, University of Maryland, College Park, Maryland 20742-3511 USA, except as noted:

W. Main is with ACCURAY, Inc., Santa Clara, CA USA.

K. Ogura, S. Watanabe, M.R. Amin, and K. Minami are with Niigata University, Niigata City, Japan.

A. Bromborsky is with Army Research Laboratories, Adelphi, MD USA  
IEEE Log Number 9404603D.



distribution. To date, parameters have usually been obtained through numerical calculations, which are more complicated as the Q-factor decreases. In this study we present experimental methods for determining these parameters and for checking the results of numerical calculations.

To properly address these issues we have developed a formalism describing the fields inside a finite length, spatially periodic structure and methods for measuring the fields and end reflections. For this study we used a periodic structure in the shape of a cylindrical waveguide with a sinusoidally varying conducting wall. A schematic diagram of this apparatus appears in Fig. 1(a). The dispersion diagram for the first six symmetric transverse magnetic modes in an infinitely long slow wave structure with the same dimensions is shown in Fig. 1(b). The periodic nature of the structure leads to a band pass characteristic of each mode. The passbands are given an index, starting with 1 for the lowest and increasing by 1 for each subsequent passband. Thus, the first is referred to as  $TM_{01}$ , the second as  $TM_{02}$ , and the  $n$ th as  $TM_{0n}$ . In this paper, we have studied the fundamental ( $TM_{01}$ ) and two higher order ( $TM_{02}$ ,  $TM_{03}$ ) transverse magnetic modes in a spatially periodic, sinusoidally corrugated structure of finite length. Preliminary data for  $TM_{04}$  is also available.

This paper is organized as follows. In Section II we discuss the formation of axial modes associated with each transverse mode in a finite length periodic resonator and the relation of these modes to the dispersion diagram of the corresponding infinite length structure. This dispersion diagram is useful for modeling some aspects of BWO operation, such as the relation of beam energy to the approximate operating frequency. To model the more complex nonlinear behavior, it is necessary to numerically simulate the operation of the BWO. For that purpose one needs to know the amplitude and phase of the reflection coefficient from the structure ends, as well as the beam-wave coupling coefficient. The coupling coefficient can only be calculated once the field profile in the structure is known. In Section III we describe how the electromagnetic fields are calculated by expanding the fields in a spatially harmonic series. In Section IV we show how the resonant frequencies as well as the radial field profile associated with each axial mode of the closed slow-wave structure was measured for the three TM modes considered. In Section V we describe how we experimentally determined the reflection coefficient at the open end of our slow-wave resonator. This was done by measuring the spectral width of each resonance, which broadens as the end of the slow-wave resonator is opened. We present both experimental and numerical results for the end reflection. Section VI summarizes our work and describes our latest efforts to increase the accuracy of our results. Possible extensions of these techniques to plasma filled systems are also discussed. Two appendices are also attached to explain the calculation of the reflection coefficient and the analytic model used for the closed cavity quality factor.

## II. AXIAL MODES IN A FINITE LENGTH SLOW-WAVE CAVITY

The dispersion characteristics of electromagnetic modes in an infinitely long spatially periodic structure are determined

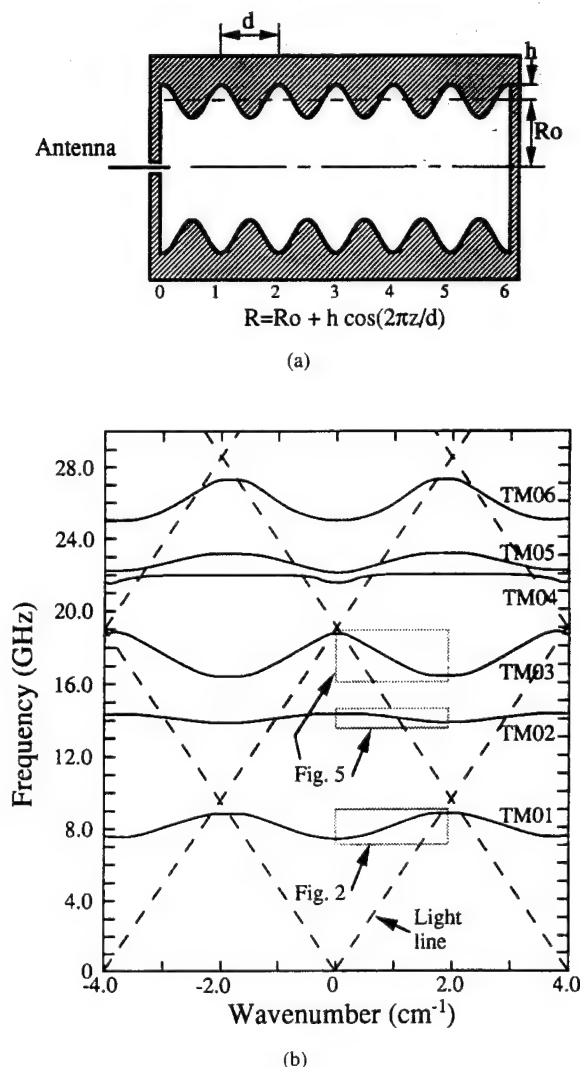


Fig. 1. (a) Schematic diagram of a spatially periodic (corrugated wall) structure shorted at both ends. (b) The calculated dispersion diagram for six symmetric transverse magnetic ( $TM_{0s}$ ) modes in an infinitely long, spatially periodic structure of Fig. 1(a).

only by the geometry of the conducting walls. A finite length structure, however, can be described by a simple dispersion relation only when it is well matched at both ends (i.e., no reflections). Structures used in relativistic BWO's are usually not well matched. First, relativistic BWO's utilize a strong reflection at the entrance of the structure to prevent microwave propagation into the diode region [7], [8], [10], [11]. At the output end of the structure, part of the microwave radiation is reflected and part transmitted. As a result of these reflections a standing wave pattern is created leading to a spectrum of axial modes. This effect was studied in [5] and [6].

Any spatially periodic structure with end reflections containing  $N$  periods will support  $N + 1$  different axial modes for each transverse mode [12]. Each of these axial modes is characterized by a discrete frequency ( $f_r$ ) and a discrete axial wave number ( $\beta_r$ ), which are located on the dispersion curve of the same transverse mode in an otherwise identical structure of infinite length. As a consequence of the spatial periodicity of the structure, traveling waves can be presented as a super

position of spatial harmonics. The standing wave is formed by a pair of such traveling waves propagating in opposite directions. As an example, the measured frequencies and wave numbers of the seven axial modes associated with the lowest order symmetric transverse magnetic mode ( $TM_{01}$ ) of the six period slow-wave structure of Fig. 1 are shown in Fig. 2(a). In Fig. 2(a) we show, for simplicity, only axial wave numbers for the forward wave in the zero's Brillouin zone. Bear in mind that for a given frequency, the total field contains a set of axial wave numbers corresponding to different spatial harmonics. Throughout this paper, resonance plots will be presented as frequency (in GHz) versus the normalized wave number,  $\beta d$ , which is equal to the phase advance per structure period. Here  $\beta$  is the axial wave number and  $d$  is the length of the structure period. The structure wall radius is given by

$$R_w = R_0 + h \cos(2\pi z/d) \quad (1)$$

where  $R_0$  is the average radius and  $h$  is the amplitude of the wall corrugations. Even though all seven axial modes shown belong to the same transverse magnetic mode ( $TM_{01}$ ), they are characterized by completely different patterns of field lines. As an example, the calculated electric field line pattern of two of the seven axial modes in the slow-wave structure of Fig. 1 are shown in Fig. 2(b). The technique used to calculate these patterns will be described in Section III.

A few features of finite length structures follow from Fig. 2(a), which describes an X-band slow-wave structure having a passband from 7.4 to 8.7 GHz for the fundamental symmetric transverse magnetic ( $TM_{01}$ ) mode. First, the discrete axial modes which are equally spaced in wave number are not equally spaced in frequency within the structure passband. The mode separation varies between 0.05 and 0.25 GHz for the structure studied in this work. Second, the spectral resonance width (and thus the quality factor) of each of the axial modes is different since the group velocity of the electromagnetic wave varies. This feature is used to calculate the end reflection of shorted and open slow-wave structures, as will be shown in Section V.

In addition to the dispersion curve, Fig. 2(a) shows all seven  $TM_{01}$  resonance peaks for a closed six-period slow-wave cavity as measured with a microwave network analyzer. For a structure with  $N$  periods of length  $d$  the resonance condition can be stated as [12]

$$Nd = (n_r/2)(2\pi/\beta) \quad (2)$$

where  $n_r$  is the number of half wavelengths along the axis of the structure and  $(2\pi/\beta)$  is the axial wave length. The resonant axial wave number  $\beta_r$  is then found from  $n_r$  using the above equation. Points on the dispersion curve are found by recording the resonant frequencies  $f_r$  and associated axial wave numbers  $\beta_r$  for the set of axial modes associated with each transverse magnetic (TM) mode. The complete dispersion relation can then be constructed from these discrete points [13] or calculated, as will be shown in Section III. Measuring the

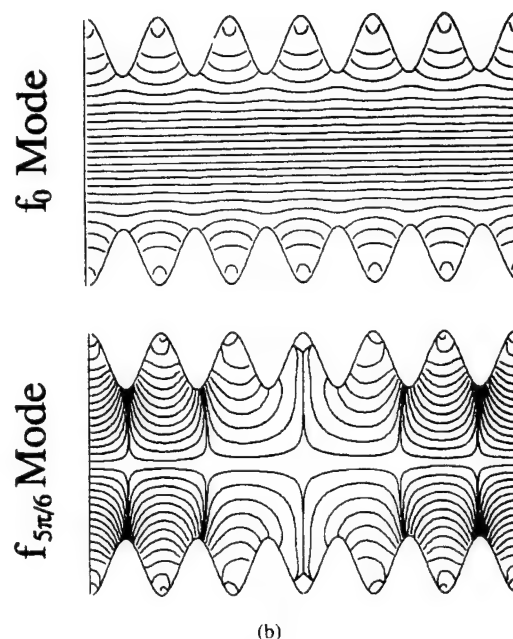
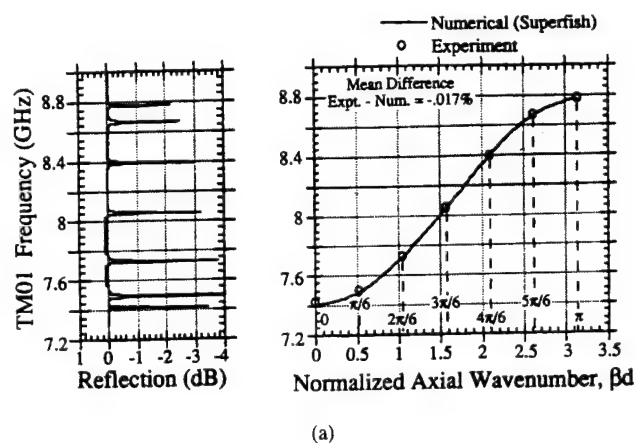


Fig. 2. (a) The dispersion diagram of an X-band slow wave structure having a passband of 7.4 to 8.7 GHz for the  $TM_{01}$  mode as calculated by Superfish, presented as a smooth line. Only half of the first Brillouin zone is shown. Also shown is the measured reflection data and all seven  $TM_{01}$  resonance peaks of the closed six period slow wave cavity (open circles). (b) The electric field line pattern associated with two of the seven axial modes ( $0, 5\pi/6$ ).

dispersion relation is therefore reduced to finding the set of resonant frequencies and axial wave numbers ( $f_r$ ,  $\beta_r$ ) for the desired TM mode. In practice it is much easier to find the frequencies than the wave numbers. For a spatially periodic resonator excited by an ideal mode launcher, the  $N + 1$  axial modes associated with a single TM mode should be equally spaced in wave number. Thus if the dispersion curve,  $f(\beta)$ , is known to be an increasing or decreasing monotonic function of the wave number over one Brillouin zone, then it is necessary to measure only the resonance frequencies. If the dispersion relation is non-monotonic, then it is necessary to measure both  $f$  and  $\beta$  to determine  $f(\beta)$ . In this study we consider the fundamental ( $TM_{01}$ ) and the next two higher order ( $TM_{02}$  and  $TM_{03}$ ) transverse modes, which are monotonic; however, the techniques presented also apply to nonmonotonic modes. In Section IV we show how these resonances were measured.



### III. NUMERICAL MODELING OF THE SLOW-WAVE STRUCTURE FIELDS

#### A. Field model

The first step in the simulation of overmoded slow wave structures is to find a way to accurately and efficiently calculate the electromagnetic fields in the structure. As higher modes are considered, these calculations become more complex and it becomes also important to experimentally verify the results. Here we present a technique which shows good agreement with experimental measurements for closed, spatially periodic structures at least up to the  $TM_{03}$  mode.

We use a model [14]–[16] in which the fields are expanded in a spatially harmonic series, according to Floquet's theorem. Solving the dispersion relation for the sinusoidal boundary of the slow-wave structure given by (1) gives the expansion coefficients. Using Maxwell's equation, we get the following expressions for the electromagnetic field components,  $E_z$ ,  $E_r$ , and  $H_\phi$ ,

$$E_z(r, z, t) = \sum_{n=-\infty}^{\infty} A_n J_0\left(\frac{\chi_n}{R_0} r\right) e^{i(\beta_n z - \omega t)} \quad (3)$$

$$E_r(r, z, t) = -iR_0 \sum_{n=-\infty}^{\infty} \frac{A_n \beta_n}{\chi_n} J_1\left(\frac{\chi_n}{R_0} r\right) e^{i(\beta_n z - \omega t)} \quad (4)$$

$$H_\phi(r, z, t) = -i\epsilon_0 \omega R_0 \sum_{n=-\infty}^{\infty} \frac{A_n}{\chi_n} J_1\left(\frac{\chi_n}{R_0} r\right) e^{i(\beta_n z - \omega t)} \quad (5)$$

where  $J_0$  and  $J_1$  are the Bessel functions of the first kind of order 0 and 1, respectively,

$$\chi_n^2 = R_0^2 (\omega^2/c^2 - \beta_n^2) \quad (6)$$

where  $\beta_n = \beta + n2\pi/d$  is an integer and  $c$  is the velocity of light in vacuum. The dispersion relation is derived from the boundary condition [17] requiring that the tangential electric field is zero at the wall  $r = R(z)$ ,

$$E_t(R) \propto E_z(R) + E_r(R) dR/dz = 0. \quad (7)$$

The spatial Fourier transform of (7) can be expressed as:

$$D \cdot A = 0 \quad (8)$$

where  $A$  is a coefficient vector in (3)–(5) and  $D$  is a matrix of infinite order. The dispersion relation is the non-trivial solution of (8) and is given by

$$\det[D(\beta, \omega)] = 0. \quad (9)$$

In the case of a finite length, slow-wave structure, the additional boundary conditions at both ends ( $z = 0$  and  $z = L$ ) must be satisfied [18]. A wave propagating forward along the  $z$ -axis,  $F$ , reflects at  $z = L$  and becomes a backward propagating wave  $B$ . Fig. 3(a) illustrates this process, and

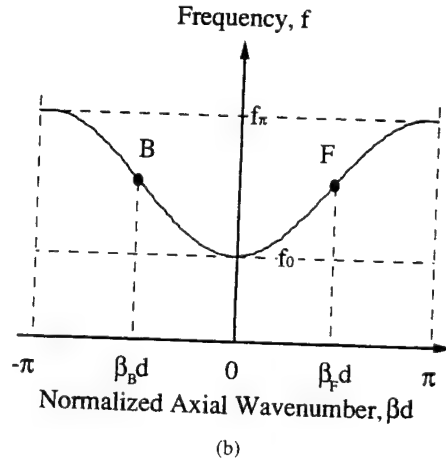
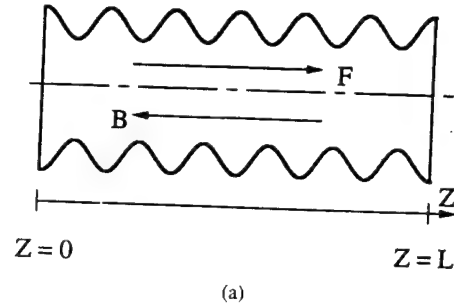


Fig. 3. (a) A wave propagating forward along the  $z$ -axis,  $F$ , reflects at  $z = L$  and becomes a backward propagating wave. (b) The location of the  $F$  and  $B$  waves on the dispersion diagram.

Fig. 3(b) shows the location of these waves on a dispersion diagram.

Both forward and backward waves have to satisfy the dispersion relation,

$$\det[D(\beta_F, \omega)] = 0, \quad (10)$$

$$\det[D(\beta_B, \omega)] = 0. \quad (11)$$

Electromagnetic quantities must also be single valued at a given position and time at the resonance,

$$\rho e^{i(\beta_F - \beta_B)L} = 1. \quad (12)$$

Here,  $\rho$  is a round trip reflection coefficient. With the assumption of a loss less cavity that is completely shorted at both ends, we may write  $\rho = 1$  and  $\beta_B = -\beta_F$ . Hence, (12) becomes

$$\beta_F = \pi N/L \quad (13)$$

where  $N$  is an integer. Except for the propagation direction, the backward wave is identical to the forward wave; that is, it satisfies the same radial boundary condition and has the same energy. Therefore, in (3)–(5), the relationship between the coefficients  $A_n^B$  of backward wave and those  $A_n^F$  of the forward wave may be written as

$$A_n^F = A_n^B. \quad (14)$$

By summing the forward and backward waves, the electromagnetic field components in the cavity can be written

$$E_z(r, z, t) = e^{-i\omega t} \sum_{n=-\infty}^{\infty} 2A_n J_0\left(\frac{\chi_n}{R_0} r\right) \cos(\beta_n z) \quad (15)$$

$$E_r(r, z, t) = R_0 e^{-i\omega t} \sum_{n=-\infty}^{\infty} \frac{2A_n \beta_n}{\chi_n} J_1\left(\frac{\chi_n}{R_0} r\right) \sin(\beta_n z) \quad (16)$$

$$H_\phi(r, z, t) = -i\epsilon_0 \omega R_0 e^{-i\omega t} \sum_{n=-\infty}^{\infty} \frac{2A_n}{\chi_n} J_1\left(\frac{\chi_n}{R_0} r\right) \cos(\beta_n z). \quad (17)$$

In our calculations, the rank of the matrix was truncated at 9 ( $-4 < n < 4$ ) [15], [16]. Once the dispersion relation, (9), is solved numerically, the ratios of the coefficients,  $A_n/A_0$ , are determined from (8). With a known set of  $A_n/A_0$ , the field components  $E_z$ ,  $E_r$ , and  $H_\phi$  are calculated from (15)-(17).

### B. Perturbation Theory

Perturbation theory indicates that slight changes in the shape of a resonant cavity can affect the resonant frequency. Each resonance (associated with an axial mode) is frequency shifted by a perturbing object of volume  $\Delta V$  by a different amount. The general relation for the relative frequency shift is given by [2]

$$\frac{\Delta f_r}{f_r} = \frac{\int_{\Delta V} (\mu H \cdot H^* - \epsilon E \cdot E^*) dV}{\int_V (\mu H \cdot H^* + \epsilon E \cdot E^*) dV} \quad (18)$$

where the integral in the numerator is evaluated over the perturbing object volume  $\Delta V$  and the integral in the denominator is evaluated over the whole cavity. This assumes that the perturbing object is small compared to the amplitude and length of the wall ripple. For the case of a sphere [2] the above equation is geometrically corrected by multiplying the first term in the numerator by 3/2 and the second term in the numerator by 3. For a small metal bead of radius  $r_0$  the field is almost constant over  $\Delta V$  so the integration is unnecessary. Thus the equation commonly used is [1]

$$\frac{\Delta f_r}{f_r} = 2\pi r_0^3 \left( \frac{1}{2} H_0^2 - E_0^2 \right) \quad (19)$$

where  $E_0$  and  $H_0$  are the field amplitudes normalized so that the integral of  $H_0^2$  or  $E_0^2$  over the cavity is unity. Since the only field component on axis is  $E_z$ , the simplest measurement would be to find  $\beta_r$  by perturbing the field on axis. In our experiment, a bead was placed 0.54 cm away from the axis because of the difficulty associated with having both the bead and the antenna on axis. At this radius it was still possible to identify  $\beta_z$  for the  $TM_{01}$  modes by inspection of the axial profile of the frequency shift. Once the cavity fields are calculated, (19) can be used to find the associated perturbation. This frequency shift can then be directly compared with experimental measurements.

## IV. RESULTS OF THE FIELD MODEL AND EXPERIMENTAL VERIFICATION

There are two levels at which we can compare the field model of Section III with experiment. The first and simplest level is to compare the measured and calculated resonant frequencies associated with the axial modes. The second is to compare the field distribution (or the related spatial distribution of frequency shifts) of these modes using the

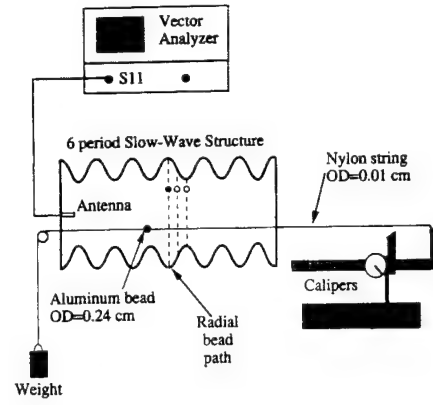


Fig. 4. Cold test system used for measuring the electromagnetic characteristics of spatially periodic structures. The perturbing bead could be translated both axially and radially.

spatial perturbation technique described in Section III. In this section we will present the comparison on both levels. Fig. 4 shows the measurement system, including the bead-pull apparatus to be described later.

### A. Resonant Frequencies

Experimentally, the modes of our slow-wave structure were excited using a small Hertzian antenna on the axis which could be moved axially in and out of the cavity to adjust the degree of coupling and to enable calibration. A network analyzer was used to measure the microwave reflection from the cavity over the desired frequency range ( $S_{11}$  single port measurement). The resonances appeared as narrow spikes at frequencies where the magnitude of the reflection was reduced.

The experimental results appear as plots of the resonant frequency ( $f_r$ ) versus the normalized axial wave number ( $\beta d$ ). All measurements were compared with numerical calculation. The measurements agree very well with the boundary specific calculation of Section III and the general boundary calculation using the 2-D electromagnetic code Superfish [19]. A graphical comparison of the experimental results with Superfish calculations is shown in Fig. 2(a). This figure shows the dispersion curve and reflection data with a common frequency axis. The Superfish results, which were actually calculated at seven points, are converted to form a smooth curve to aid in comparison with experiment. Similar plots comparing the measured and calculated results [16], [20] for the  $TM_{02}$  and  $TM_{03}$  modes are shown in Fig. 5(a) and 5(b), respectively. The measured frequencies of the  $TM_{01}$  resonances are, on average, 0.17% lower than our calculations and 0.03% higher than Superfish. For the  $TM_{02}$  and  $TM_{03}$  modes the experimental data are, respectively, 0.05% and 0.37% lower than our calculations.

### B. Field Distribution

To perturb the cavity a small object had to be placed at known locations within the structure and the resulting shift in the frequency of a given resonant mode was measured. Fig. 4 shows a schematic diagram of the apparatus and Table I gives a few critical dimensions.

TABLE I  
DIMENSIONS OF SLOW-WAVE STRUCTURE.

Structure Period	1.67 cm
Total Length	10 cm (6 periods)
Radius [cm]	$1.5 + .41 \sin(3.7z)$
Bead Diameter	0.24 cm
Radial Position of String	0.54 cm

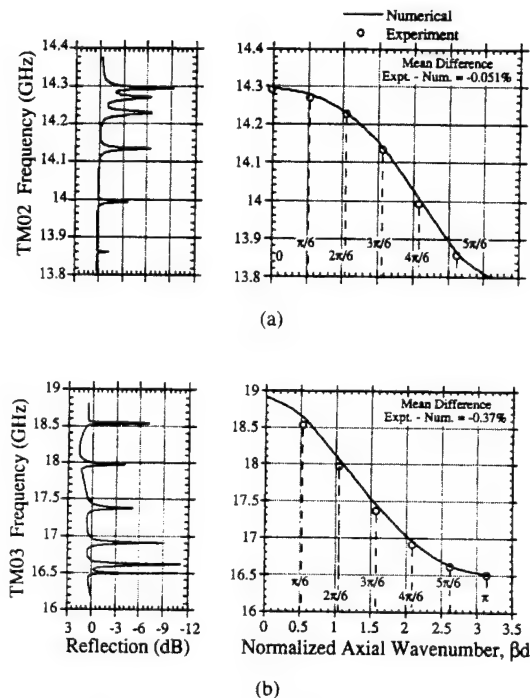


Fig. 5. (a) The dispersion diagram of an X-band slow wave structure having a passband of 7.4 to 8.7 GHz for the  $TM_{02}$  mode (smooth line). Also shown is the measured reflection data for the  $TM_{02}$  resonance peaks of the closed six period slow wave cavity (open circles). (b) Same as (a), but for the  $TM_{03}$  mode.

An aluminum bead was suspended in the cavity on a nylon thread via one of four sets of access holes; one set parallel to the cavity axis and three along the diameter at axial positions corresponding to the maximum, average, and minimum radii of the slow wave structure. Bead movement was regulated by tying one end of the thread to a dial caliper to measure position and the other end to a small weight to provide tension. An HP network analyzer measured the forward and reflected power versus frequency ( $S_{11}$ ) from a coax Hertzian element inserted on axis through the cavity end plate. For each mode, the resonant frequency was recorded as a function of bead position. The frequency shift at a given point is then the difference between this frequency and the frequency in an unperturbed cavity. It should be noted that the effect of the nylon thread was negligible (less than 500 kHz in all cases). Both axial and radial dependence of frequency shifts were measured. The first shift was measured with the bead translated along a path parallel to the cavity axis at a radial position of 0.54 cm. The second shift corresponded to a radial path at a position of maximum cavity diameter (see Fig. 4).

In general, measurements and calculations can be performed for each of the seven axial modes associated with each of the

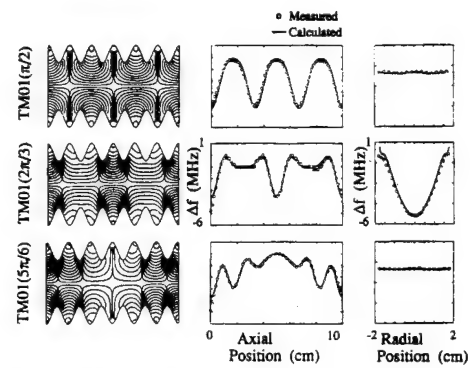


Fig. 6. Field perturbation results in the shorted structure for three axial modes of the  $TM_{01}$  transverse mode. (a) Plots of the electric field lines, axial and radial frequency perturbation for  $\pi/2$  axial mode; solid lines - calculation based on equation 18; open circles - experiment. (b) Same, for  $2\pi/3$ . (c) Same, for  $5\pi/6$ .

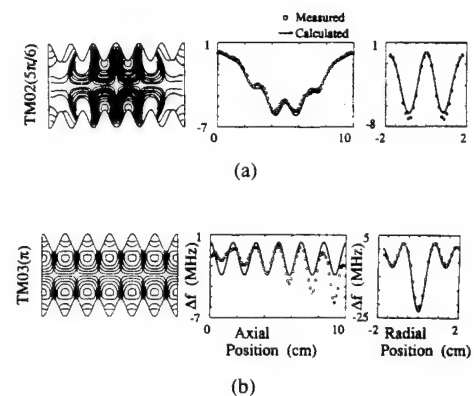


Fig. 7. Field perturbation results of the shorted structure for one axial mode of high order transverse modes. (a) Plots of the electric field lines, axial and radial frequency perturbation for  $5\pi/6$  axial mode of the  $TM_{02}$  mode; solid lines - calculation based on (18); open circles - experiment. (b) Same, for  $\pi$  mode of the  $TM_{03}$  transverse mode.

three transverse modes ( $TM_{01}$ ,  $TM_{02}$ ,  $TM_{03}$ ). In Fig. 6 and 7 we present selected results. All seven axial modes of the  $TM_{01}$  group of modes and some of the axial modes of the  $TM_{02}$ ,  $TM_{03}$ , and  $TM_{04}$  have been studied numerically and experimentally. The results are shown in Fig. 6(a), (b), (c) for the  $TM_{01}$   $\pi/2$ ,  $TM_{01}$   $2\pi/3$ , and  $TM_{01}$   $5\pi/6$  modes, respectively. The experimental results appear as circles overlaid on solid lines that represent the numerical results. To help visualize the cavity fields, a plot of the electric field lines for each axial mode is displayed beside the corresponding data. Similarly, Fig. 7(a) displays the  $5\pi/6$  mode of the  $TM_{02}$  series and Fig. 7(b) shows the  $\pi$  mode of the  $TM_{03}$  series. The normalized wave number,  $\beta d$ , can be found from these results by simply counting the number of local maxima along the length of the resonator and multiplying the number by  $\pi/6$ .

## V. REFLECTION AND Q-FACTOR OF AN OPEN SLOW-WAVE STRUCTURE

In most low power linear microwave devices the output power is extracted radially at one end of the interaction region. Microwave mode converters change the cylindrical mode produced in the interaction region into the fundamental

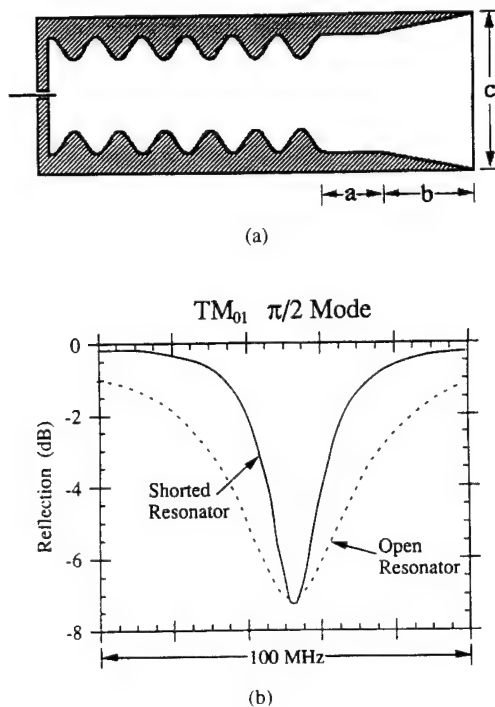


Fig. 8. (a). A schematic diagram of an open slow wave cavity – a way for axial power extraction in a relativistic backward wave oscillator. In this work  $a = 1.02$  cm,  $b = 7.62$  cm,  $c = 4.75$  cm. (b). Demonstration of resonance broadening. The  $\pi/2$  resonance of the  $TM_{01}$  mode is broadened when the structure is open (dotted line) as compared to the shorted case (solid). This effect is used to calculate the reflection at the end of the structure.

mode of a waveguide which can transport the energy to the load or antenna. At power levels of tens of MW, the complex geometry of the mode converter can lead to breakdown even in vacuum. To avoid this problem high power tube designs eliminate the mode converter and allow the output power to exit the slow-wave structure along the beam axis. Then the beam is separated from the microwave by tapering the magnetic guide field and thus dumping the beam into the wall of the waveguide. For these discussions this type of cavity is labelled “open” [23]. A diagram of a practical open cavity used in high power BWO experiments [8], [11] is shown in Fig. 8(a).

When modeling a BWO it is important to know the end reflection of the structure. End reflections affect both the starting conditions and saturation effects in the device [5], [6]. Several numerical codes can predict the end reflection coefficient ( $\rho$ ) for a given geometry, however, it is often difficult to accurately calculate end reflections due to the complex geometry of such systems and the often unknown surface finish conditions used. For these reasons it is important to perform experimental measurements. The most direct method of measuring  $\rho$  is to launch the desired mode down the structure and measure the waves which are transmitted through or reflected from the end of the structure. This technique requires both launching the desired mode and completely absorbing the reflected wave inside the structure. Either of these would be very difficult in practice. It is much easier to find  $\rho$  indirectly by exploiting its relation to the diffractive quality factor of the structure. The diffractive quality factor of a structure ( $Q_d$ ) is related to the

radiative power loss through the output aperture of the cavity, whereas the power loss to the walls is related to the ohmic quality factor of the cavity ( $Q_{ohm}$ ).

To find  $Q_d$  it is necessary to separate the ohmic losses ( $Q_{ohm}$ ) from the total circuit losses ( $Q_t$ ) which include the radiative losses of the cavity. Since the Q-factor is inversely related to power loss,  $Q_d$  can be found from  $Q_t$  and  $Q_{ohm}$  by the relation

$$Q_d = 1/(1/Q_t - 1/Q_{ohm}). \quad (20)$$

Both  $Q_t$  and  $Q_{ohm}$  can be measured directly. The measured quality factor of the system is  $Q_t$  when the structure is open, and  $Q_{ohm}$  when the diffractive loss is eliminated by placing a short at the output side of the structure. Fig. 8(b) demonstrates this effect by showing how the  $\pi/2$  resonance of the  $TM_{01}$  mode is broadened when the end of the structure is opened.

#### A. Experimental measurement of Q

It is useful to give some details of our Q measurement here. We measured the voltage standing wave ratio (VSWR) of the cavity across the desired resonance or resonances using a HP8510C vector network analyzer (we used a one-port measurement for simplicity). From this data we found the minimum VSWR (at resonance) and the maximum VSWR (between resonances). From these two values we used a technique [21] to find the VSWR level at which to read the upper and lower frequencies,  $f_1$  and  $f_2$ , of each resonance. From these frequencies, and the resonant frequency  $f_r$  we can calculate the cavity Q using the relation

$$Q = f_r/(f_1 - f_2). \quad (21)$$

With the additional knowledge of whether the cavity was under-coupled (less than optimum coupling) or over-coupled (more than optimum coupling) a correction factor for the Q was found that eliminated the loading effect of our measurement apparatus and wave launcher. The cavity coupling could be adjusted by moving the launcher in and out of the cavity. Using the minimum insertion which would give a clear resonance we were certain to be in the under-coupled regime. The cavity was made of brass.

Using these techniques we measured the Q's of the cavity modes in both open-ended and close-ended configurations. As a check we compared the measured Q's for the shorted configuration with an analytic calculation which is described in detail in Appendix II. These results appear in Fig. 9. The agreement of the measured and calculated Q's is very good when we use a surface roughness factor of 1.7. This factor effectively increases the skin depth in the calculation to compensate for increased field penetration due to surface imperfections (i.e. fabrication, oxidation).

We use (20) to calculate  $Q_d$  from the measured values of  $Q_t$  and  $Q_{ohm}$ . The only remaining step is to calculate the end reflection,  $\rho$ , from  $Q_d$ . Appendix I presents a derivation of the

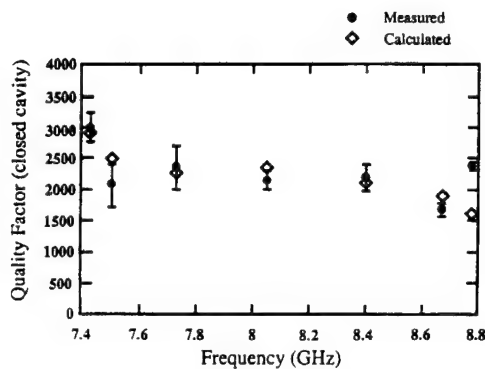


Fig. 9. Calculation (open squares) and measurement (bars) of the wall losses for various axial modes associated with the  $TM_{01}$  mode of the shorted periodic cavity. The surface finish factor is 1.7.

relation of these two parameters. The result is

$$\rho = \sqrt{\frac{1 - (\alpha/Q_d)}{1 + (\alpha/Q_d)}} \quad (22)$$

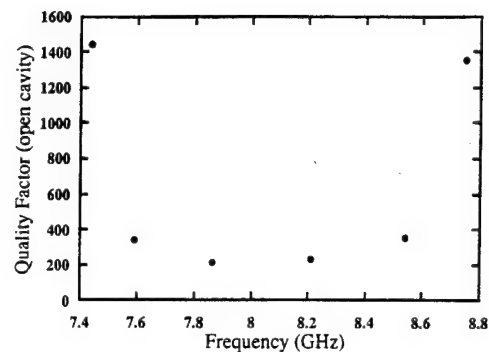
where  $\alpha = (\omega/c)^2(L/\beta)$ . Using this relation the measured values of  $\rho$  were found. These values of  $\rho$  for the  $TM_{01}$  axial modes were compared with a set of calculations performed by A. Bromborsky [22]. The results appear in Fig. 10(b). The measured reflection coefficients are up to 15% larger than the calculated ones. This is a significant difference since reflections are important for both the linear characteristics (starting conditions) and for simulations of non-stationary operation of pulsed relativistic backward wave tubes. For example, a 15% change in the reflection coefficient can cause the starting current to double.

## VI. SUMMARY AND CONCLUSIONS

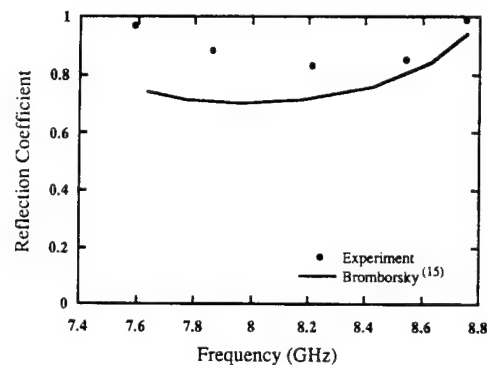
The electromagnetic properties of slow-wave resonators for high-power relativistic backward wave tubes have been studied both theoretically and experimentally. The agreement between the measured and calculated frequencies and spatial field distributions is very good (the discrepancy is less than 0.2%) for the first three symmetric transverse magnetic modes ( $TM_{0p\ell}$ ) with the index  $p$  from 1 to 3 and various axial indices  $\ell$  (from 0 to  $N$  where  $N$  is the number of periods of a slow-wave resonator). Preliminary data is also available for the  $TM_{04}$  mode, which is characterized by a very flat dispersion curve (see Fig. 1).

We have also developed a simple method to measure the end reflections in open slow-wave resonators by measuring their Q-factors. This measurement technique gives results for end reflections which are up to 15% higher than those that follow from computer code simulations [22].

Applying these techniques is especially important to high-power relativistic BWO's with overmoded structures because their dispersion diagram may not be a monotonic function of the axial wave number. For this reason it is necessary to measure both the frequency and the axial wave number, as was done in this work, in order to identify the transverse and axial indices of the operating mode.



(a)



(b)

Fig. 10. (a) Measurement of the diffractive quality factor of the open periodic cavity for various axial modes associated with the  $TM_{01}$  mode. (b) The measured reflection coefficient for various axial modes, derived from the diffraction quality factor using (22).

The results obtained are important in the design of future high-power relativistic backward wave oscillators, relativistic travelling wave tubes, overmoded multiwave Cherenkov and multiwave diffraction generators. We also plan to extend the technique described here to the study of plasma filled relativistic slow wave devices [24].

## ACKNOWLEDGMENT

The authors gratefully acknowledge discussions with T.M. Antonsen, Jr., B. Levush, A. Vlasov, and H. Guo on the behavior of finite length periodic systems. We also thank D. Cohen and J. Pyle for their assistance with the experiment and ARL personnel for their help and the use of their facilities.

## APPENDIX I DEPENDENCE OF CAVITY END-REFLECTION ON DIFFRACTIVE QUALITY FACTOR

We consider a cavity consisting of a section of waveguide with a short at one end and a "leaky" aperture (antenna) at the other. We find the dependence of the reflection from this aperture,  $\rho$ , on the diffractive quality factor of the cavity  $Q_d$  in two steps. First, we relate  $Q_d$  to the ratio of circulating power to power loss, and then we relate this ratio to the end-reflection. We begin with a description of  $Q_d$  and how it relates

to the total and ohmic quality factors. These three Q-factors are defined as follows:

$Q_{\text{ohm}}$  = Q-factor related to RF power lost in the cavity wall by resistive heating

$Q_t$  = Q-factor related to all power loss mechanisms (ohmic and radiation)

$Q_d$  = Q-factor related to power lost by diffraction through an aperture in the cavity.

By definition, the Q-factor is related to the cavity power loss,  $P_{\text{loss}}$ , by the equation

$$Q = \omega(U/P_{\text{loss}})$$

where  $\omega$  is the resonant frequency and  $U$  is the electromagnetic energy stored in the cavity. Because  $Q$  is inversely related to power loss, and the total power loss is equal to the sum of the diffractive and ohmic losses, the three Q-factors have the relation

$$1/Q_t = 1/Q_{\text{ohm}} + 1/Q_d. \quad (23)$$

An experimental measurement of the open cavity would give the value for  $Q_t$ . If the aperture was shorted then the measurement would give  $Q_{\text{ohm}}$ . Thus, using this equation, all three  $Q$ s can be experimentally determined.

We now proceed to relate  $Q_d$  to the end reflection. To accomplish the first step we use the relation between power and energy in an empty waveguide

$$P/u = (\beta/\omega)c^2 = v_{gr} \quad (24)$$

where  $u$  is the energy per unit length in the waveguide ( $U/L$ ) and  $v_{gr}$  is the group velocity. Using this relation the definition of quality factor becomes

$$Q_d = (\omega/c)^2(L/\beta)(P_{\text{circ}}/P_d) \quad (25)$$

where  $P_{\text{circ}}$  now represents the power circulating in the cavity. To relate  $P_{\text{circ}}/P_d$  to the end-reflection  $\rho$ , we consider the forward and reverse waves in the cavity with associated power  $P_+$  and  $P_-$ , and the power lost through the cavity aperture  $P_d$ . By definition

$$P_-/P_+ = |\rho|^2 \quad (26)$$

and

$$P_+ - P_- = P_d \quad (27)$$

so

$$P_d/P_+ = 1 - |\rho|^2. \quad (28)$$

By eliminating  $P_+$  and  $P_-$  we relate the power ratio to the reflection coefficient

$$\frac{P_{\text{circ}}}{P_d} = \frac{P_+ + P_-}{P_d} = \frac{1 + |\rho|^2}{1 - |\rho|^2}. \quad (29)$$

Thus, substituting into the equation for  $Q_d$

$$Q_d = \alpha \frac{1 + |\rho|^2}{1 - |\rho|^2} \quad (30)$$

where

$$\alpha = (\omega/c)^2(L/\beta). \quad (31)$$

Inverting this expression in terms of  $\rho$ , we find

$$\rho = \sqrt{\frac{1 - (\alpha/Q_d)}{1 + (\alpha/Q_d)}}. \quad (32)$$

This is the relation we used to find the cavity end-reflection in Section V of this paper (22).

## APPENDIX II

### OHMIC LOSSES IN RESONATORS WITH CORRUGATED WALLS

Consider a resonator formed by the part of a cylindrical waveguide with corrugated walls which is bounded with two end walls. In general, the ohmic quality factor ( $Q$ ) of any resonator can be defined as

$$Q_{\text{ohm}} = \frac{\overline{W}}{\overline{W}_{\text{ohm}}} = 2 \frac{\int_V |\vec{H}_{\sim}|^2 dV}{\int_{V_{\text{skin}}} |\vec{H}_{\sim}|^2 dV}. \quad (33)$$

Here, the bars imply the averaging over the wave time period  $2\pi/\omega$ ,  $W$  is the microwave energy stored in the resonator,  $W_{\text{ohm}}$  is the microwave energy concentrated in a skin-layer of the metallic walls.  $V_{\text{skin}}$  is the volume associated with the skin depth. The coefficient 2 reflects the fact that inside a resonator the electric field amplitude is equal to the magnetic field amplitude while in a metallic wall (with the finite but very large conductivity,  $\sigma$ ) only the magnetic field is significant since  $E_{\sim} \sim (1/\sqrt{\sigma})H_{\sim}$ .

We will restrict our consideration to the simplest but most important case of symmetric  $\text{TM}_{0p\ell}$  modes. The magnetic field of such modes has only one, non-zero component directed along azimuthal coordinate  $\phi$  ( $H_{\sim\phi}$ ). In a corrugated structure with strong end reflections this field, excited at the given frequency  $\omega$ , can be presented as

$$H_{\sim\phi} = H_{\phi} e^{i\omega t} + \text{complex conjugate.}$$

where

$$H_{\phi} = i\epsilon_0\omega R_0 \sum_{n=-\infty}^{\infty} \frac{A_n}{\chi_n} J_1(g_n r) e^{i\beta_n z} \quad (34)$$

$$\beta_n = l\pi/L + n\bar{\beta}$$

Here  $l\pi/L$  is the axial wave number of the field, the wave number  $\bar{\beta}$  is determined by the period of corrugation  $d$ :  $\bar{\beta} = 2\pi/d$ , the transverse wave number  $g_n$  is equal to  $g_n = [(\omega/c)^2 - \beta_n^2]^{1/2}$ . This is the form given by (5). For slow spatial harmonics  $g_n^2 < 0$  ( $n \neq 0$ ), and therefore,  $J_1(g_n r) = iI_1(p_n r)$



where  $p_n^2 = -g_n^2$ . Below we will take into account only zero and  $\pm$  first spatial harmonics supposing that amplitudes of all other harmonics are negligibly small.

Let us consider periodical corrugation of the resonator wall,

$$R = R_0 + h \cdot \cos \bar{\beta} z \quad (35)$$

and suppose that the height of these ripples,  $h$ , is much smaller than the wavelength,  $\lambda$ . In such a case of small ripples it is possible to replace the boundary condition for the field at the real corrugated wall by an approximate boundary condition at the wall of the cylindrical waveguide of radius  $R_0$  [25]. From this condition one can find the relation between spatial harmonic amplitudes [26]:

$$\frac{A_{\pm 1}}{A_0} = -i \frac{h}{2} \cdot \frac{g_0^2 \mp (l\pi/L) \cdot \bar{\beta}}{p_{\pm 1}} \cdot \frac{J_1(g_0 R_0)}{I_0(p_{\pm 1} R_0)}. \quad (36)$$

In the case of arbitrary relations between  $h$  and  $\lambda$  the ratio of harmonic amplitudes can be found only numerically.

In addition to the assumptions given above let us also assume that the structure consists of an integer number of periods:  $L = N \cdot d$  where  $N$  is an integer. Then, for the microwave energy stored in the resonator one can obtain the following formula:

$$\bar{W} = \pi L R_0^2 \left[ \left( \epsilon_0 \omega R_0 \frac{A_0}{\chi_0} \right) J_1(\chi_p) \right]^2 (1 + \alpha_1^2 \phi_1 + \alpha_{-1}^2 \phi_{-1}) \quad (37)$$

where  $\chi_p = g_0 R_0$  is the  $p$ th root of the equation  $J_0(\chi) = 0$ , which is the boundary condition for the  $TM_{0p\ell}$  mode in a waveguide of the constant radius  $R_0$ ,

$$\begin{aligned} \alpha_{\pm 1} &= \left( \frac{h}{2} \cdot \frac{g_0^2 \mp l\pi/L \cdot \bar{\beta}}{p_{\pm 1}} \right), \pm \\ \phi_{\pm 1} &= \frac{1}{I_0^2(p_{\pm 1} R_0)} [I_1^2(p_{\pm 1} R_0) - I_0(p_{\pm 1} R_0) I_2(p_{\pm 1} R_0)]. \end{aligned} \quad (38)$$

The last two terms in (II.5) correspond to the  $\pm$  first spatial harmonics.

In a similar manner one can find the microwave energy stored in a skin-layer of the depth  $\delta_{sk}$ . Note that due to a certain roughness of the wall, a realistic skin depth is 1.5 – 2 times larger [27] than the theoretical value. Correspondingly, the ohmic Q-factor of the closed cavity

$$Q_{ohm}^{closed} = \frac{\bar{W}}{\bar{W}_{ohm,corr} + \bar{W}_{ohm,e.w.}} \quad (39)$$

where  $\bar{W}_{ohm,corr}$  is the average microwave energy concentrated in a skin-layer of the corrugated wall of a waveguide section, and  $\bar{W}_{ohm,e.w.}$  is the microwave energy concentrated in a skin-layer of end walls. Denoting the skin-depth by  $\delta_{sk}$  one can derive for  $\bar{W}_{ohm,corr}$ ,  $\bar{W}_{ohm,e.w.}$  the following

expressions:

$$\begin{aligned} \bar{W}_{ohm,corr} &= \pi \delta_{sk} L \left( \epsilon_0 \omega R_0 \frac{A_0}{\chi_0} \right)^2 R_0 J_1^2(\chi_p) \\ &\left\{ 1 + \alpha_1^2 q_1^2 + \alpha_{-1}^2 q_{-1}^2 + \frac{h}{R_0} (\alpha_1 q_1 + \alpha_{-1} q_{-1}) + \left( \frac{h\bar{\beta}}{2} \right)^2 \right\}, \end{aligned} \quad (40)$$

$$\begin{aligned} \bar{W}_{ohm,e.w.} &= 2\pi \delta_{sk} \left( \epsilon_0 \omega R_0 \frac{A_0}{\chi_0} \right)^2 R_0^2 J_1^2(\chi_p) \\ &\left\{ 1 + \alpha_1^2 \phi_1 + \alpha_{-1}^2 \phi_{-1} + 4\alpha_1 \frac{p_1}{\beta + 2(l\pi/L)} \cdot \frac{1}{\beta R_0} \right. \\ &\left. + 4\alpha_{-1} \frac{p_{-1}}{\beta - 2(l\pi/L)} \frac{1}{\beta R_0} + \frac{\alpha_1 \alpha_{-1}}{\beta R_0 \cdot (l\pi/L)} (p_1 q_{-1} - p_{-1} q_1) \right\}, \end{aligned} \quad (41)$$

Here  $q_{\pm 1}$  denotes  $I_1(p_{\pm 1} R_0)/I_0(p_{\pm 1} R_0)$ .

Substituting equations (II.5), (II.6), (II.8) and (II.9) into (II.7) one can find the ohmic Q-factor of the closed cavity. In microwave generation experiments [3,4,6,7] structures without end walls are used. Correspondingly, when reflections of the microwave power at both ends ( $z = 0$  and  $z = L$ ) are large enough, the ohmic Q-factor of the resonator can be estimated by the following equation

$$Q_{ohm}^{open} = \frac{\bar{W}}{\bar{W}_{ohm,corr}}, \quad (42)$$

where  $\bar{W}$  and  $\bar{W}_{ohm,corr}$  are defined by Eqs. (II.5) and (II.8), respectively. Equation (II.7) was used in Section V (and Fig. 9) to calculate the ohmic losses in a shorted cavity.

Two limiting cases should be considered separately. In case of the 0-mode, we have  $l = 0$ ,  $\beta_1^2 = \beta_{-1}^2$ ,  $p_1 = p_{-1}$ ,  $q_1 = q_{-1}$ ,  $\alpha_1 = \alpha_{-1}$  and  $\phi_1 = \phi_{-1}$ , which means that the first and minus first harmonics degenerate to each other except for difference in propagating direction. Thus we have to recalculate our formulas from the first step by taking the degeneracy into consideration. This leads to simplified expressions for terms defined by eqs.(II.8),(II.9). We do not present here these formulas because it was found that for parameters of our slow-wave structure the amplitudes of  $\pm$  first harmonics are small ( $A_1 = A_{-1} = 0.02A_0$ ), and therefore these harmonics can be ignored in calculation. This fact has been used to calculate the Q-value of the 0-mode in Fig. 6.

In case of  $\pi$ -mode, a zero harmonic of forward wave and minus first harmonic of backward wave have the same axial wave number as well as a zero harmonic of backward wave and plus first harmonic of forward wave. They propagate in opposite directions and thus form a standing wave together. In other words, these harmonics degenerate to each other in terms of dependence of the radial coordinate and therefore all formulas must account for this effect. We do not present here these formulas recalculated, because it was found that in our experiment the intersection between the light-line,  $\omega = k_z c$  and the dispersion curve is close to the point of the  $\pi$ -mode, which means  $|g_0| \ll \bar{\beta}$ , where

$$p_0^2 \equiv -g_0^2 = -\left(\frac{\omega}{c}\right)^2 + \frac{\bar{\beta}^2}{4} > 0.$$

This condition  $|g_0| \ll \bar{\beta}$  simplifies the consideration. For experimental parameters the following relation between har-

monic amplitudes was found,

$$\frac{A_1}{A_0} = -1.57 \times 10^{-4}, \quad \frac{A_{-1}}{A_0} = 1.025.$$

Thus we were able to ignore the plus first harmonic and to approximate the magnetic field as

$$H_\phi = \left( \epsilon_0 \omega R_0 \frac{A_0}{\chi_0} \right) I_1(p_0 R_0) \cos(\beta z/2) \quad (43)$$

This expression has been used to calculate the Q-value of the  $\pi$ -mode in Fig. 6.

## REFERENCES

- [1] L. C. Maier and J. C. Slater "Field strength measurements in resonant cavities," *J. Appl. Phys.*, vol. 23, pp. 68-77, 1952.
- [2] Om. P. Gandhi, *Microwave Engineering and Applications*, Pergamon Press, 1984.
- [3] D. K. Abe, T. Antonsen, Jr., Y. Carmel, W. W. Destler, V. L. Granatstein, B. Levush, and S. M. Miller, "Experimental studies of overmoded high power microwave generators," in *1993 IEEE Inter. Conf. on Plasma Science*.
- [4] D. K. Abe, T. Antonsen, Jr., A. Bromborsky, Y. Carmel, B. Levush, and S. M. Miller, "Experimental and theoretical results from the University of Maryland multiwave Čerenkov generator program," in *Beams '92 Conf. Proc.*
- [5] B. Levush, T. M. Antonsen, Jr., A. Bromborsky, W. R. Lou, Y. Carmel, "Theory of relativistic backward wave oscillators with end reflections," *IEEE Trans. Plasma Sci.*, vol. 30, pp. 263-280, 1992.
- [6] B. Levush, T. M. Antonsen, Jr., A. Bromborsky, W. R. Lou, Y. Carmel, "Relativistic backward wave oscillators: Theory and experiment," *Phys. Fluids B*, vol. 4, pp. 1-7, 1992.
- [7] N. F. Kovalev, M. I. Petelin, M. D. Raiser, A. V. Smorgonsky and L. E. Tsopp, "Generation of powerful electromagnetic radiation pulses by a beam of relativistic electrons," *JETP Lett.*, vol. 18, pp. 138-140, 1973.
- [8] Y. Carmel, W. R. Lou, J. Rodgers, H. Guo, W. W. Destler, V. L. Granatstein, B. Levush, T. Antonsen, Jr., and A. Bromborsky, "From linearity towards chaos: Basic studies of relativistic backward wave oscillators," *Phys. Rev. Lett.*, vol. 69, pp. 1652-1655, 1992.
- [9] S. P. Bugaev et al., "Relativistic multiwave Čerenkov generators," *IEEE Trans. Plasma Sci.*, vol. 18, pp. 525-536, 1990.
- [10] S. D. Korovin et al., "The nonuniform-phase velocity relativistic BWO," in *9th International Conference on High Power Particle Beams, BEAMS 92*, Washington, DC, May 25-29, 1992, Paper PG-02.
- [11] R. A. Kehs et al., "High power backward wave oscillator driven by a relativistic electron beam," *IEEE Trans. Plasma Sci.*, vol. PS-13, pp. 559-562, 1985.
- [12] C. C. Johnson, *Field and Wave Electrodynamics*, New York: McGraw-Hill, 1965, ch. 7.
- [13] Y. Carmel, H. Guo, W. R. Lou, D. Abe, V. L. Granatstein, and W. W. Destler, "Novel method for determining the electromagnetic dispersion relation of periodic slow wave structures," *Appl. Phys. Lett.*, vol. 57, pp. 1304-1306, 1990; also, H. Guo, Y. Carmel, W. R. Lou, L. Chen, J. Rodgers, D. Abe, A. Bromborsky, W. Destler, and V. L. Granatstein, "A novel highly accurate technique for determination of the dispersive characteristics in periodic slow wave circuits," *IEEE Trans. Microwave Theory and Tech.*, vol. 40, pp. 2086-2094, 1992.
- [14] J. A. Swegle et al., "Backward wave oscillators with rippled wall resonators: Analytic theory and numerical simulation," *Phys. Fluids*, vol. 28, pp. 2882-2894, 1985. This paper also contains a list of Soviet references on this topic.
- [15] K. Minami, Y. Carmel, V. L. Granatstein, W. Destler, W. R. Lou, D. Abe, T. Hosokawa, K. Ogura, and T. Watanabe, "Linear theory of electromagnetic wave generation in plasma loaded corrugated wall resonators," *IEEE Trans. on Plasma Sci.*, vol. 18, pp. 537-545, 1990.
- [16] K. Ogura, K. Minami et al., *J. Phys. Soc. Japan*, vol. 61, p. 3966, 1992.
- [17] V. I. Kurilko et al., *Sov. Physics Tech. Physics*, vol. 24, p. 1451, 1979.
- [18] M. M. Ali, K. Ogura et al., *Phys. Fluids B*, vol. 4, p. 1023, 1992.
- [19] K. Halbach, and R. Holsinger, *Part. Accel.*, vol. 1, p. 213, 1976.
- [20] The results are also in excellent agreement with those of A. Bromborsky and B. Ruth, *IEEE Trans. Microwave Theory Tech.*, vol. MTT-32, p. 600, 1984.
- [21] D. K. King, *Measurement at Centimeter Wavelength*, pp. 128-141, New York: Van Nostrand Co., 1952. See also, L. Malter and G. A. Brewer, *J. Appl. Phys.*, vol. 20, p. 10, 1949.
- [22] A. Bromborsky, private communication.
- [23] The subject of "open" cavities with smooth walls is discussed in L. A. Weinstein, *Open Resonators and Open Waveguides*, Boulder, CO: Golem Press, 1969. In this work we deal with cavities having spatially periodic walls.
- [24] Y. Carmel, W. R. Lou, T. M. Antonsen, Jr., J. Rodgers, B. Levush, W. W. Destler, and V. L. Granatstein, "Relativistic plasma microwave electronics: Studies of high-power plasma filled backward wave oscillators," *Phys. Fluids B*, vol. 4, pp. 2286-2292, 1992.
- [25] N. F. Kovalev, "Electrodynamical structure of the ultrarelativistic BWO," *Elektronnaya Tekhnika*, ser. 1, Elektronika SVCh, no. 3, pp. 102-106, 1978.
- [26] B. Z. Katzenelenbaum, *Theory of Irregular Waveguides with Slowly Variable Parameters*, Moscow, 1961.
- [27] K. Kreisher and R. J. Temkin, in *Infrared and Millimeter Waves*, vol. 7, ch. 8, Academic Press, 1983, p. 377.

William Main, photograph and biography not available at the time of publication.



**Yuval Carmel** (S'66-M'74) was born in Israel in 1942. He received the B.Sc. (EE) and M. Sc. (EE) degrees from the Technion, Israel Institute of Technology, in 1966 and 1971, respectively, and the Ph.D. (EE) degree from Cornell University, Ithaca, NY, in 1974.

He was with the government of Israel, the Naval Research Laboratory, and is currently with the University of Maryland, College Park. His research interest include electromagnetic radiation from intense electrons beams, plasma microwave devices,

advanced concepts in millimeter-wave tubes, gyrotrons, and backward wave oscillators.



**K. Ogura** was born in Japan in 1957. He received the B.Sc. degree in physics from Okayama University in 1981, and the M.Sc. and D.Sc. degrees in physics from Kyoto University in 1983 and 1989, respectively.

He is an Associate Professor in the Electrical and Electronic Engineering Department of Niigata University. His research interests include high-power microwave oscillators and their applications to plasma heating.



**James Weaver** received the B.S. degree in physics from the Massachusetts Institute of Technology in 1992. He is currently a graduate student in the Department of Electrical Engineering at the University of Maryland at College Park.



**Gregory Nusinovich** for a photograph and biography see page 524 of this issue.



**S. Kobayashi** received the B.Sc. and M.Sc. degrees in geological science from Kyoto University, in 1986 and 1989, respectively, and the M.Sc. degree in physics from Washington State University in 1991. He is currently a graduate student in the Department of Physics at the University of Maryland, College Park.



**Jeffrey P. Tate** was born on April 15, 1958 in Detroit, Michigan. He received the B.S. degree in electrical engineering in 1982 from Michigan State University, East Lansing. From 1982-1983 he worked as a systems engineer for the Detroit Edison Company. He received the M.S. degree in electrical engineering from Michigan State in 1985. In 1991 he received the Ph.D. degree in electrical engineering and applied physics from Cornell University.

During his study for the M.S. degree, he completed thesis work on magnetostatic surface-wave amplifiers. In 1986 and 1987 he held summer internships with the Advanced Microwave and Millimeter-wave Laboratory of TRW, performing research in the area of gallium-arsenide microwave integrated circuits. His doctoral research involved the characterization of high electron-cyclotron harmonic radiation from a Penning discharge plasma. He currently holds a research associate position at the University of Maryland, College Park, where his work includes the study of advanced harmonic gyrotron devices. His other interests include passive microwave components, plasma diagnostics and microwave materials processing.

**John Rodgers**, photograph and biography not available at the time of publication.

**A. Bromborsky**, photograph and biography not available at the time of publication.



**S. Watanabe** was born in Japan in 1969. He received the B.S. (EE) and M.S. (EE) degrees from Niigata University in 1991 and 1993, respectively.

He is presently a Ph.D. candidate at the Graduate School of Science and Technology, Niigata University. His research interests include high-power microwave generators and cryogenic plasmas.



**M. R. Amin** was born in Rangpur, Bangladesh in 1959. He received the B.Sc. (EEE) degree from the University of Rajshahi in 1984 and the M.Sc. (EEE) degree from Bangladesh University of Engineering and Technology, Dhaka, in 1987. He is now on sabbatical from the Bangladesh Institute of Technology, Rajshahi, where he is an Assistant Professor in the Electrical and Electronic Engineering Department. He is presently working toward the Ph.D. degree at the Graduate School of Science and Technology, Niigata University, Japan.

His research interests include theoretical and experimental investigations of high-power microwave devices, and semiconductor power electronic drives.

Mr. Amin is a member of the Institute of Engineers Bangladesh (IEB), and the Physical Society of Japan.



**K. Minami** was born in Japan in 1938. He received the B.S. (EE) degree at Nagoya Institute of Technology in 1962, the M.S. (EE) degree at the Tokyo Institute of Technology in 1964, and the Ph.D. degree at Nagoya University in 1969.

Since 1986 he has been a Professor in the Electrical Engineering Department, Niigata University, Japan. His research interests include the generation of high-power microwave radiation and interaction between powerful microwaves and plasmas.

**William W. Destler** (M'84), photograph and biography not available at the time of publication.

**Victor L. Granatstein** for a photograph and biography see page 525 of this issue.

# Theory of relativistic backward wave oscillators operating near cutoff

S. M. Miller, T. M. Antonsen, Jr., B. Levush, A. Bromborsky, D. K. Abe, and Y. Carmel  
*Laboratory for Plasma Research, University of Maryland, College Park, Maryland 20742*

(Received 14 June 1993; accepted 30 November 1993)

A numerical model for analyzing backward-wave oscillators (BWOs) operating near the upper edge of the transmission band is presented. The model is used to calculate starting currents for two finite length devices, an X-band BWO ( $f=8.4$  GHz) and a J-band BWO ( $f=5.5$  GHz). The operating frequency and efficiency predicted by the nonlinear numerical simulations are compared with experimental data for each device.

## I. INTRODUCTION

Backward-wave oscillators (BWOs) utilize a high-current electron beam to produce high-power, coherent radiation in the centimeter and millimeter wavelength regime. Under certain voltage and beam current operating conditions, a backward-wave oscillator can operate near the upper edge of the transmission band, where the group velocity of the electromagnetic wave goes to zero. Most frequently, this corresponds to operation at the so-called " $\pi$ " point, where the electromagnetic fields have a period twice that of the structure. There are a number of practical reasons for operation near this point. First, the start current usually has its lowest value in this case. Thus, if the length of the interaction region and the available beam current are constrained, one can still design a device that will operate efficiently by placing the operating point at the minimum of the group velocity. Second, once a particular structure is chosen, its operating point can be varied by varying beam voltage. The highest-frequency operation will occur at the " $\pi$ " point. Thus, it is natural to consider operation in this regime.

For frequencies near the " $\pi$ " point the cold structure dispersion relation can be approximated as a quadratic function of the wave number. A theoretical model, similar to those presented in Refs. 1–3, is developed in this paper to describe the operation of the device in this regime. The model consists of the self-consistent set of equations that describe the slow evolution of the envelope of the radiation field and the relativistic motion of the electrons along a strong magnetic field. Numerical calculations of the starting current are performed and compared with an analytic expression for the starting current derived by assuming a fixed field profile.

To compare with experimental results, the effects of a time-varying voltage and beam current pulse are included in the theoretical modeling. We consider two BWOs, an X-band BWO ( $f=8.4$  GHz) and a J-band BWO ( $f=5.5$  GHz). We compare predictions of peak efficiencies and operating frequencies from the theoretical model with experimental results.<sup>4,5</sup> From studies performed on the X-band BWO, agreement is shown between experiment and theory. However, as will be seen, some aspects of the J-band BWO experiment are not explained by the model.

Earlier theoretical modeling of the X-band device<sup>6</sup> was developed, with the assumption that the interaction takes

place at frequencies far away from the zero group velocity point. However, at high voltages this assumption breaks down. The present model allows us to accurately model the behavior of the device at operating points near the upper edge of the transmission band.

## II. THEORETICAL MODEL

In this section we develop the theoretical model to describe the BWO interaction near the upper edge of the transmission band, where the group velocity vanishes. In our model, we assume the interaction between the electron beam and the electromagnetic waves of the cold slow-wave structure is weak in the following sense. Over a length equal to a period of the structure, the electromagnetic fields have the same temporal and spatial dependence as the cold-structure fields. The effect of the beam is to cause the envelope of the electromagnetic fields to vary slowly in axial distance and time. In addition, the beam produces a small space-charge field that is proportional to the beam density.

Our derivation will begin by reviewing the approach of Refs. 4 and 6. The electromagnetic fields in the structure can be written as follows:

$$\mathbf{E}(\mathbf{x}, t) = [\mathbf{E}_p(\mathbf{x}, k)\epsilon(z, t) + \mathbf{E}_p^{(s)}(\mathbf{x}, k)]e^{i(kz - \omega t)} + \text{c.c.}, \quad (1)$$

$$\mathbf{B}(\mathbf{x}, t) = [\mathbf{B}_p(\mathbf{x}, k)\epsilon(z, t) + \mathbf{B}_p^{(s)}(\mathbf{x}, k)]e^{i(kz - \omega t)} + \text{c.c.}, \quad (2)$$

where  $\epsilon(z, t)$  is the slowly varying amplitude of the electromagnetic waves,  $\mathbf{E}_p(\mathbf{x}, k)$  and  $\mathbf{B}_p(\mathbf{x}, k)$  are the periodic eigenfunctions of the empty slow-wave structure and  $\mathbf{E}_p^{(s)}(\mathbf{x}, k)$  and  $\mathbf{B}_p^{(s)}(\mathbf{x}, k)$  are the "space-charge" fields. The space-charge fields represent the first-order correction (in beam density) to the vacuum fields and contain both a periodic dependence due to the corrugations and a slow dependence [analogous to that imparted by the envelope  $\epsilon(z, t)$  to the vacuum fields], reflecting the degree of bunching at a particular point in the interaction region. Note that the space-charge fields are also modulated by an exponential with wave number  $k$  and frequency  $\omega$ . This is due to the fact these fields are the responses to the bunched beam, which is moving with speed  $v_z \approx \omega/k$ . A more detailed treatment of the space-charge field will be given in Appendices A and B.

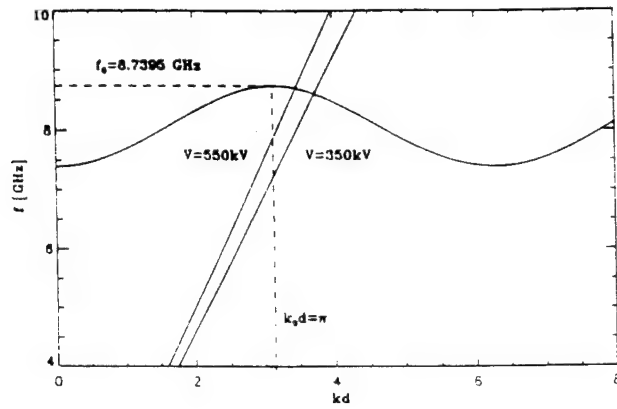


FIG. 1. A schematic picture of a cold-structure dispersion  $\omega(k)$  of a  $TM_{01}$  mode of an infinitely long periodic structure. The straight lines that intersect the dispersion curve are the electron beam Doppler lines,  $\omega = kv_{g0}$ , where  $v_{g0}$  is the initial beam velocity. The two Doppler beamlines correspond to beam voltages of 550 and 350 kV.

The periodic eigenfunctions of the slow-wave structure satisfy Maxwell's equations for a wave of frequency  $\omega$  and Floquet wave number  $k$ , namely

$$-\frac{i\omega}{c} \mathbf{E}_p = \nabla \times \mathbf{B}_p + ik\hat{z} \times \mathbf{B}_p, \quad (3a)$$

$$\frac{i\omega}{c} \mathbf{B}_p = \nabla \times \mathbf{E}_p + ik\hat{z} \times \mathbf{E}_p, \quad (3b)$$

where  $\hat{z}$  is the unit vector in the axial direction. The solution to (3a) and (3b) with the boundary condition that the tangential component of  $\mathbf{E}_p$  vanishes at the metal wall gives the cold-structure dispersion relation,  $\omega(k)$ . For example, consider an empty corrugated structure with period  $d$  and wall radius  $r(z) = r_{av}[1 - \Delta \cos(2k_0 z)]$ , where  $r_{av}$  is the average wall radius and  $k_0 = \pi/d$  is the wave number at the "π" point. The dispersion curve for the lowest axisymmetric mode of this structure is plotted in Fig. 1 for the case where  $r_{av} = 1.5$  cm,  $\Delta = 0.1$ , and  $d = 1.67$  cm. Also shown are the beam dispersion curves for two values of the beam's axial velocity,  $v_z$ , corresponding to energies of 350 and 550 kV. The significance of these curves will be discussed subsequently.

To determine the equations governing the slowly varying amplitude of the electromagnetic fields, one substitutes (1) and (2) into Maxwell's equations,

$$\frac{1}{c} \frac{\partial \mathbf{E}}{\partial t} = \nabla \times \mathbf{B} - \frac{4\pi}{c} \mathbf{j}, \quad (4a)$$

$$-\frac{1}{c} \frac{\partial \mathbf{B}}{\partial t} = \nabla \times \mathbf{E}. \quad (4b)$$

Then one subtracts the dot product of (4a) with  $\mathbf{B}_p^*$  from the dot product of (4b) with  $\mathbf{E}_p^*$  and integrates over the volume contained in one period of the structure. Using (3a) and (3b), the periodicity of  $\mathbf{E}_p$ ,  $\mathbf{E}_p^{(s)}$ ,  $\mathbf{B}_p$  and  $\mathbf{B}_p^{(s)}$ , and the boundary condition that the tangential component of the electric field vanishes on the metal wall, the following slowly varying amplitude equation is obtained:<sup>4,6</sup>

$$\frac{\partial \epsilon}{\partial t} + v_g \frac{\partial \epsilon}{\partial z} = - \int dz' \int d^2x_\perp \frac{\mathbf{E}_p^* \cdot \mathbf{J} e^{-i(kz' - \omega t)}}{U}, \quad (5)$$

where the group velocity was shown to be<sup>4,6</sup>

$$v_g = \frac{c}{4\pi} \int dz' \int d^2x_\perp \hat{z} \cdot \frac{(\mathbf{E}_p \times \mathbf{B}_p^* + \mathbf{E}_p^* \times \mathbf{B}_p)}{U}, \quad (6)$$

the normalized energy stored in one period of the structure is given by

$$U = \frac{1}{4\pi} \int dz' \int d^2x_\perp (|\mathbf{E}_p|^2 + |\mathbf{B}_p|^2), \quad (7)$$

and  $\mathbf{J}$  is the component of the current oscillating at  $\omega$ . The integrals in (5), (6), and (7) are carried out over the volume contained in one period of the structure. The integrands in (6) and (7) are strictly periodic in  $z$ , and there is no ambiguity in the evaluation of the integral. In the case of (5) the integral is carried out over the range of  $z'$  values of length  $d$ , the period of the structure, centered about the point  $z$ . The formal basis for this type averaging is presented in Appendix A. To be specific, we note that in the case of a symmetric structure the volume integral may be written as

$$\int dz' \int d^2x_\perp = \int_z^{z+d} dz' \int_0^{r_w(z')} r dr \int_0^{2\pi} d\phi.$$

When operating far away from the "π" point (for example, with the lower beam voltage of Fig. 1), the dispersion relation of the cold structure can be approximated by a straight line with slope  $v_g$ , which is constant. This is the situation that has been treated previously, and is well described by (5). As the operating point moves closer to the zero group velocity point as the voltage is raised (for example, with the higher beam voltage of Fig. 1), the straight line approximation breaks down and (5) requires modification. A rigorous derivation of the amplitude equations for this case is presented in Appendix A. Here we present a heuristic derivation that yields the same result. Near the upper edge of the transmission band the dispersion relation is approximated by the parabola

$$\omega(k) = \omega_0 + \frac{1}{2} \frac{\partial v_g}{\partial k} (k - k_0)^2, \quad (8)$$

where  $\omega_0$  and  $k_0$  are the frequency and wave number at the "π" point (zero group velocity), and  $\partial v_g / \partial k$  is a negative constant. Thus, in this range of wave numbers we have  $v_g(k) = (k - k_0) \partial v_g / \partial k$ . We now regard  $k$  as an operator, which near the "π" point, is written as  $k = k_0 - i\partial/\partial z$ , where the derivative with respect to  $z$  operates on the slowly varying envelope. The correct generalization of (5) is obtained by replacing  $v_g \partial/\partial z$  in (5) by the following:

$$v_g \frac{\partial}{\partial z} \rightarrow i[\omega(k) - \omega_0] \approx \frac{-i \partial v_g(k_0)}{2} \frac{\partial^2}{\partial z^2}. \quad (9)$$

Substituting (9) into (5), we obtain the following slowly varying amplitude equation:

$$\frac{\partial \epsilon}{\partial t} - \frac{i}{2} \frac{\partial v_g}{\partial k} \frac{\partial^2 \epsilon}{\partial z^2} = - \int dz' \int d^2 x_1 \frac{\mathbf{E}_p^* \cdot \mathbf{J} e^{-i(k_0 z' - \omega_0 t)}}{U}, \quad (10)$$

where

$$\frac{\partial v_g}{\partial k} = \frac{c}{4\pi} \int dz' \int d^2 x_1 \hat{z} \cdot \frac{\partial (\mathbf{E}_p \times \mathbf{B}_p^* + \mathbf{E}_p^* \times \mathbf{B}_p)}{\partial k} \frac{1}{U}. \quad (11)$$

Equation (10) is the envelope equation for an electromagnetic wave driven by a source term that represents the interaction of the cold-structure fields with an electron beam current. The envelope varies slowly in space compared to the period of the structure  $d$  and the wavelength  $2\pi/k$ , and varies slowly in time compared to  $2\pi/\omega$ . The boundary conditions for the slowly varying amplitude that are to be applied at both ends of the structure, are of the form

$$\frac{\partial \epsilon}{\partial z} (z=0) = ik_{b0} \epsilon(z=0), \quad (12a)$$

$$\frac{\partial \epsilon}{\partial z} (z=L) = -ik_{b1} \epsilon(z=L), \quad (12b)$$

where  $k_{b0}$  and  $k_{b1}$  are parameters that depend on the coupling of the fields inside and outside the structure. By analogy to the theory of transmission lines, these quantities can be thought of as admittances describing the fields outside the structure. These boundary admittances can be written in terms of the reflection coefficients at the ends of the periodic structure. Consider the following slowly varying amplitude:

$$\epsilon = \epsilon_- e^{i(\Delta k z + \Delta \omega t)} + \epsilon_+ e^{-i(\Delta k z - \Delta \omega t)}, \quad (13)$$

where  $\epsilon_{\pm}$  represent the forward and backward propagating waves, and  $\Delta k$  and  $\Delta \omega$  represent the shift in the wave number and frequency away from the " $\pi$ " point. Inserting the above expression into the boundary conditions (12a) and (12b), one obtains the following expression for the reflection coefficient:

$$R_i = \frac{\Delta k - k_{bi}}{\Delta k + k_{bi}}, \quad (14)$$

for  $i=0,1$ , where  $R_0 = \epsilon_+/\epsilon_-$  and  $R_1 = e^{i2\Delta k L} \epsilon_-/\epsilon_+$ , corresponding to the reflection at  $z=0$  and  $z=L$ , respectively. As the wave number approaches  $k_0$ ,  $\Delta k$  goes to zero and the reflection  $R_i$  goes to  $-1$ . Now suppose that the reflection coefficient  $R_i(k)$  has been determined by some other means. For example, the reflection coefficient for sinusoidally rippled waveguides connected to waveguides of constant wall radius has been determined numerically in Ref. 7. It is found that  $R_i(k) \rightarrow -1$  as  $k \rightarrow k_0$ , the wave number at the " $\pi$ " point. The boundary condition parameter  $k_{bi}$  can then be determined by solving (14), assuming  $R_i(k)$  is known and taking the limit as  $k \rightarrow k_0$ ,

$$k_{bi} = \lim_{k \rightarrow k_0} (k - k_0) \frac{1 - R_i(k)}{1 + R_i(k)}. \quad (15)$$

By doing this one obtains a unique value for the boundary admittances valid for operation near cutoff.

From (15) one sees that the boundary admittance is a measure of how the magnitude of reflection coefficient for a particular structure goes to unity as the operating wave number approaches  $k_0$ , the wave number at cutoff. Large values of the boundary admittance correspond to structures with large values of the magnitude of the reflection coefficients for all operating wave numbers under consideration, whereas small values of the boundary admittance correspond to structures with low reflection coefficients, except when operating near the cutoff.

To evaluate the source term in (10) we need to characterize the electron beam current. Consider an annular electron beam immersed in a strong magnetic field. Assuming the beam has initially only an axial component of momentum and the magnetic field confines the motion of the electrons along the  $z$  axis, then only the interaction of the axial current with the axial electric field needs to be considered. For synchronism between the electromagnetic fields and the electron beam, we pick out the component of the current that varies as  $e^{-i\omega_0 t}$ . Therefore, we average the current as follows:

$$\mathbf{J}_e i\omega_0 t = \hat{z} \frac{\omega_0}{2\pi} \int_0^{2\pi/\omega_0} dt j_z e^{i\omega_0 t}. \quad (16)$$

The current due to an annular electron beam with radius  $r_b$  can be written as follows:

$$j_z = q \int_{-\infty}^{\infty} \frac{p_z}{\gamma(p_z) m_0} f(z, p_z, t) \frac{\delta(r - r_b)}{2\pi r} dp_z, \quad (17)$$

where  $f(z, p_z, t)$  is the nonthermal electron distribution function defined as

$$f(z, p_z, t) = n_0 v_{z0} \int_{-\infty}^{\infty} dt_0 \delta[z - z(t, t_0)] \delta[p_z - p_z(t, t_0)], \quad (18)$$

where  $n_0$  is the initial electron density per unit length,  $v_{z0}$  is the initial axial electron velocity and  $z(t, t_0)$  and  $p_z(t, t_0)$  are the position and momentum, respectively, of a particle at time  $t$  that entered the interaction region of the structure at time  $t_0$ .

Substituting the above expression for the current into (10) and then normalizing the equation, we arrive at the following slowly varying amplitude equation:

$$2 \frac{\partial a}{\partial \tau} + i \frac{\partial^2 a}{\partial \xi^2} = -\hat{I} \langle e^{-i\psi} \rangle \psi_0, \quad (19)$$

with the following normalized boundary conditions:

$$\frac{\partial a}{\partial \xi} (\xi=0) = ik_{b0} L a(\xi=0), \quad (20a)$$

$$\frac{\partial a}{\partial \xi} (\xi=1) = -ik_{b1} L a(\xi=1), \quad (20b)$$

where  $\psi = k_0 z - \omega_0 t$  is the electron phase,  $\xi = z/L$  is the normalized axial distance,  $\tau = |\partial \beta_g / \partial k| L |ct/L|$  is the normalized time, and  $a(z, t) = q L \bar{E}_{zp}(r_b) \epsilon(z, t) / mc^2$  is the normalized amplitude. Here we have assumed that  $\partial v_g / \partial k < 0$ ,

appropriate to the upper edge of the transmission band. The angled bracket denotes the average over the initial phase of the electrons with respect to the high-frequency field. In addition, we have introduced a normalized current defined as

$$\hat{I} = 8\pi \left( \frac{I}{I_A} \right) \left( \frac{L}{d} \right)^2 \frac{C(r_b)}{|\partial \beta_g / \partial k| L}, \quad (21)$$

where  $I_A = mc^3/q = 1.7 \times 10^4$  A and  $C(r_b)$  is the coupling coefficient. The coupling coefficient is a measure of how well the electromagnetic fields of the cold-structure couple to the electron beam. The coupling coefficient is defined as

$$C(r_b) = \frac{d \left| \int_0^d dz E_{zp}(r_b, z) \right|^2}{\int_0^d \int_0^{r_w(z)} 2\pi r dr dz \left[ \left| E_p(r, z) \right|^2 + \left| B_p(r, z) \right|^2 \right]}, \quad (22)$$

where the numerator is the square of the average of the axial electric field over one period of the structure and the denominator is the total electromagnetic field energy stored in one period of the structure. For our model we use the value of the coupling coefficient at the radius of the electron beam for the cold structure electromagnetic fields with frequency  $\omega_0$  and wave number  $k_0$ .

An electron in the beam is characterized by its phase  $\psi = k_0 z - \omega_0 t$  and its energy  $mc^2 \gamma$ , where  $\gamma = (1 - v^2/c^2)^{-1/2}$ . Since the electron beam is assumed to be immersed in a strong axial magnetic field, only motion in the axial direction is considered. As the beam travels through the interaction region, its phase and energy evolve according to

$$\frac{\partial \psi}{\partial t} + v_z \frac{\partial \psi}{\partial z} = k_0 v_z - \omega_0, \quad (23)$$

$$\frac{\partial \gamma}{\partial t} v_z + v_z \frac{\partial \gamma}{\partial z} = \frac{q}{m} (\epsilon E_{zp} + E_{zp}^{(s)}) e^{i(kz - \omega t)} + \text{c.c.}, \quad (24)$$

where  $q$  is the electron charge. The particles respond strongly only to the synchronous spatial harmonic of the axial electric field. Therefore, in (24), we average the axial electric field over one period of the structure. The quantity  $E_{zp}^{(s)}$  is the axial component of the space-charge field. In Appendix B this field is shown to be proportional to the alternating beam current density,

$$\frac{i\omega}{c} E_{zp}^{(s)} \propto \frac{4\pi}{c} J_z e^{-i(kz - \omega t)}. \quad (25)$$

Consistent with our previous assumption of slow time evolution, the dominant terms in the above equations of motion are the derivatives with respect to the axial coordinate. Here we are basically assuming that the slowly varying field amplitude changes little during the time in which an electron is in the structure. As an estimate, this requires  $\partial \beta_g / \partial (kL) \ll \beta_z$ . With these assumptions the equations of motion reduce to the following:

$$\frac{\partial \psi}{\partial \xi} = k_0 L - \frac{\omega_0 L}{c\beta_z}, \quad (26)$$

$$\frac{\partial \gamma}{\partial \xi} = 2 \operatorname{Re} \left[ \left( a(\xi, \tau) - i \frac{\bar{\omega}_p^2}{\omega_0^2} \langle e^{-i\psi} \rangle_{\psi_0} \right) e^{i\psi} \right]. \quad (27)$$

The space-charge parameter is defined as

$$\bar{\omega}_p^2 = 4\pi \left( \frac{I}{I_A} \right) \left( \frac{k_1^2 L^2}{\omega_0 L/c} \right) C_2 \omega_0^2, \quad (28)$$

where  $C_2$  is the coefficient describing the reduction of the plasma frequency due to the metal wall of the periodic structure. See Appendix B for a precise definition of  $C_2$ . For our calculation we use the coefficient  $C_2$  calculated assuming an annular beam in a smooth waveguide of radius<sup>4,6</sup>  $r_w = r_{av}$ . The analytic expression for  $C_2$  is given by

$$C_2 = \frac{1}{2\pi} I_0(k_1 r_b) K_0(k_1 r_b) \left( 1 - \frac{K_0(k_1 r_w) I_0(k_1 r_b)}{K_0(k_1 r_b) I_0(k_1 r_w)} \right), \quad (29)$$

where  $I_0$  and  $K_0$  are modified Bessel functions and  $k_1^2 = (k_0^2 - \omega_0^2/c^2)$ . This concludes the derivation of our theoretical model. Equations (19), (20), (26), and (27) describe mathematically our model and will be solved numerically to determine the operating frequency and efficiency for two different devices. In the next section we use this model to calculate the starting current for the two devices. In Sec. IV, results from nonlinear simulations will be presented.

### III. STARTING CURRENT

The start current is defined as the current above which the linear gain exceeds losses, and signals are self-excited. Several authors have investigated conditions for self-oscillation near the edge of the transmission band.<sup>9-11</sup> Presented here is both an analytic and numerical calculation for the starting current for a BWO operating near the zero group velocity point. Starting current calculations are presented in Ref. 6 for operation far from the “ $\pi$ ” point. We will compare this starting current calculation based on the linear dispersion curve valid far from the “ $\pi$ ” point with our starting current calculations based on a quadratic curve valid near the “ $\pi$ ” point.

For the analytic calculation of the starting current we assume a fixed field profile for the slowly varying envelope and use perturbation theory to solve the equations of motion for the system. To do this, let us choose the normalized slowly varying amplitude of the electromagnetic waves to have the following form:

$$a(\xi) = a_0 \sin(\Delta k L \xi), \quad (30)$$

where  $\Delta k L = n\pi$  for  $n = 1, 2, \dots, N$ , where  $N$  is the number of periods of the slow-wave structure. Such a field profile will result when the boundary condition parameters  $k_{bi} L$  are very large. Using energy balance for the amplitude equation (19) along with the appropriate boundary conditions (20a) and (20b), the analytic expression for the starting current is



TABLE I. Simulation parameters.

Parameters	Backward wave oscillator	
	X-band BWO	J-band BWO
$f_0$ (GHz)	8.7395	5.8480
$d$ (cm)	1.67	2.15
$N$	8	10 14 35
$r_{av}$ (cm)	1.500	8.440
$r_b$ (cm)	0.775	7.375
$C(r_b)$	$7.24 \times 10^{-2}$	$2.91 \times 10^{-3}$
$k_{y0}d$	$\infty$	1.169
$k_{b1}d$	5.80	1.169
$\partial\beta_z/\partial kd$	-0.4613	-2.6834
$V$ (kV)	300-600	200-900
$I$ (kA)	0.10-0.25	2.0-10.0

$$I_{\text{start}} = \frac{I_A}{4\pi} \left( \frac{d}{L} \right)^3 \frac{c\beta_{z0}^3 \gamma_0^3}{\omega_0 L} \frac{|\partial\beta_z/\partial kd|}{C(r_b)F(\Delta k L)} \times \left( \frac{1}{k_{y0}L} + \frac{1}{k_{b1}L} \right), \quad (31)$$

where the function  $F(\Delta k L)$  is defined as follows:

$$F(\Delta k L) = \frac{G(\kappa_-) - G(\kappa_+)}{\kappa_- \kappa_+ (\kappa_+ + \kappa_-) \sin^2(\kappa_+ + \kappa_-)}, \quad (32)$$

where  $\kappa_{\pm} = [\Delta k \pm (k_0 - \omega_0/v_{z0})]L$  and

$$G(\kappa) = \kappa \frac{\partial}{\partial \kappa} \left( \frac{\sin^2 \kappa}{\kappa^2} \right). \quad (33)$$

In the above calculation we have allowed for outgoing waves (finite  $k_{y0}$  and  $k_{b1}$ ) at both ends of the structure. If at the input of the structure ( $z < 0$ ) modes are cut off [ $a(z=0)=0$ ] then, according to (20a) this case is treated, by allowing  $k_{y0}$  to become infinite.

Equation (31) shows the starting current is inversely proportional to the boundary admittance. This is reasonable, since by (15) a large value of  $k_b$  implies the reflection coefficient is close to unity. As the boundary admittance increases, the starting current of the device decreases. The boundary admittance at the “ $\pi$ ” point is inversely proportional to the slope of the reflection coefficient therefore as the slope approaches zero [corresponding to a constant reflection  $R(k)=1$  for all  $k$ ] more energy is stored in the device. Less energy radiates out of the device, making it easier to start electromagnetic waves oscillating.

Using our model we calculate numerically the starting current for two devices and compare our analytic and numerical results. Table I shows the operating parameters for the two devices. The values of quantities such as frequency, coupling coefficient, boundary condition parameters, and group velocities are obtained using the computer code described in Ref. 7. The first device considered is an X-band BWO. This device has been extensively studied in Refs. 4 and 6, using the model based on a linear dispersion curve (constant  $v_g$ ). However, the assumption that the group velocity is constant breaks down for voltages above 400 kV. As the voltage is increased, the beamline moves toward the “ $\pi$ ” point, where the dispersion curve rolls over.

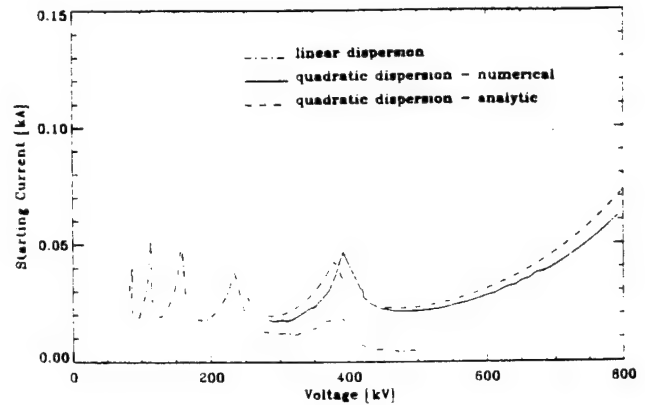


FIG. 2. Starting current versus voltage for the X-band BWO with period length  $d=1.67$  cm, number of periods  $N=8$ , cutoff frequency  $f_0=8.7395$  GHz, average wall radius  $r_{av}=1.50$  cm, and beam radius  $r_b=0.775$  cm.

Therefore, for small changes in voltage the group velocity of the electromagnetic waves is no longer constant. Figure 2 shows the starting current calculation based on the zero group velocity model (both analytic and numerical) and the start current from the model of Refs. 4 and 6. Clearly, the analytic and numerical calculations based on the quadratic dispersion agree very well. As expected, the slowly varying amplitude is very nearly equal to the assumed sine profile. The cusp in the starting current corresponds to a change in the axial mode number. For voltages between 200 and 400 kV the field profile has  $\Delta k L = 3\pi$ , and for voltages greater than 400 kV the field profile has  $\Delta k L = 2\pi$ . For the range of voltage from 300 to 400 kV, the two models (linear and quadratic dispersion) agree well, however, for voltages greater than 400 kV our model near cut-off (quadratic dispersion) is more reliable.

The second device considered here is a J-band BWO. As detailed in Table I, this device operates in the range of voltage, where the dispersion relation for the cold-structure fields is quadratic. The group velocity of the electromagnetic wave is very nearly equal to zero. The previous linear dispersion model is not capable of treating this device. Therefore for this device our “ $\pi$ ” point model is preferable. For this device three lengths,  $N=14, 16, 35$ , periods are studied. Figure 3 shows the analytic and numerical starting currents for the three structures. A discrepancy exists between the two curves because the actual slowly varying field profile obtained from the numerical code differs from the sine wave assumed by the analytic calculation. This discrepancy is shown in the inset figure of Fig. 3 for the 16 period structure. We note that the boundary admittances for this device are not nearly as large as for the X-band BWO. Thus, the assumption of a sinusoidally varying field profile in the analytic calculation is not expected to be as good.

#### IV. NONLINEAR SIMULATIONS

In this section we present the modifications to our theoretical model in order to simulate actual BWO experi-

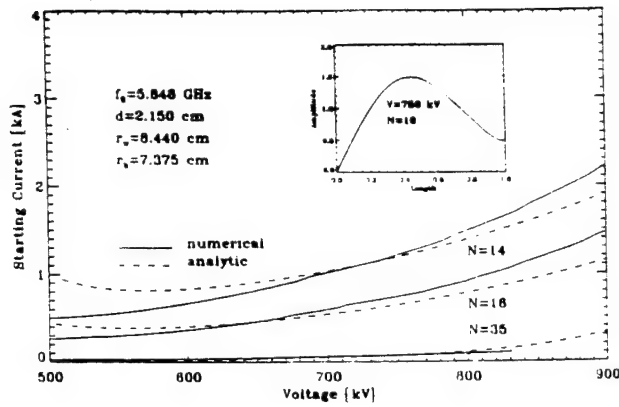


FIG. 3. Starting current versus voltage for the J-band BWO with period length  $d=2.15$  cm, number of periods  $N=14, 16, 35$ , cutoff frequency  $f_0=5.8488$  GHz, beam radius  $r_b=7.375$  cm, and average wall radius  $r_w=8.44$  cm. The profile in the upper right corner is the normalized slowly varying amplitude versus normalized length for voltage  $V=750$  kV.

ments. Comparisons between the nonlinear simulations and experimental results for operating frequency and peak efficiency are shown.

To simulate the BWO experiments, we include in our theoretical model a time-dependent voltage and beam current pulse. We assume a rising exponential for the beam current and voltage, namely

$$I(t) = I_p(1 - e^{-(t+t_p)/t_r})^\rho, \quad (34)$$

$$V(t) = V_p(1 - e^{-(t+t_p)/t_r}), \quad (35)$$

where  $t_r$  is the rise time and  $t_p$ ,  $V_p$ , and  $I_p$  are parameters chosen to best model the characteristics of the beam. We assume the Child–Langmuir law is approximately valid, and let  $\rho=1.5$ . To model the end of the pulse, we assume the voltage and current drop exponentially at some time  $t=t_f$ . In addition, we include the effects of direct current space charge. When the electron beam enters the electromagnetic structure the beam slows down due to a buildup of an electrostatic potential. This voltage depression reduces the electron beam energy. The reduction in the beam energy is calculated using the following formula:<sup>12</sup>

$$\Delta\gamma = 2 \frac{I}{I_A} \ln\left(\frac{r_{av}}{r_b}\right) \left(1 - \frac{1}{(\gamma_0 - \Delta\gamma)^2}\right)^{-1/2}, \quad (36)$$

where  $r_{av}$  is the average wall radius of the corrugated structure and  $r_b$  is the radius of the electron beam. Since the voltage and current are time dependent, the initial value of the relativistic factor  $\gamma_i$  is given by  $\gamma_i = \gamma_0 - \Delta\gamma$ , where  $\gamma_0 = 1 + V(t)/mc^2$ .

The two BWO devices considered here do not operate exactly at the “ $\pi$ ” point, therefore, we made two additional modifications to our theoretical model to more accurately simulate these devices. The first modification to our model was to change the equations of motion to included the frequency shift away from the “ $\pi$ ” point. Equation (26) then becomes

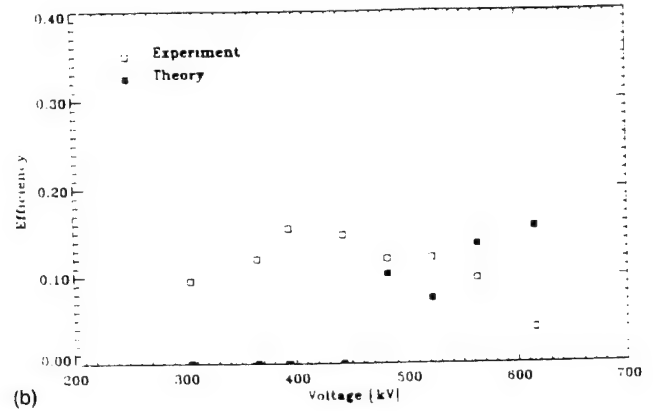
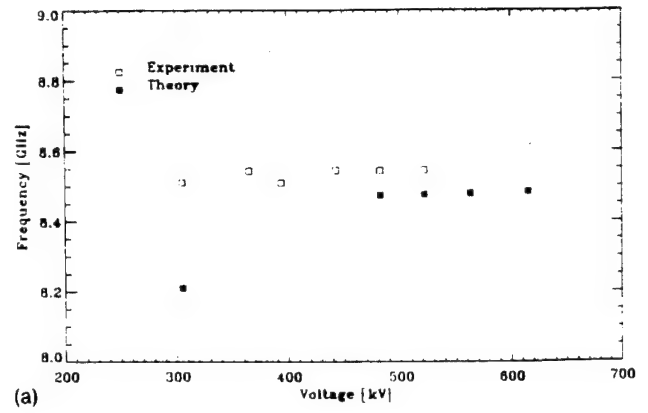


FIG. 4. (a) Operating frequency versus voltage for the X-band BWO with period length  $d=1.67$  cm, number of periods  $N=8$ , cutoff frequency  $f_0=8.7395$  GHz, average wall radius  $r_w=1.50$  cm, and beam radius  $r_b=0.775$  cm. (b) Peak efficiency versus voltage.

$$\frac{\partial\psi}{\partial\xi} = k_0 L - \frac{(\omega_0 + \Delta\omega)L}{c\beta_z}, \quad (37)$$

where  $\Delta\omega$  is the average frequency shift obtained from (19). The slowly varying envelope is a complex quantity representing the amplitude and phase of the wave. The frequency shift  $\Delta\omega$  is the rate of change of the phase of the amplitude,  $a$ . To find  $\Delta\omega$  we multiply (19) by  $a^*$ , integrate over the length, and take the imaginary part to find the average frequency shift. In addition, since the coupling coefficient varies very sharply with wave number near the “ $\pi$ ” point, we included the coupling coefficient as a function of operating wavelength. Therefore, after each correction of the operating frequency we updated the value of the coupling coefficient.

Using our modified code for a finite-duration current and voltage pulse, we compare numerical simulation with experimental results.<sup>5,8</sup> First, consider the X-band BWO with cutoff frequency  $f_0=8.7395$  GHz, period  $d=1.67$  cm, and length  $L=13.36$  cm. Figure 4(a) shows the comparison of the operating frequency versus voltage and Fig. 4(b) shows the comparison of the peak efficiency versus voltage. With the above improvements to our model we obtain very good agreement between the calculated and measured frequencies, as shown in Fig. 4(a). The small discrepancy between the measured and calculated frequen-

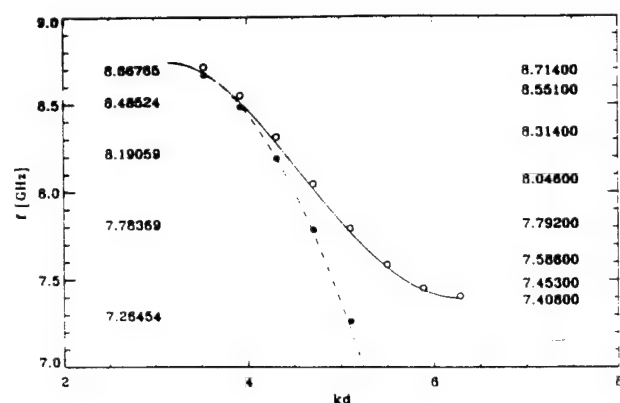


FIG. 5. Axial modes for the X-band BWO with period length  $d=1.67$  cm, number of periods  $N=8$ , cutoff frequency  $f_0=8.7395$  GHz, average wall radius  $r_w=1.50$  cm, and beam radius  $r_b=0.775$  cm. The solid line is the cold-structure dispersion curve, where the open circles represent different axial modes. The dashed line is the parabolic dispersion curve used in the theoretical model for operation near the " $\pi$ " point, where the closed circles represent different axial modes. The frequencies for the axial modes of the cold-structure dispersion are listed on the right and the frequencies for the axial modes of the parabolic dispersion are listed on the left.

cies is explained by the difference between the actual dispersion relation and its parabolic approximation. Figure 5 shows the cold structure dispersion relation with the axial modes for the structure, assuming a shorted boundary condition [ $R(k)=1$ ] at the end. The dotted line shows the assumed parabolic dispersion relation for the structure when operating near the " $\pi$ " point with the corresponding axial modes. For the first three axial modes the quadratic dispersion agrees with the cold-structure dispersion to within 65 MHz.

The simulated frequency for diode voltages below 400 kV is not shown in Fig. 4(a), since in the simulations the device did not start in this range of voltages. It should be noted, however, that if the diode current in the simulations is increased the device will operate with a diode voltage of 365 kV in the third axial mode ( $f=8.19$  GHz, which is not the observed frequency). Additionally, if the duration of the pulse is sufficiently increased (nearly doubled) the device will operate in the second axial mode ( $f=8.48$  GHz) at 365 kV, however, the efficiency is less than 1%. With the diode voltage set to 305 kV, neither raising the current nor lengthening the pulse leads to efficient operation in the second axial mode ( $f=8.19$  GHz). This is a consequence of the fact that for the measured frequency (8.5 GHz) and the wave number inferred from Fig. 5 ( $k=\pi/d+2\pi/L$ ), the resonant energy is 277 kV. Since efficient operation requires the energy of the entering beam exceed the resonant energy by some margin, high efficiency operation at this frequency  $V=305$  kV is not possible. Thus, while the calculated efficiency shows the same basic trend as the experimentally measured efficiency, the calculated efficiency is shifted in voltage by approximately 100 kV. The origin of this shift is under current investigation.

We consider now the J-band BWO with cutoff frequency  $f=5.848$  GHz and period  $d=2.15$  cm. For this

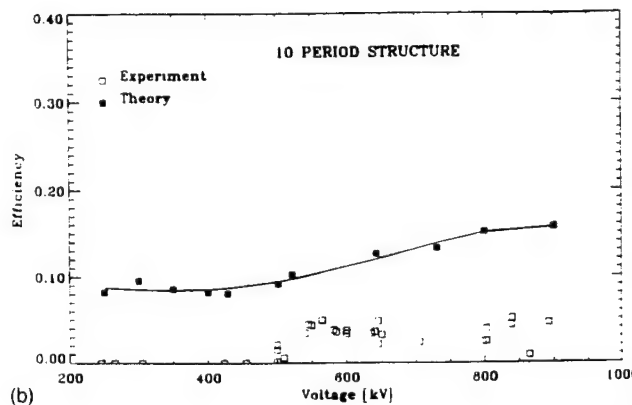
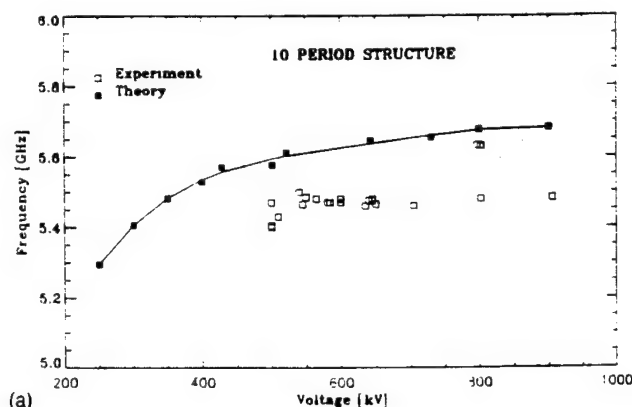


FIG. 6. (a) Operating frequency versus voltage for the J-band BWO with period length  $d=2.15$  cm, number of periods  $N=10$ , cutoff frequency  $f_0=5.8488$  GHz, beam radius  $r_b=7.375$  cm, and average wall radius  $r_w=8.44$  cm. The solid line is the best-fit curve through the simulation points. (b) Peak theoretical efficiency versus voltage.

device we used the experimentally measured voltage and current versus time traces instead of the exponential pulse described by (34) and (35). The operating parameters for this device are presented in Table I. Figures 6(a), 7(a), and 8(a) show the comparison between the measured and calculated frequencies for each of the three structure lengths:  $N=10$ , 14, and 35, respectively.

The simulated and measured frequencies of operation show the same general dependence on beam voltage. Further, both the simulation and experiment show roughly the same frequency shift from the " $\pi$ " point ( $f=5.848$  GHz). The agreement appears to be best for the 35 period structure. While the shorter structures exhibit less variation of frequency with voltage in the experiment than the simulation. This suggests that the effective cavity  $Q$  in the experiment is higher than in the simulation.

The peak theoretical efficiency versus voltage for each of the structures is shown in Figs. 6(b), 7(b), and 8(b), respectively. Results from the experimental study<sup>5</sup> of this device predict peak efficiencies near 5%, based on output power measurements. Numerically calculated efficiencies are between 10%–15%.

Two possible explanations for the relatively large disparity in predicted and measured efficiencies are the following. First, there is a large uncertainty in the measure-



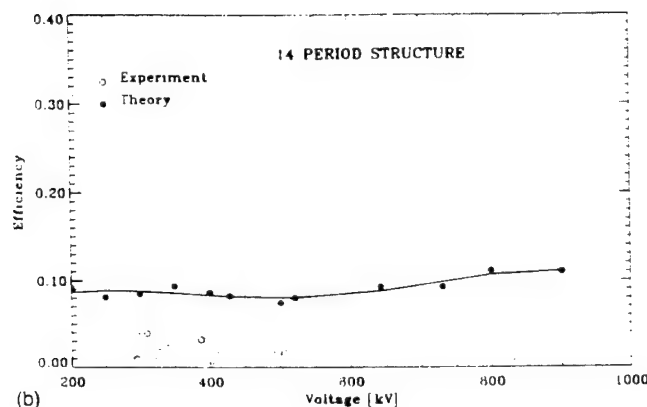
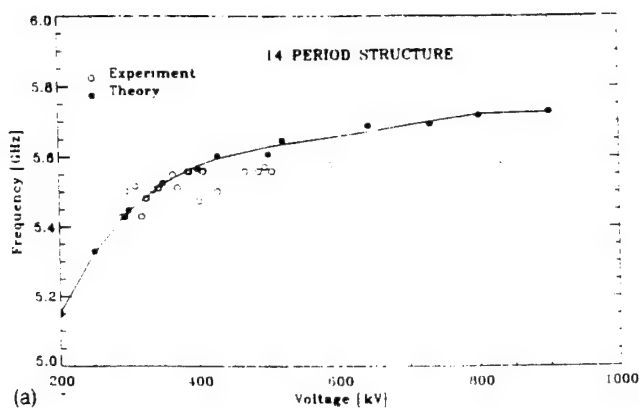


FIG. 7. (a) Operating frequency versus voltage for the J-band BWO with period length  $d=2.15$  cm, number of periods  $N=14$ , cutoff frequency  $f_0=5.8488$  GHz, beam radius  $r_b=7.375$  cm, and average wall radius  $r_w=8.44$  cm. The solid line is the best-fit curve through the simulation points. (b) Peak theoretical efficiency versus voltage.

ment of the experimental efficiencies, as will be described in a forthcoming paper.<sup>13</sup> Second, the theory treats only the lowest-order symmetric, transverse mode of the structure. While this mode is the one that interacts most strongly with the electron beam, the next two symmetric modes may be important as well since they are above cutoff at the operating frequency. These modes will be excited at the discontinuity at the ends of the structure and can affect the transverse field profile of the radiated power. A more complete theory would follow the evolution of these modes as well as the lowest-order mode and include the coupling among the modes at the ends of the device.

## V. SUMMARY

We have used the theoretical model for the operation of a BWO near the edge of the transmission band to calculate starting current for two structures. This model agrees well with the previous model formulated with non-zero group velocity assumptions for operating voltages, where the cold-structure dispersion makes a transition from a linear to a quadratic function of wavelength. After modifying the model near cutoff to include a time-dependent current and voltage, we have simulated two BWO experiments, and compared the predicted and measured results for peak efficiency and operating frequency.

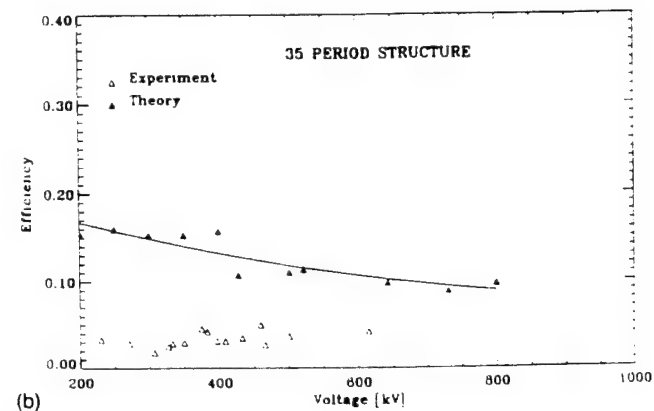
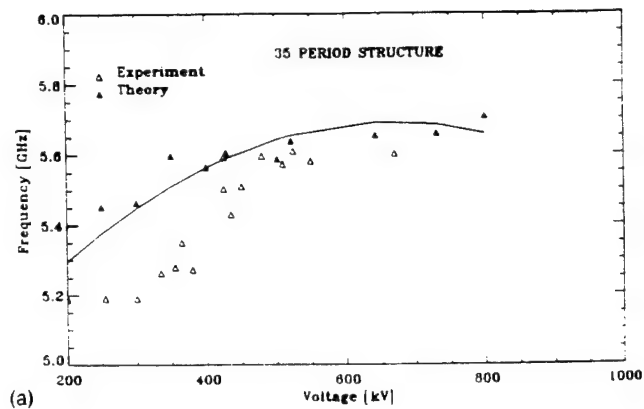


FIG. 8. (a) Operating frequency versus voltage for the J-band BWO with period length  $d=2.15$  cm, number of periods  $N=35$ , cutoff frequency  $f_0=5.8488$  GHz, beam radius  $r_b=7.375$  cm, and average wall radius  $r_w=8.44$  cm. The solid line is the best-fit curve through the simulation points. (b) Peak theoretical efficiency versus voltage.

Predicted and measured frequencies generally agree to within 4%, and show the same dependence on beam voltage. However, predicted and measured efficiencies show various forms of disagreement. In the case of the X-band BWO, the magnitude of the measured and predicted efficiencies are in agreement. However, the peak efficiencies in the two cases occur at different voltages. Various theoretical attempts to induce the "model" BWO to operate at lower voltages failed. Thus, the efficient experimental operation at the reported voltages is unexplained. In the case of the J-band BWO, the predicted efficiency is substantially higher than that which is measured. However, there are large uncertainties in this measurement.<sup>5</sup> Further, the model treats only the lowest-order symmetric mode of the structure. An improved theory that is currently under development will employ a "full-wave" solution for the symmetric electromagnetic fields, including coupling at the output and input ends of the cavity.

## ACKNOWLEDGMENTS

This work was supported by the U.S. Army Research Laboratories and the Air Force Office of Scientific Research.

## APPENDIX A: DERIVATION OF SLOWLY VARYING AMPLITUDE EQUATION

In this appendix we will present a rigorous derivation of the slowly varying amplitude equation used in our numerical simulations. We begin by assuming that the operating point is near the “ $\pi$ ” point and write the electric and magnetic fields in the structure as

$$\mathbf{E}(\mathbf{x}, t) = \hat{\mathbf{E}}(\mathbf{x}, t) e^{i(k_0 z - \omega_0 t)} + \text{c.c.}, \quad (\text{A1})$$

$$\mathbf{B}(\mathbf{x}, t) = \hat{\mathbf{B}}(\mathbf{x}, t) e^{i(k_0 z - \omega_0 t)} + \text{c.c.}, \quad (\text{A2})$$

where  $k_0 = \pi/d$  and  $\omega_0$  is the “ $\pi$ ” point frequency. These expressions are then substituted in Maxwell's equations (4a) and (4b), yielding evolution equations for the complex amplitudes  $\hat{\mathbf{E}}$  and  $\hat{\mathbf{B}}$ ,

$$\frac{1}{c} \frac{\partial \hat{\mathbf{E}}}{\partial t} - \frac{i\omega_0}{c} \hat{\mathbf{E}} = \nabla \times \hat{\mathbf{B}} + ik_0 \hat{\mathbf{z}} \times \hat{\mathbf{B}} - \frac{4\pi}{c} \mathbf{J} e^{-i(k_0 z - \omega_0 t)}, \quad (\text{A3})$$

$$-\frac{1}{c} \frac{\partial \hat{\mathbf{B}}}{\partial t} + \frac{i\omega_0}{c} \hat{\mathbf{B}} = \nabla \times \hat{\mathbf{E}} + ik_0 \hat{\mathbf{z}} \times \hat{\mathbf{E}}. \quad (\text{A4})$$

We now introduce a multiple length and time scale analysis to describe the slow evolution in time and space of the amplitude of the field. Primarily this involves separating the axial dependence of the fields into a fast dependence on the variable  $z_0$  and a slow dependence on the variable  $z_1$ . Here, variations with  $z_0$  will be periodic, with a period equal to that of the structure describing the cold cavity fields, and variations with  $z_1$  will describe the profile of the fields over a distance equal to the length of the structure. Thus, our formal expansion is based on the small parameter  $\delta = d/L$ , where  $d$  and  $L$  are the period and length of the structure, respectively. We then expand the field and axial derivatives in powers of  $\delta$ ,

$$\hat{\mathbf{E}} = \hat{\mathbf{E}}_0 + \hat{\mathbf{E}}_1 + \hat{\mathbf{E}}_2 + \dots, \quad (\text{A5})$$

$$\hat{\mathbf{B}} = \hat{\mathbf{B}}_0 + \hat{\mathbf{B}}_1 + \hat{\mathbf{B}}_2 + \dots, \quad (\text{A6})$$

$$\frac{\partial}{\partial z} = \frac{\partial}{\partial z_0} + \frac{\partial}{\partial z_1} + \dots \quad (\text{A7})$$

The beam current and the time derivative of the fields in (A3) and (A4) will be small quantities; exactly how small will be discussed in a moment. Thus, the lowest-order equations resulting from (A3) and (A4) are

$$-\frac{i\omega_0}{c} \hat{\mathbf{E}}_0 = \nabla_0 \times \hat{\mathbf{B}}_0 + ik_0 \hat{\mathbf{z}} \times \hat{\mathbf{B}}_0, \quad (\text{A8})$$

$$\frac{i\omega_0}{c} \hat{\mathbf{B}}_0 = \nabla_0 \times \hat{\mathbf{E}}_0 + ik_0 \hat{\mathbf{z}} \times \hat{\mathbf{E}}_0, \quad (\text{A9})$$

which are the empty structure equations (3a) and (3b) for  $\omega = \omega_0$  and  $k = k_0$ , which is at the “ $\pi$ ” point. The solution of these equations is

$$\hat{\mathbf{E}}_0 = \mathbf{E}_p(\mathbf{x}, k_0) \epsilon(z_1, t), \quad (\text{A10})$$

$$\hat{\mathbf{B}}_0 = \mathbf{B}_p(\mathbf{x}, k_0) \epsilon(z_1, t), \quad (\text{A11})$$

where  $\epsilon(z_1, t)$  is the amplitude envelope, which is to be determined in higher order.

At this point it is necessary to decide the ordering with respect to the parameter  $\delta$  of all the terms, which we have dropped from the lowest-order version of (A3) and (A4). For example, the theory described in Refs. 4 and 6, which is valid far away from the “ $\pi$ ” point assumes that the slow time derivative and the beam current are first order in  $\delta$ , as is the axial derivative with respect to the variable  $z_1$ . This results in (5), which, as we have seen, cannot be used at the “ $\pi$ ” point due to the vanishing of the group velocity. The resolution is that one must consider the time derivative and the beam current to be second order in  $\delta$ . Physically, this is a consequence of the fact that the dispersion curve is parabolic near the “ $\pi$ ” point, and the frequency depends quadratically on the deviations of the wave number from the “ $\pi$ ” point value. From a formal point of view, we will now have to go to second order in the expansion parameter to obtain the envelope equation.

Proceeding now with our expansion, the first-order version of (A3) and (A4) are written as

$$-\frac{i\omega_0}{c} \hat{\mathbf{E}}_1 = \nabla_0 \times \hat{\mathbf{B}}_1 + ik_0 \hat{\mathbf{z}} \times \hat{\mathbf{B}}_1 + \hat{\mathbf{z}} \times \mathbf{B}_p(\mathbf{x}, k_0) \frac{\partial \epsilon}{\partial z_1}, \quad (\text{A12})$$

$$\frac{i\omega_0}{c} \hat{\mathbf{B}}_1 = \nabla_0 \times \hat{\mathbf{E}}_1 + ik_0 \hat{\mathbf{z}} \times \hat{\mathbf{E}}_1 + \hat{\mathbf{z}} \times \mathbf{E}_p(\mathbf{x}, k_0) \frac{\partial \epsilon}{\partial z_1}. \quad (\text{A13})$$

Equations (A12) and (A13) represent a pair of coupled, inhomogeneous partial differential equations for the first-order fields  $\hat{\mathbf{E}}_1$  and  $\hat{\mathbf{B}}_1$ . It can be verified by differentiation with respect to  $k$  of (3a) and (3b) that the particular solution of (A12) and (A13) is

$$\hat{\mathbf{E}}_1 = -i \left. \frac{\partial \mathbf{E}_p}{\partial k} \right|_{k_0} \frac{\partial \epsilon}{\partial z_1}, \quad (\text{A14})$$

$$\hat{\mathbf{B}}_1 = -i \left. \frac{\partial \mathbf{B}_p}{\partial k} \right|_{k_0} \frac{\partial \epsilon}{\partial z_1}. \quad (\text{A15})$$

The homogeneous solution has the same form as the lowest-order solution of (A10) and (A11) and thus can be absorbed into it.

Proceeding to second order, we find

$$\frac{1}{c} \mathbf{E}_p \frac{\partial \epsilon}{\partial t} - \frac{i\omega_0}{c} \hat{\mathbf{E}}_2 = \nabla_0 \times \hat{\mathbf{B}}_2 + ik_0 \hat{\mathbf{z}} \times \hat{\mathbf{B}}_2 - i\hat{\mathbf{z}} \times \left. \frac{\partial \mathbf{B}_p}{\partial k} \right|_{k_0} \times \frac{\partial^2 \epsilon}{\partial z_1^2} - \frac{4\pi}{c} \mathbf{J} e^{-i(k_0 z_0 - \omega_0 t)}, \quad (\text{A16})$$

$$-\frac{1}{c} \mathbf{B}_p \frac{\partial \epsilon}{\partial t} + \frac{i\omega_0}{c} \hat{\mathbf{B}}_2 = \nabla_0 \times \hat{\mathbf{E}}_2 + ik_0 \hat{\mathbf{z}} \times \hat{\mathbf{E}}_2 - i\hat{\mathbf{z}} \times \left. \frac{\partial \mathbf{E}_p}{\partial k} \right|_{k_0} \frac{\partial^2 \epsilon}{\partial z_1^2}, \quad (\text{A17})$$

where we have made use of (A10), (A11), (A14), and (A15). Taking the dot product of (A16) with  $\mathbf{E}_p^*$  and (A16) with  $\mathbf{B}_p^*$  and then subtracting, we obtain

$$\frac{1}{c} (|\mathbf{E}_p|^2 + |\mathbf{B}_p|^2) \frac{\partial \epsilon}{\partial t} - i\hat{z} \cdot \left( \mathbf{E}_p^* \times \frac{\partial \mathbf{B}_p}{\partial k} \Big|_{k_0} + \frac{\partial \mathbf{E}_p}{\partial k} \Big|_{k_0} \times \mathbf{B}_p^* \right) \frac{\partial^2 \epsilon}{\partial z_1^2} \\ = \nabla \cdot (\hat{\mathbf{B}}_2 \times \mathbf{E}_p^* - \hat{\mathbf{E}}_2 \times \mathbf{B}_p^*) - \frac{4\pi}{c} \mathbf{E}_p^* \cdot \mathbf{J} e^{-i(k_0 z_0 - \omega_0 t)} \quad (\text{A18})$$

In obtaining (A18) we have made use of the complex conjugate of (3a) and (3b). Integrating (A18) over the volume in one period of the structure and dividing through by the electromagnetic energy per  $|\epsilon|^2$  in one period, we obtain the slowly varying amplitude equation,

$$\frac{\partial \epsilon}{\partial t} - \frac{i}{2} \frac{\partial v_g}{\partial k} \frac{\partial^2 \epsilon}{\partial z_1^2} = - \int dz_0 \int d^2 x_1 \frac{\mathbf{E}_p^* \cdot \mathbf{J} e^{-i(k_0 z_0 - \omega_0 t)}}{U} \quad (\text{A19})$$

where

$$U = \frac{1}{4\pi} \int dz_0 \int d^2 x_1 (|\mathbf{E}_p|^2 + |\mathbf{B}_p|^2) \quad (\text{A20})$$

is the electromagnetic energy per  $|\epsilon|^2$  in one period and

$$\frac{\partial v_g}{\partial k} = \frac{c}{4\pi} \int dz_0 \int d^2 x_1 \hat{z} \cdot \frac{\partial}{\partial k} \frac{(\mathbf{E}_p \times \mathbf{B}_p^* - \mathbf{E}_p^* \times \mathbf{B}_p)}{U} \quad (\text{A21})$$

is the derivative of the group velocity with respect to  $k$  at the “ $\pi$ ” point for the vacuum electromagnetic wave. In deriving (A19), we have used the periodicity of  $\mathbf{E}_p$ ,  $\hat{\mathbf{E}}_2$ ,  $\mathbf{B}_p$ , and  $\hat{\mathbf{B}}_2$  and the boundary condition that the tangential component of the electric field vanishes on the metal wall. Equation (A19) is our desired result and is clearly identical to (10), which was derived heuristically in the text.

## APPENDIX B: DEVELOPMENT OF SPACE-CHARGE FIELDS

In Appendix A we introduced an ordering scheme and perturbation expansion for calculation of the fields in a corrugated structure in the presence of an electron beam. The fields are represented as a sum of terms, (A5) and (A6), which constitutes a series expansion in the small parameter  $\delta = d/L$ , where  $d$  and  $L$  are the period and length of the structure, respectively. As discussed in Appendix A, in solving these equations we assumed that the beam current and density was second order in the parameter  $\delta$ . Thus, the lowest-order fields ( $\hat{\mathbf{E}}_0, \hat{\mathbf{B}}_0$ ) and ( $\hat{\mathbf{E}}_1, \hat{\mathbf{B}}_1$ ) [given by Eqs. (A10)–(A11), (A14), and (A15)] represent, essentially, vacuum fields with slowly varying envelopes. The second-order fields ( $\hat{\mathbf{E}}_2, \hat{\mathbf{B}}_2$ ) will contain contributions proportional directly to the local charge and current density. It is these terms that constitute the space-charge fields included in our model.

To obtain these space charge fields we must solve Eqs. (A16) and (A17). To do this, we exploit the variation of parameters technique used to solve the first-order system in

Eqs. (A12) and (A13). We write the second-order fields as the sum of a space-charge field and a second-order correction to the vacuum field,

$$\hat{\mathbf{E}}_2 = \hat{\mathbf{E}}_2^{(s)} - \frac{1}{2} \frac{\partial^2 \epsilon}{\partial z_1^2} \frac{\partial^2 \mathbf{E}_p}{\partial k^2} \Big|_{k_0} \quad (\text{B1})$$

$$\hat{\mathbf{B}}_2 = \hat{\mathbf{B}}_2^{(s)} - \frac{1}{2} \frac{\partial^2 \epsilon}{\partial z_1^2} \frac{\partial^2 \mathbf{B}_p}{\partial k^2} \Big|_{k_0} \quad (\text{B2})$$

and insert these expressions in Eqs. (A16) and (A17). We then use Eq. (A19) to eliminate the term proportional to  $\partial \epsilon / \partial t$  in Eqs. (A16) and (A17). We note that terms proportional to  $\partial^2 \epsilon / \partial z_1^2$  cancel, since they multiply the second derivative of Eqs. (3a) and (3b). That is, by differentiating Eqs. (3a) and (3b) twice with respect to  $k$ , we have the identity

$$-\frac{i \partial^2 \omega}{c \partial k^2} \Big|_{k_0} \mathbf{E}_p - \frac{i \omega_0}{c} \frac{\partial^2 \mathbf{E}_p}{\partial k^2} \Big|_{k_0} \\ = \nabla \times \frac{\partial^2 \mathbf{B}_p}{\partial k^2} \Big|_{k_0} + i k_0 \hat{z} \times \frac{\partial^2 \mathbf{B}_p}{\partial k^2} + 2 i \hat{z} \times \frac{\partial \mathbf{B}_p}{\partial k} \Big|_{k_0} \quad (\text{B3})$$

$$\frac{i \partial^2 \omega}{c \partial k^2} \Big|_{k_0} \mathbf{B}_p + i \frac{\omega}{c} \frac{\partial^2 \mathbf{B}_p}{\partial k^2} \Big|_{k_0} \\ = \nabla \times \frac{\partial^2 \mathbf{E}_p}{\partial k^2} \Big|_{k_0} + i k_0 \hat{z} \times \frac{\partial^2 \mathbf{E}_p}{\partial k^2} + 2 i \hat{z} \times \frac{\partial \mathbf{E}_p}{\partial k} \Big|_{k_0} \quad (\text{B4})$$

After noting the cancellations, the space-charge fields are found to satisfy

$$-\frac{i \omega_0}{c} \hat{\mathbf{E}}_2^{(s)} = \nabla_0 \times \mathbf{B}_2^{(s)} + i k_0 \hat{z} \times \hat{\mathbf{B}}_2^{(s)} - \frac{4\pi}{c} \mathbf{J} e^{-i(k_0 z_0 - \omega_0 t)} \\ + \frac{1}{c} \mathbf{E}_p \int dz_0 \int d^2 x_1 \frac{\mathbf{E}_p^* \cdot \mathbf{J} e^{-i(k_0 z_0 - \omega_0 t)}}{U} \quad (\text{B5})$$

$$+\frac{i \omega_0}{c} \hat{\mathbf{B}}_2^{(s)} = \nabla_0 \times \hat{\mathbf{E}}_2^{(s)} + i k_0 \hat{z} \times \hat{\mathbf{E}}_2^{(s)} \\ - \frac{1}{c} \mathbf{B}_p \int dz_0 \int d^2 x_1 \frac{\mathbf{E}_p^* \cdot \mathbf{J} e^{-i(k_0 z_0 - \omega_0 t)}}{U} \quad (\text{B6})$$

Thus, the space-charge fields  $\hat{\mathbf{E}}_2^{(s)}(z_0, z_1)$  and  $\hat{\mathbf{B}}_2^{(s)}(z_0, z_1)$  are linearly proportional to the beam current. These space-charge fields are referred to in the main text as  $\mathbf{E}_p^{(s)}$  and  $\mathbf{B}_p^{(s)}$ . For the model considered in our paper in which the beam is annular, and the magnetic field restricts the current to point in the axial direction we have, following the steps leading to Eq. (19),

$$\mathbf{J} e^{-i(k_0 z - \omega_0 t)} = \hat{z} \frac{I \delta(r - r_b)}{2\pi r_b} \langle e^{-i\psi(z_1)} \rangle \quad (\text{B7})$$

Note that the “bunching function”  $\langle \exp[-i\psi(z_1)] \rangle$  varies on the slow scale,  $z_1$ , that is, the bunching varies slowly over a distance equal to one period of the structure.

beam can vary by a large amount over the length of the structure. Thus, we may write the space charge fields as a product of the beam current, the bunching factor, and a field profile,  $C_2(\mathbf{x}_1, z_0; r_b)$ , which depends on the geometry of the structure, the operating point, and the location of the beam,

$$\frac{i\omega_0}{c} \mathbf{E}_2^{(s)} = \frac{4\pi I}{c} \left( k_0^2 - \frac{\omega_0^2}{c^2} \right) C_2(\mathbf{x}_1, z_0; r_b) \langle e^{-i\psi} \rangle. \quad (\text{B8})$$

The axial component of this field when evaluated at the beam radius and averaged over axial distance enters the equations of motion in Eq. (24).

It is reasonable to ask the basis for retaining the space-charge field in the interaction, but not retaining the higher-order corrections to the vacuum field. There are two justifications. The first is that the space-charge field produces a qualitatively different interaction with the beam than the vacuum electromagnetic field. This is due to the fact that it is locally proportional to the beam current, unlike the vacuum field, whose effect is integrated over the length of the structure. Thus, including higher-order corrections to the electromagnetic field will not change the results as much as including the space-charge field. The second reason is that the space-charge field, though formally small in the small parameter  $\delta = d/L$ , tends to be peaked at the location of the beam, whereas the synchronous component of the elec-

tromagnetic field tends to be larger at the wall, and depends also on the ripple size. In a device with small ripples the space-charge field can dominate. Thus, we retain only the space-charge field and the lowest-order electromagnetic field.

- <sup>1</sup>A. P. Kuznetsov and S. P. Kuznetsov, *Sov. Radiophys. Electron.* **27**, 1575 (1984).
- <sup>2</sup>L. V. Bulgakova and S. P. Kuznetsov, *Sov. Radiophys. Electron.* **31**, 155 (1988).
- <sup>3</sup>L. V. Bulgakova and S. P. Kuznetsov, *Sov. Radiophys. Electron.* **31**, 452 (1988).
- <sup>4</sup>B. Levush, T. M. Antonsen, Jr., A. Bromborsky, W. R. Lou, and Y. Carmel, *IEEE Plasma Sci.* **PS-20**, 263 (1992).
- <sup>5</sup>D. K. Abe, Ph.D. dissertation, University of Maryland, College Park, Maryland, 1992.
- <sup>6</sup>B. Levush, T. M. Antonsen, Jr., A. Bromborsky, W. R. Lou, and Y. Carmel, *Phys. Fluids B* **4**, 2293 (1992).
- <sup>7</sup>A. Bromborsky, *SPIE Intense Microwave Part. Beams III* **1629**, 182 (1992).
- <sup>8</sup>P. Sprangle, C. M. Tang, and W. M. Manheimer, *Phys. Rev. A* **21**, 302 (1980).
- <sup>9</sup>E. A. Galst'yan, S. V. Gerasimov, and N. I. Karbushev, *Radiotekh. Electron.* **5**, 1061 (1990).
- <sup>10</sup>V. I. Kanavets, Yu. D. Mozgovoy, and A. I. Slepko, *Radiotekh. Electron.* **6**, 1178 (1986).
- <sup>11</sup>N. P. Kravchenko, N. L. Romashin, and V. A. Solntsev, *Radiotekh. Electron.* **6**, 1320 (1987).
- <sup>12</sup>L. S. Bogdankevich and A. A. Rukhadze, *Sov. Phys.* **14**, 163 (1971).
- <sup>13</sup>D. K. Abe (private communication, 1992).

# Parametric effect of a spatially periodic voltage depression on operation of Čerenkov sources of electromagnetic radiation

G. S. Nusinovich and A. N. Vlasov<sup>a)</sup>

*Institute for Plasma Research, University of Maryland, College Park, Maryland 20742*

(Received 27 September 1993; accepted 22 November 1993)

In microwave sources of coherent Čerenkov radiation the electrons usually propagate near the rippled wall of a slow-wave structure. These ripples cause the periodic modulation of electron potential depression, and therefore, lead to periodic modulation of electron axial velocities. Since the period of this electrostatic pumping is the period of the slow-wave structure the parametric coupling of electrons to originally nonsynchronous spatial harmonics of the microwave field may occur. This effect can be especially important for backward-wave oscillators (BWO's) driven by high current, relativistic electron beams. In the paper both linear and nonlinear theories of the relativistic resonant BWO with periodic modulation of electron axial velocities are developed and results illustrating the evolution of the linear gain function and the efficiency of operation in the large-signal regime are presented.

## I. INTRODUCTION

Operation of Čerenkov sources of electromagnetic radiation is based on the synchronism between the electron axial velocity,  $v_z$ , and the phase velocity of the electromagnetic wave,  $v_{ph}$ . To provide this synchronism slow-wave structures are used. Usually these structures are made in the form of metallic waveguides with periodically corrugated walls (see Fig. 1). According to the Floquet theorem, the electromagnetic fields of any mode in such a structure can be represented as a superposition of spatial harmonics

$$\mathbf{E} = \sum_s \mathbf{E}_s e^{i(\omega t - [k_0 - s(2\pi/d)]z)} + \text{c.c.} \quad (1)$$

(A similar expression can be written for  $\mathbf{H}$ .) In this equation  $d$  is the structure period,  $\omega$  is the field frequency,  $k_0$  is the axial wave number of the zero spatial harmonic, and  $E_s$  is the harmonic amplitude. The above mentioned condition of synchronism

$$v_z \approx v_{ph} = \omega/k_z, \quad (2)$$

where  $k_z = k_0 - s2\pi/d$ , may be fulfilled either for the zero spatial harmonic (in traveling wave tubes, TWT's) or for the minus first spatial harmonic (in backward wave oscillators, BWO's). Usually the theory of these devices considers only the interaction of electrons with the synchronous harmonic of the electromagnetic field.

During the last 20 years high-power microwave sources based on Čerenkov radiation of relativistic electron beams have been actively studied both theoretically and experimentally (an extensive review of these studies has recently been done by Benford and Swegle<sup>1</sup>). In spite of a large number of publications there is still at least one effect which may be important for operation of these devices but which, as far as we know, has not been analyzed before.

This effect is based on the periodic axial modulation of the velocities of electrons moving linearly along the metallic structure with rippled walls (see Fig. 1).

In principle, depression of electron potential with respect to the applied voltage, which is caused by the finite distance between the electron beam and the accelerating structure wall, is well known and its effect on the operation of relativistic Čerenkov devices has been discussed elsewhere.<sup>2,3</sup> However, usually this effect is treated only as a reduction of the mean value of electron energy.

In fact, for electron beams propagating in a metallic structure with rippled walls, the voltage depression depends also on the electron axial position which leads to axial modulation of electron velocities. The period of this modulation is, obviously, the period of the slow-wave structure  $d$ . Therefore, this modulation may cause the resonance parametric coupling between electrons and other originally nonsynchronous spatial harmonics. Of course, as the current grows, the voltage depression effect becomes more pronounced. There is also another not so obvious reason which makes this effect potentially important for relativistic BWO's. From the scaling laws for Čerenkov microwave sources with ultra-relativistic electron beams<sup>4</sup> it follows that with the increase in operating voltage,  $V_b$ , the optimal amplitude of the synchronous spatial harmonic of the field scales as  $\gamma_0^{-1}$ , where  $\gamma_0 = 1 + eV_b/mc^2$  is the electron Lorentz factor. This tendency becomes distinctive enough at voltages above 300–400 kV.<sup>5</sup> In the case of BWO's the minus first harmonic is synchronous. So, its amplitude becomes smaller as the voltage grows while the amplitude of the zero spatial harmonic becomes larger because the radiated power grows proportionally to the beam power. From here it follows that at high voltages the role of the electrons' interaction with the zero spatial harmonic becomes more important, and this interaction may partly be caused by the above discussed axial modulation of electron velocities.

In a general form this effect was taken into account in Ref. 6 where the dispersion equation for the waves in a waveguide with corrugated walls was derived and the cor-

<sup>a)</sup>Permanent address: Department of Physics, Moscow State University, Moscow 119899, Russia.

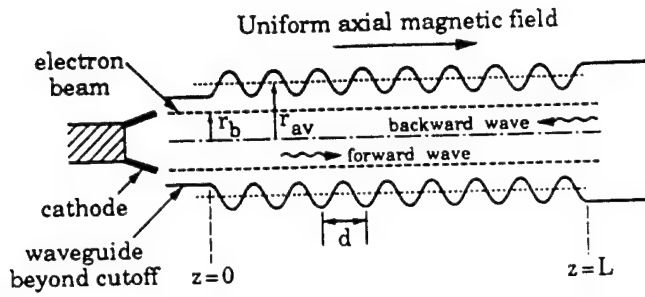


FIG. 1. A schematic picture of a relativistic backward wave oscillator. A thin annular relativistic electron beam of radius  $r_b$  propagates inside of a metallic structure with rippled walls.

responding terms proportional to  $dv_x/dz$  were presented. However, no analysis of the effect has been carried out.

The present paper is aimed at studying the effect of parametric coupling between electrons and the zero spatial harmonic of the field in the simplest model of a relativistic Čerenkov device, the backward wave oscillator with large end reflections. The paper is organized as follows. Section II contains general equations describing the effect. In Sec. III the linear theory is presented. In Sec. IV the stationary nonlinear theory is given. Finally, Sec. V contains the discussion and summary of our results.

## II. GENERAL EQUATIONS

First of all, let us consider the effect of voltage depression on an electron beam propagating near a corrugated metallic wall. Let a thin annular electron beam propagate at a distance from the corrugated wall of the cylindrical waveguide that for all  $z$  is much smaller than the period of corrugation,  $d$ . In such a case, which corresponds to the condition

$$\Delta, l \ll d, \quad (3)$$

where  $\Delta$  is the distance between the average radius of the wall,  $r_{av}$ , and the electron beam radius,  $r_b$ , and  $l$  is the height of corrugation (see Fig. 1), the axial modulation of voltage depression can be considered locally, which leads to the standard definition of electron energy depression

$$\gamma_0 - \gamma = \frac{2I_b}{mc^3/e} \frac{1}{\sqrt{1-\gamma^{-2}}} \ln \frac{r_w}{r_b}. \quad (4)$$

In this equation  $I_b$  is the electron current, and the waveguide radius  $r_w$  is a slowly varying function of  $z$ . For small voltage depression we can assume that in the right-hand side of Eq. (4),  $\gamma \approx \gamma_0$ . Also, supposing that the sizes  $\Delta$  and  $l$  are small not only in comparison with  $d$ , as given by Eq. (3), but also with the beam radius,  $r_b$ , we can expand  $\ln(r_w/r_b)$  in the form

$$\ln \frac{r_w}{r_b} \approx \frac{\Delta}{r_b} - \frac{l}{r_b} \cos\left(\frac{2\pi}{d} z\right). \quad (5)$$

The latter expression is given for the wall corrugation in the form  $r_w = r_b + \Delta - l \cos(2\pi z/d)$ . Correspondingly, the depression of the beam potential can be described by a simple equation for  $\Delta\gamma = \gamma_0 - \gamma$ :

$$\Delta\gamma = 2 \frac{eI_b}{mc^3\beta_{x0}} \frac{1}{r_b} \left[ \Delta - l \cos\left(\frac{2\pi}{d} z\right) \right]. \quad (6)$$

Here the initial electron velocity normalized to the speed of light is equal to  $\beta_{x0} = \sqrt{1-\gamma_0^{-2}}$ . As follows from Eq. (6), the effect of energy depression is rather small. However, it may play an important role in phase relations between electrons and synchronous spatial harmonic of the wave. Indeed, by introducing, according to Eq. (1), the phase of an electron with respect to the minus first harmonic as  $\phi = \omega t - [k_0 + (2\pi/d)z]$ , where electrons  $z$  and  $t$  are related as  $dz/dt = v_z$ , one can obtain the standard equation for  $d\phi/dz$ :

$$\frac{d\phi}{dz} = \frac{1}{\beta_z} - \frac{k_0 + 2\pi/d}{\omega/c}.$$

Here the axial coordinate  $z$  is normalized to  $\omega/c$ .

Correspondingly, by introducing the mean value of electron energy, which accounts for energy depression

$$\gamma_{d.m.} = \gamma_0 - 2 \frac{eI_b}{mc^3} \frac{1}{\beta_{x0}} \frac{\Delta}{r_b}, \quad (7)$$

(cf. Eq. 6), the mean value of the electron unperturbed normalized velocity,

$$\bar{\beta}_{x0} = \sqrt{1-\gamma_{d.m.}^{-2}},$$

and the mean mismatch of synchronism,

$$\delta = \frac{1}{\bar{\beta}_{x0}} - \frac{k_0 + 2\pi/d}{\omega/c},$$

one can rewrite the equation for the phase  $\phi$  in the form

$$\frac{d\phi}{dz} = \delta + \frac{1}{\beta_z} - \frac{1}{\bar{\beta}_{x0}}. \quad (8)$$

The equation for the electron energy should include the periodic modulation of energy depression [see Eq. (6)] and the field of the nonsynchronous, zero spatial harmonic. The latter could be important because, as was mentioned in the Introduction, in relativistic BWO's the amplitude of this harmonic can be much larger than the amplitude of the synchronous, minus first harmonic. Therefore, in spite of the lack of synchronism, the effect of the nonsynchronous interaction with the large amplitude harmonic can be comparable to that of the synchronous interaction with the small amplitude harmonic. Correspondingly, by representing the axial component of the electric field acting on electrons in the form

$$E_z = \text{Re} \left[ E_{-1} e^{i\phi} \left( 1 + \frac{E_0}{E_{-1}} e^{i(\lambda z/d)} \right) \right]$$

(here  $z$  is normalized to  $\omega/c$ ,  $\lambda$  is the wavelength), one can obtain for the normalized energy  $\gamma$  the following equation:

$$\frac{d\gamma}{dz} = -I(\gamma_0^2 - 1)^{3/2} \frac{\bar{h}}{L} \sin(\bar{h}z) - \text{Re} [A e^{i\phi} (1 + \bar{h} L q e^{i\bar{h}z})]. \quad (9)$$

Here



$$I = \frac{eI_b}{mc^3} \frac{1}{\beta_0(\gamma_0^2 - 1)^{3/2}} \frac{l}{r_b} L$$

is the normalized beam current parameter responsible for axial modulation of electron energies and velocities near the ripple structure,  $L$  is the normalized length of a structure,  $\bar{h} = 2\pi c/\omega d$  is the normalized axial wave number of the slow-wave structure,  $\bar{h}L = 2\pi N$ , where  $N$  is the number of structure periods,  $A = eE_{-1,z}/mc\omega$  is the normalized amplitude of the synchronous spatial harmonic, and the ratio of harmonic amplitudes is presented as  $E_{0,z}/E_{-1,z} = \bar{h}Lq$ . Note that since both the ratio  $E_{0,z}/E_{-1,z}$  in relativistic BWO's and  $\bar{h}L$  are large, the parameter  $q = E_{0,z}/2\pi NE_{-1,z}$  which describes the effect of a large amplitude, nonsynchronous zero spatial harmonic, may have an arbitrary value. Also note that when the condition given by Eq. (3) is fulfilled, the ratio of harmonic amplitudes  $E_{0,z}/E_{-1,z}$  introduced by Eq. (1) may be found from formulas given in Ref. 7:

$$\frac{E_{0,z}}{E_{-1,z}} = \frac{2g_0}{[g_0^2 + k_0(2\pi/d)]l} \frac{I_0(p_{-1}r_{av})}{J_1(g_0r_{av})} \frac{J_0(g_0r_b)}{I_0(p_{-1}r_b)}. \quad (10)$$

Here  $g_0$  is the transverse wave number for the fast-wave zero spatial harmonic and  $p_{-1}$  is related to the transverse wave number of the minus first, slow wave spatial harmonic,  $g_{-1}$ , by  $g_{-1} = ip_{-1}$ . From Eq. (10), it follows that the ratio of harmonic amplitudes can be positive or negative.

In comparison with the standard equation for electron energy in backward wave oscillators with negligibly small space charge forces (see, e.g., Refs. 4 and 5), Eq. (9) contains two additional terms responsible, respectively, for spatial modulation of electron energy depression and for interaction with the zero spatial harmonic of the wave.

The boundary conditions for equations of electron motion (8) and (9) are  $\phi(0) = \phi_0 \in [0; 2\pi]$  and  $\gamma(0) = \gamma_0$ . The efficiency of interaction between the electrons and the electromagnetic field is

$$\eta = \frac{1}{\gamma_0 - 1} \left( \gamma_0 - \frac{1}{2\pi} \int_0^{2\pi} \gamma(L) d\phi_0 \right). \quad (11)$$

In principle, the equations for the electron motion should be supplemented with the equations defining the amplitude of the electromagnetic field, which varies along  $z$  when at least one end of the structure is opened (as shown in Fig. 1). However, below we shall restrict our consideration to the simplest model of a resonant Čerenkov device with strong reflections at both ends of the interaction region. In such a system the amplitude of the field acting on electrons is practically independent of  $z$  and can be determined by a standard balance equation between the microwave power radiated by an electron beam and the power of microwave diffractive and Ohmic losses.

### III. LINEAR THEORY

To develop the linear theory one has to linearize the equations for electron motion (8) and (9) with respect to

the field amplitude  $A$ . Zeroth-order terms lead us to the expression for the electron energy given by Eq. (6) and for the phase  $\phi$ :

$$\phi_{(0)} = \phi_0 + \delta z - \frac{2eI_b}{mc^3\beta_0(\gamma_0^2 - 1)^{3/2}} \frac{1}{\bar{h}} \frac{l}{r_b} \sin\left(\frac{2\pi}{d}z\right). \quad (12)$$

Then, linearizing Eqs. (8) and (9) one can find the first-order terms in  $\gamma$  and  $\phi$ . However, after averaging over initial phase  $\phi_0$  in Eq. (11) these terms will not contribute to energy exchange between the electron beam and the microwave field. Therefore, it is necessary to take into account the second-order terms in perturbations in electron energy. The corresponding formalism has been described in detail elsewhere,<sup>8</sup> so we will present here only the final expression for the electron efficiency defined in the frame of the linear theory:

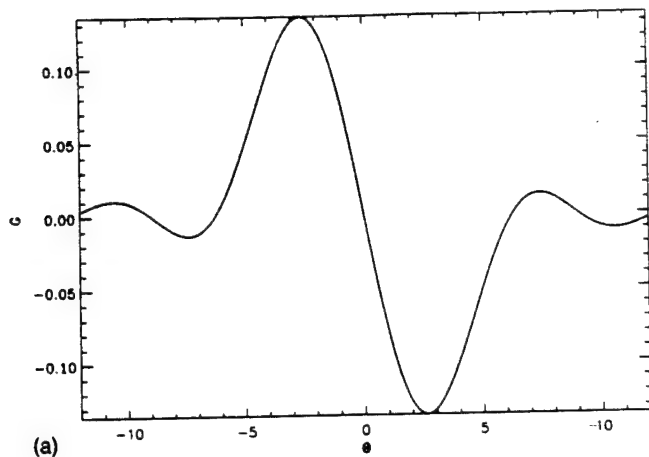
$$\eta_{\text{LIN}} = \frac{A^2 L^3}{2(\gamma_0 - 1)(\gamma_0^2 - 1)^{3/2}} \mathcal{F}(\theta, q, I). \quad (13)$$

Here the function  $\mathcal{F}$  depends on the electron transit angle through the interaction region,  $\theta = \delta L$ , on the parameter  $q$  responsible for the interaction with the zero spatial harmonic of the microwave field, and on the normalized beam current parameter  $I$  describing the effect of axial modulation of electron velocities by rippled walls:

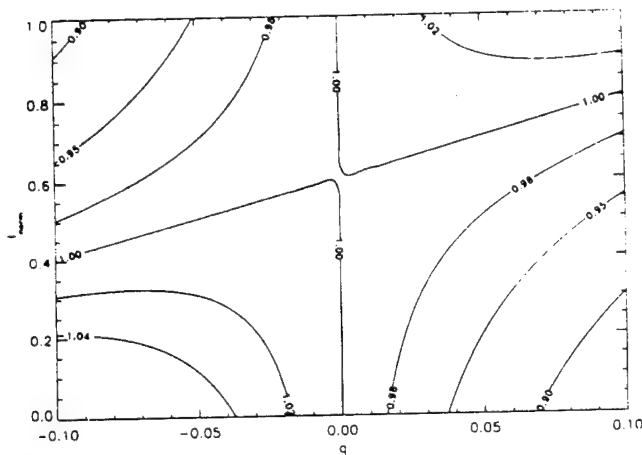
$$\mathcal{F}(\theta, q, I) = \frac{1 + q(I + \theta)}{\theta^3} \{ \theta \sin \theta [1 + q(I + \theta)] - 2(1 - \cos \theta)(1 + qI) \}. \quad (14)$$

This expression is valid for any structure containing an integer number of periods,  $d$ . Note that among the terms accounting for parametric resonance with nonsynchronous spatial harmonics only the terms responsible for interaction with the large-amplitude zero spatial harmonic are accounted for here. When both new effects, interaction with the zero spatial harmonic and axial modulation of electron velocities, are negligibly small ( $q \rightarrow 0, I \rightarrow 0$ ), Eq. (14) is reduced to the standard gain function well known in the theory of the "O" type, linear beam devices. When we neglect only the effect of axial modulation of electron velocities, the effect of interaction with the zero spatial harmonic still exists [see Eq. (14) for  $I = 0, q \neq 0$ ]. However, if we neglect the effect of interaction with the zero spatial harmonic ( $q = 0$ ), the parameter  $I$  does not play any role in Eq. (14); that demonstrates the parametric nature of this effect.

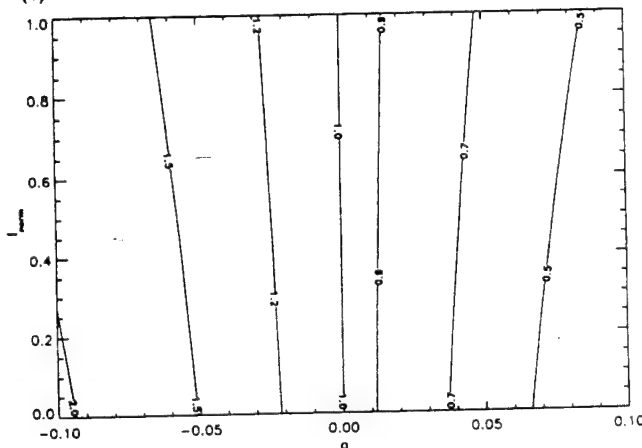
In order to illustrate the effect of the two new parameters presented in Eq. (14), let us give some results of the linear analysis. In Fig. 2(a) the standard linear gain function is shown for the case  $q = I = 0$  as the function of the transit angle  $\theta$ . In Figs. 2(b) and 2(c) the lines of equal ratios of gain functions  $\mathcal{F}/\mathcal{F}(q = I = 0)$  are given in the plane of these parameters  $q$  and  $I$ . Figure 2(b) corresponds to the transit angle  $\theta = -2.62$  which gives the maximum linear gain function for  $q = I = 0$ . Figure 2(c) corresponds to  $\theta = -5$ , where operation with the high efficiency can be realized, as will be shown below. In the case shown in



(a)



(b)



(c)

FIG. 2. (a) Standard linear gain function in the absence of new effects. (b) and (c) The lines of equal ratios of linear gain functions  $\mathcal{F}(q, I)/\mathcal{F}(q=0, I)$  in the plane of normalized parameters proportional to the axial modulation of electron potential ( $I$ ) and to the coupling with the zero spatial harmonic of the microwave field ( $q$ ). In (b) electron transit angle  $\theta = -2.62$ , which corresponds to the minimum starting current; in (c)  $\theta = -5$ , which corresponds to highly efficient operation.

Fig. 2(b) the changes in the linear gain function are small while in the case shown in Fig. 2(c), the effect is much more pronounced. As follows from Fig. 2(c), the main role is played by the interaction with the zero spatial harmonic. At negative  $q$  this effect reduces starting currents and vice versa.

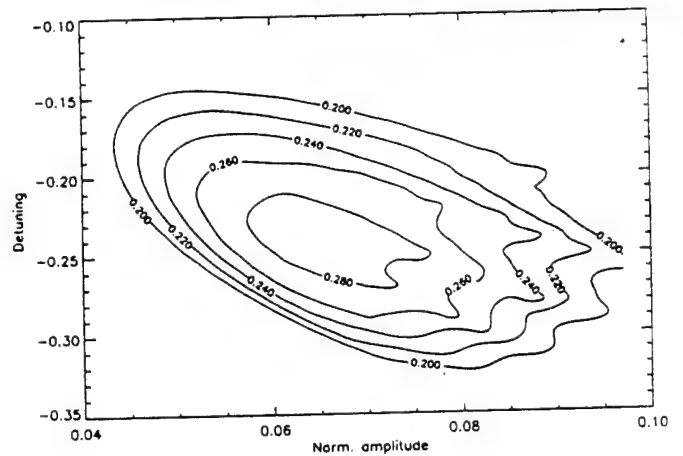
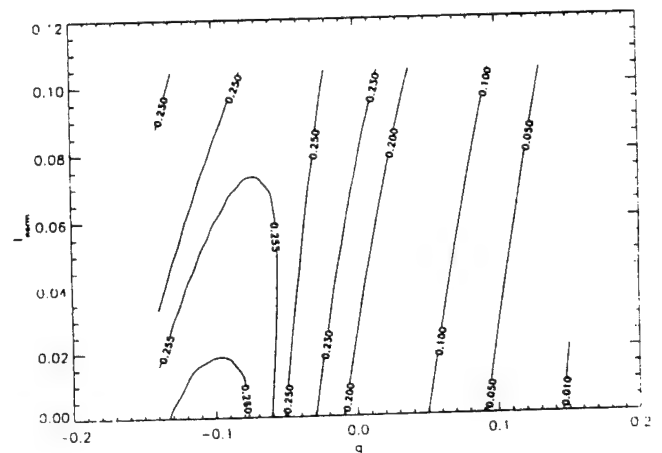


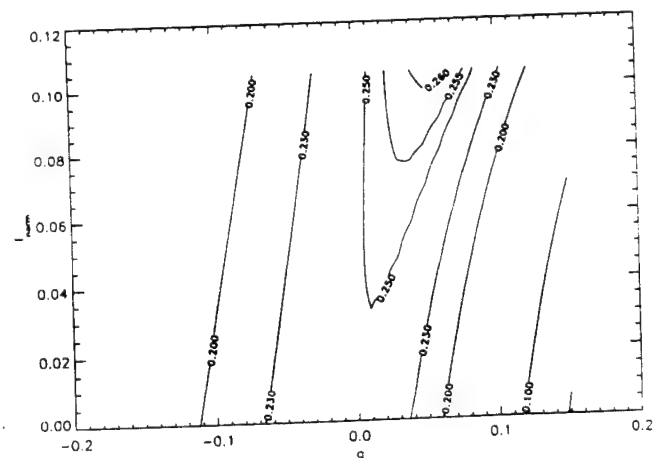
FIG. 3. Contours of equal efficiency for a resonant BWO in the plane of normalized amplitude of the microwave field and detuning of Čerenkov synchronism.

#### IV. NONLINEAR THEORY

Numerical simulations of the nonlinear set of equations (8) and (9) have been carried out for the specific value of electron initial energy,  $\gamma_0 = 2$ . The electron efficiency was first studied in the absence of the two new



(a)



(b)

FIG. 4. Lines of equal efficiency in the plane of normalized parameters  $q$  and  $I$  for the normalized length of a slow-wave structure  $L=20$ ,  $N=8$ .



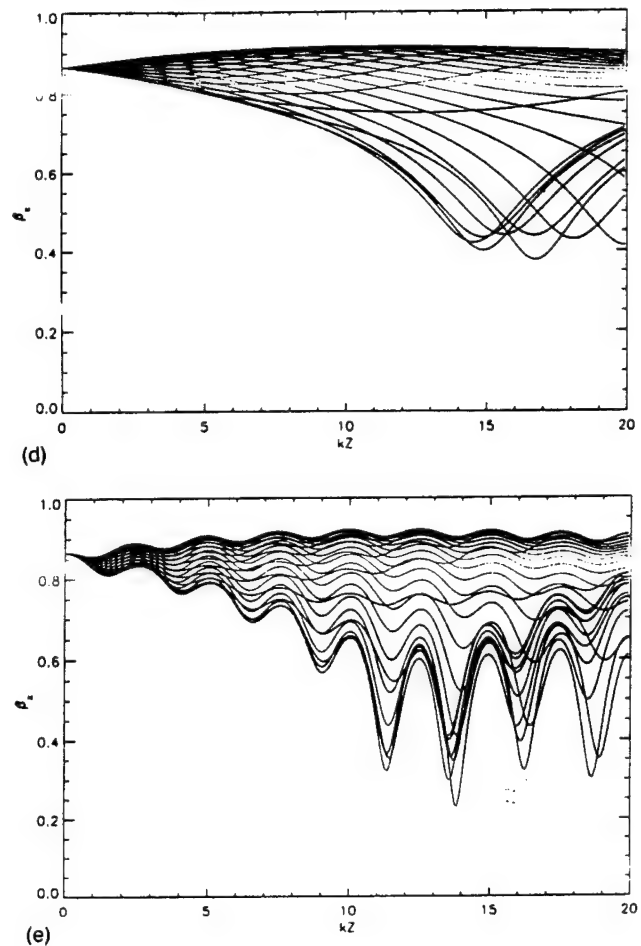
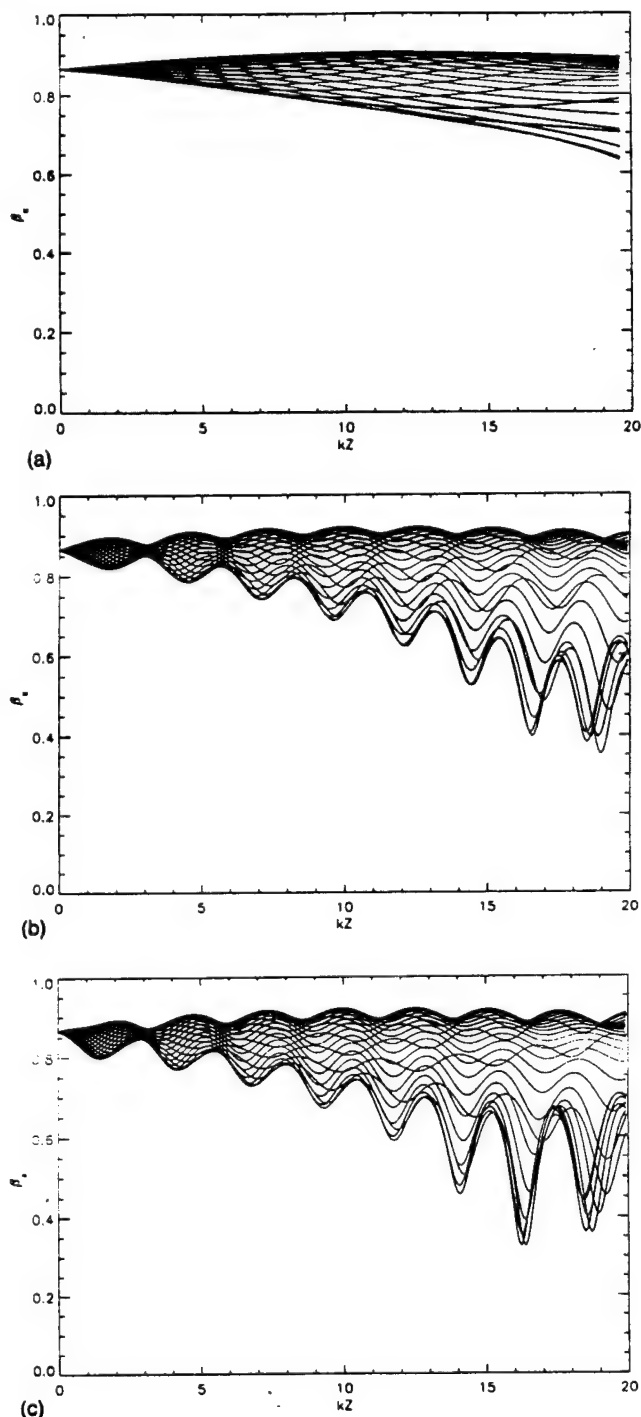


FIG. 5. Axial dependences of electron velocities with and without account for axial modulation of electron potential and interaction with zero spatial harmonics of the field. All figures correspond to  $L=20$ ,  $\delta=-0.25$ . Other parameters are (a)  $A=0.05$ ,  $I=q=0$ ; (b)  $A=0.05$ ,  $I=0$ ,  $q=-0.1$ ,  $N=8$ ; (c)  $A=0.05$ ,  $I=0.1$ ,  $q=-0.1$ ,  $N=8$ ; (d)  $A=0.07$ ,  $I=q=0$ ; (e)  $A=0.07$ ,  $I=0.15$ ,  $q=-0.03$ .

effects (at  $q=I=0$ ) as the function of the mismatch of synchronism,  $\delta$ , and the normalized field amplitude,  $A$ , at different values of the normalized length,  $L$ . It was found that when  $L$  varies from 15 to 25 the maximum efficiency is a rather weak function of  $L$ . The typical dependence of efficiency on  $\delta$  and  $A$  is shown in Fig. 3 for  $L=20$  as lines of equal efficiency in the plane of frequency detuning,  $\delta$ , and the normalized amplitude,  $A$ .

Then, the effect of new parameters,  $q$  and  $I$ , was studied. It was found that these parameters may give relatively weak enhancement in the efficiency of operation when the detuning,  $\delta$ , and amplitude,  $A$ , correspond to the maximum efficiency in the absence of the new effects. However, these effects may widen the region of parameters where efficient

operation may take place, especially at small amplitudes. Corresponding results are presented in Fig. 4, where  $A=0.05$  and  $L=20$ . In Fig. 4(a) the lines of equal efficiency are shown in the plane of parameters  $q$ ,  $I$  for  $\delta=-0.25$  and an 8-period structure (results of the study of a 6-period structure for the same values of  $A$ ,  $L$ , and  $\delta$  are very similar). In Fig. 4(b) the same lines are shown for  $\delta=-0.2$  and an 8-period structure. In both cases the maximum efficiency is above 26% which is close to the  $\eta_{\max} \approx 29\%$  shown in Fig. 3 for the system without these new effects.

To illustrate the effect of velocity modulation by interaction with the zero spatial harmonic of the wave and a rippled wall structure, it is expedient to present the axial

dependencies of electron velocities with and without these effects. Such dependencies are shown in Fig. 5. Figures 5(a)–5(c) correspond to the field amplitude  $A=0.05$ ; Figs. 5(d) and 5(e) to  $A=0.07$ . All other parameters are  $L=20$ ,  $\delta=-0.25$ ,  $N=8$ . Figures 5(a)–5(d) correspond to  $q=I=0$ ; Fig. 5(b) to  $I=0$ ,  $q=-0.1$ ; Fig. 5(c) to  $I=0.1$ ,  $q=-0.1$ ; and Fig. 5(e) to  $I=0.15$ ,  $q=-0.03$ . Comparing these figures, one can find that the interaction of electrons with the zero spatial harmonic and the axial modulation of the electron potential have a significant effect on the reduction of electron velocities. In particular, Fig. 5(e) shows that the operation at given parameters is close to the appearance of reflected particles that can also be stimulated by an initial electron velocity spread, which was not taken into account here.

## V. DISCUSSION

To illustrate the results of the theory developed in the normalized parameters above, let us express these parameters in real numbers corresponding to a typical experimental setup. Consider the 8-period slow-wave structure described in Ref. 9 and used in a number of experiments with relativistic BWO's at the Institute for Plasma Research, University of Maryland. This structure operated in the 8 GHz frequency range. The period of the structure is 1.67 cm, its average radius is 1.5 cm and the height of corrugation is 0.4 cm. Correspondingly, if we take the axial wave number for the zero spatial harmonic as equal to  $-\pi/2d$ , then for an electron beam with 500 kV operating voltage and 1 cm beam radius we get that the value of normalized current parameter 0.05 corresponds to  $\sim 0.5$  kA of the real electron beam current.

In the same manner one can find from Eq. (10) that parameters of the slow-wave structure and the electron beam given above correspond to the ratio of harmonic am-

plitudes  $E_{0,z}/E_{-1,z} \approx -10.6$ , which in turn corresponds to the value of the normalized parameter  $q = -0.236$ .

This example shows us that the results presented in the paper can be used for interpretation of a number of experiments.

Note in conclusion that the effects studied may lead, first, to achieving a highly efficient operation at low beam currents and, second, to a more smoother dependence of the BWO efficiency on the beam current than that predicted by the theory developed without these effects. Besides the efficiency increase, these effects may also cause significant reduction in efficiency at certain parameters. Also important are pulsations in electron axial velocities caused by these effects because such pulsations may lead to the appearance of reflected electrons in high efficiency operation regimes.

## ACKNOWLEDGMENTS

This work has been partially supported by the U.S. Army Research Laboratory and Air Force Office of Scientific Research.

<sup>1</sup>J. Benford and J. Swegle, *High Power Microwaves* (Artech House, Norwood, MA, 1992).

<sup>2</sup>J. Swegle, J. W. Poukey, and G. T. Leifste, *Phys. Fluids* **28**, 2882 (1985).

<sup>3</sup>J. M. Butler, C. B. Wharton, and S. Furukawa, *IEEE Trans. Plasma Sci.* **PS-18**, 4906 (1990).

<sup>4</sup>M. I. Petelin, *Radiophys. Quantum Electron.* **13**, 1229 (1970).

<sup>5</sup>Z. N. Krotova and Y. S. Chertkov, *Radiophys. Quantum Electron.* **17**, 318 (1974).

<sup>6</sup>N. F. Kovalev, *Relativistic High-Frequency Electronics*, edited by A. V. Gaponov-Grekhov (Institute of Applied Physics, Gorky, USSR, 1984), Vol. 4, p. 5.

<sup>7</sup>N. F. Kovalev, *Elektronnaya Tekhnika*, Ser. 1, *Elektronika SVCh* March(3), 102 (1978).

<sup>8</sup>A. Vlasov, G. Nusinovich, B. Levush, A. Bromborsky, W. Lou, and Y. Carmel, *Phys. Fluids B* **5**, 1625 (1993).

<sup>9</sup>Y. Carmel, K. Minami, R. A. Kehs, W. W. Destler, V. L. Granatstein, D. Abe, and W. L. Lou, *Phys. Rev. Lett.* **62**, 2389 (1989).

Presented at the IEEE Conference on  
Plasma Science, June 5-8, 1995  
in Madison, Wisconsin.

# **Characterization of the Plasma Column Used in Studies of a Plasma-Loaded Relativistic Backward Wave Oscillator**

J. Weaver, S. Kobayashi, A. Shkuvarunets,\*  
Y. Carmel, J. Rodgers, W.W. Destler  
and V. L. Granatstein

University of Maryland, College Park, MD

\* General Physics Institute, Russian Academy of Science,  
Moscow, Russia

# **Abstract**

A series of experiments were made to characterize the electron component of a transient plasma column immersed in a magnetic field. These long plasma columns (radius=1 cm and length=100 cm) were used to fill the slow wave structure of a relativistic backward wave oscillator (BWO). The addition of plasma increased the efficiency of microwave generation, the operating frequency, and the maximum allowable beam current. The plasma was generated by a coaxial hydrogen flashover gun located just outside the solenoid on the center axis. The plasma electron radial density profile and the peak density were studied for various magnetic fields (2-15 kG), gun positions (24 & 32 cm from the solenoid end), and gun voltages (10-14 kV). This knowledge will allow more precise control of the operating conditions of plasma-loaded BWOs.

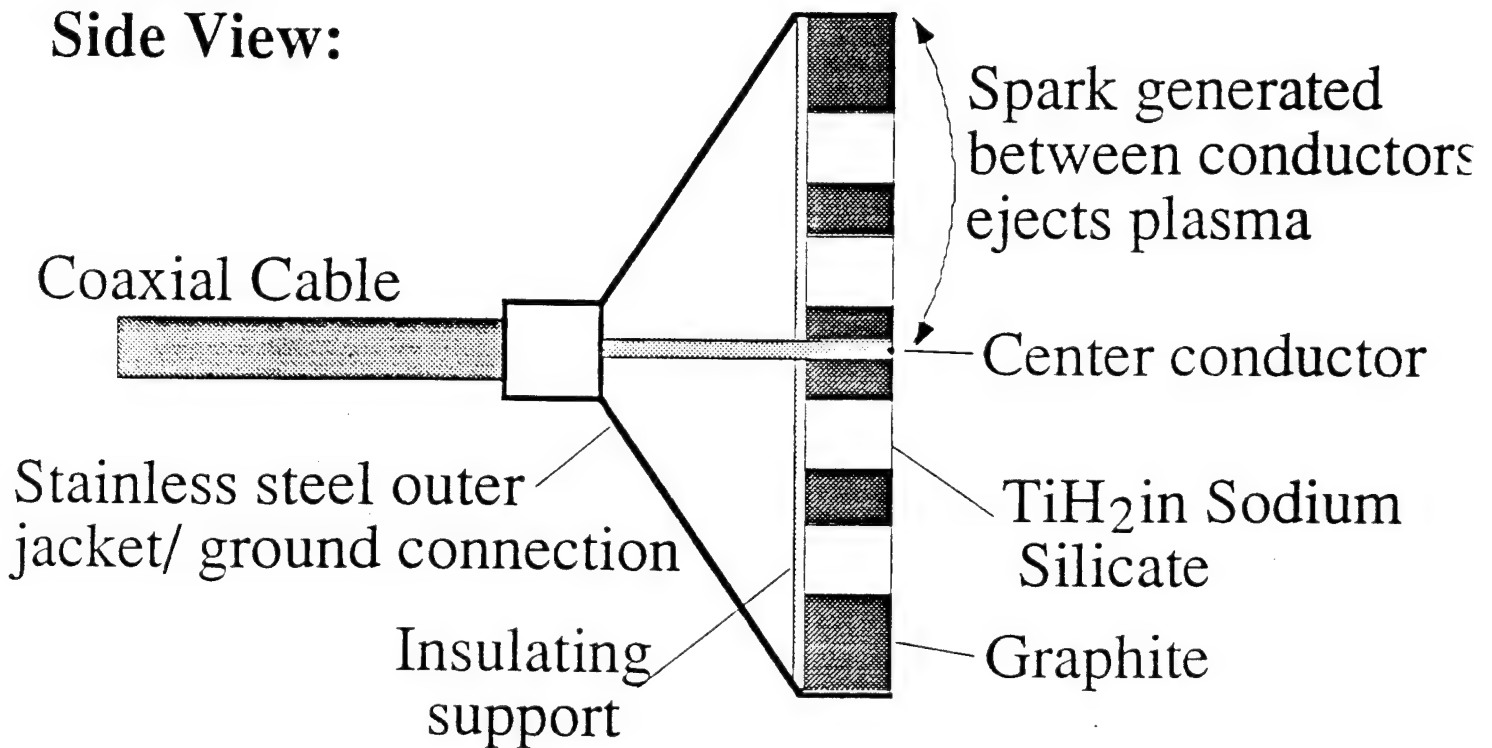
# **Introduction**

A single movable Langmuir probe and a cylindrical resonant cavity were used. The Langmuir probe consisted of a long thin tungsten wire oriented perpendicular to the plasma column and the applied magnetic field. The probe operated in two regimes: a constant bias to measure the electron saturation current and a pulsed bias to measure the current-voltage characteristic of the probe for any given moment. The peak plasma density and radial density profiles were deduced from a large number of such measurements. The results were compared to data gathered by an electromagnetic technique based on a plasma-loaded resonant cavity.

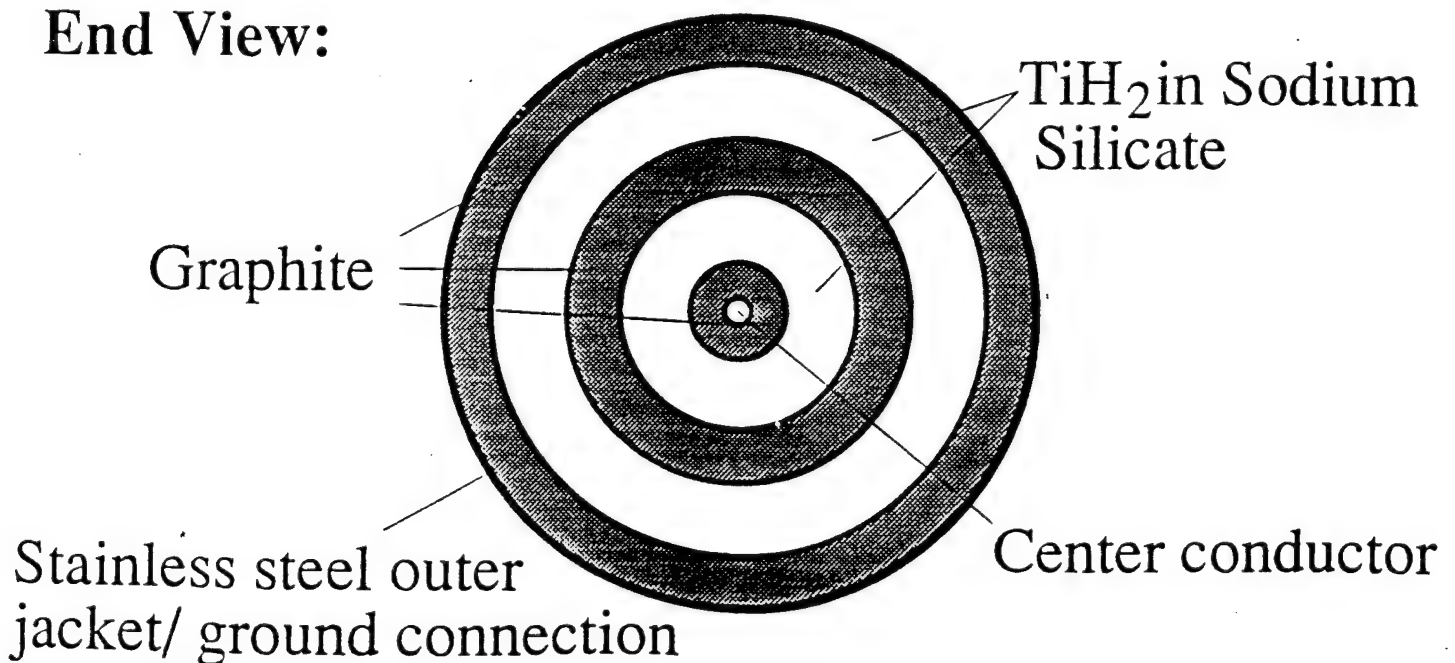
# Plasma Source

Plasma is formed when a high voltage pulse is applied between the center and outer conductor of gun. Ionized gas is ejected from titanium hydride impregnated rings concentric with the center conductor.

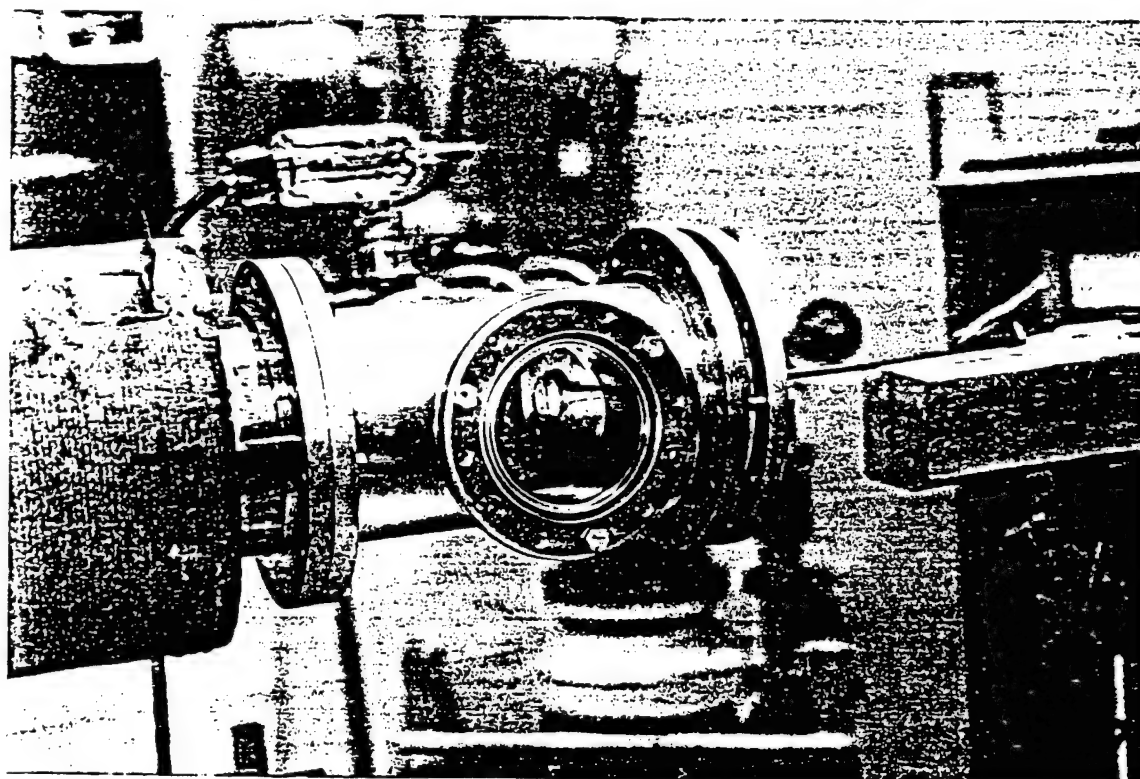
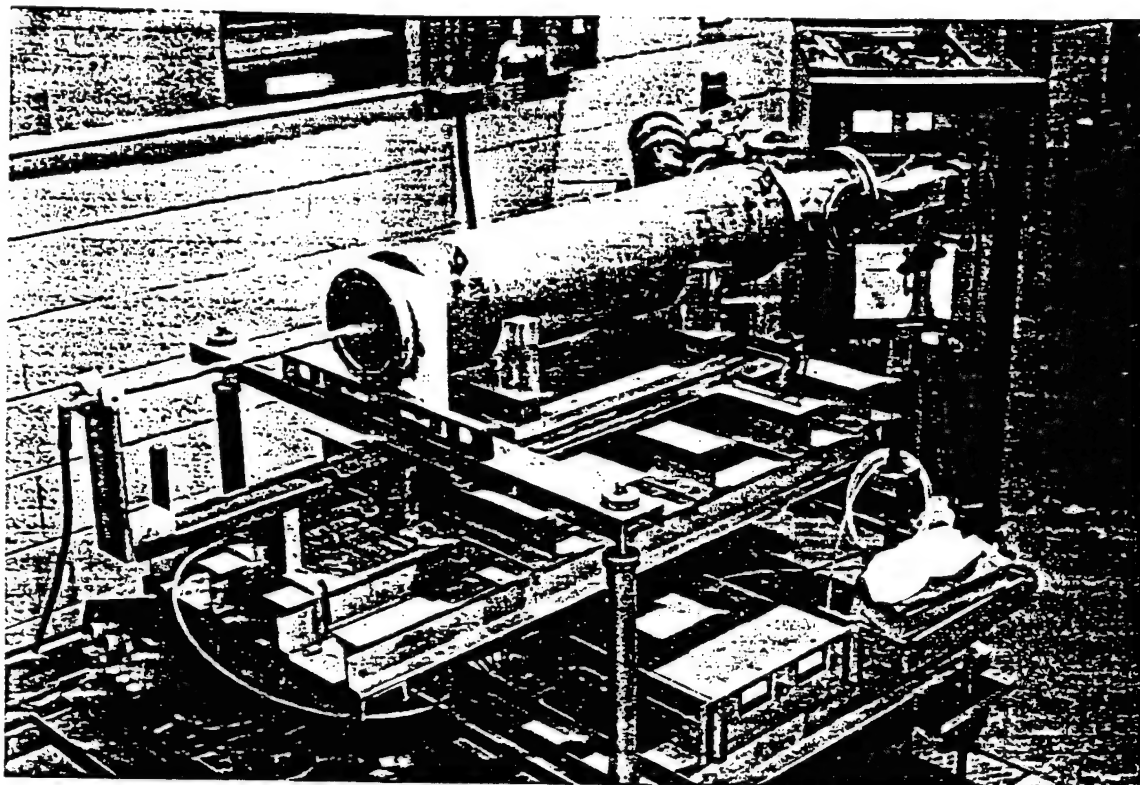
**Side View:**



**End View:**







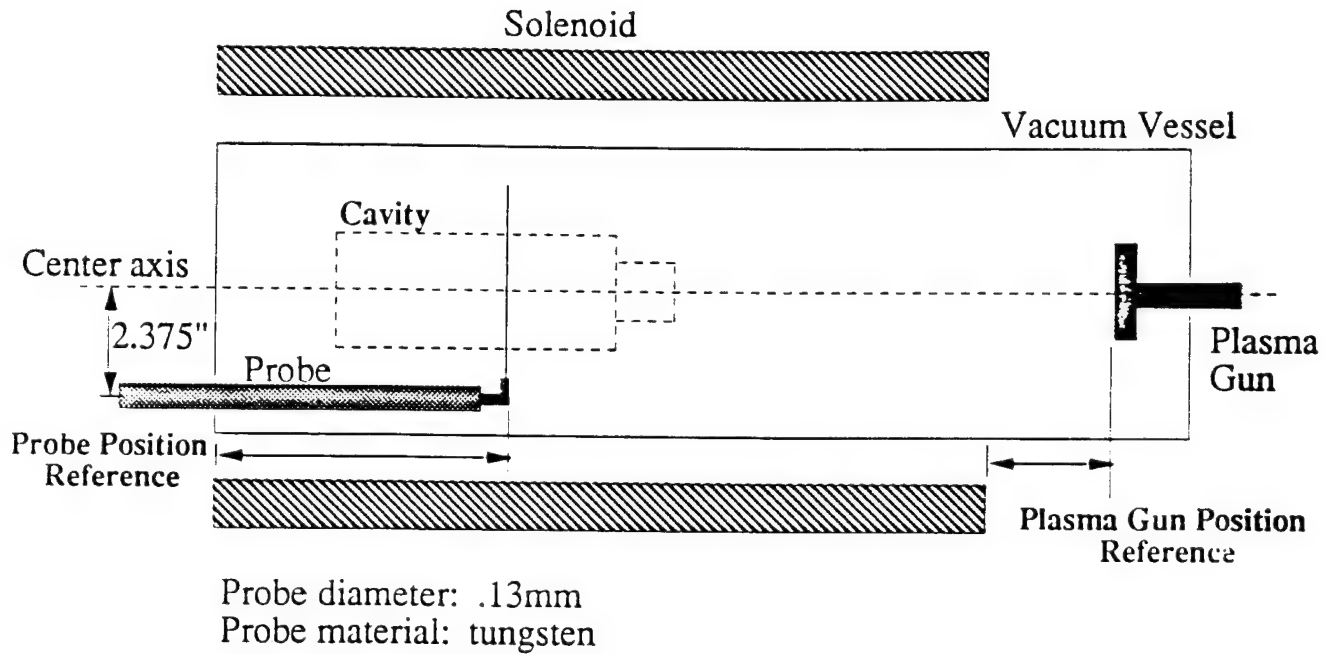
A system for mapping the plasma density inside the RF interaction region of a plasma loaded relativistic BWO.

# Langmuir Probe

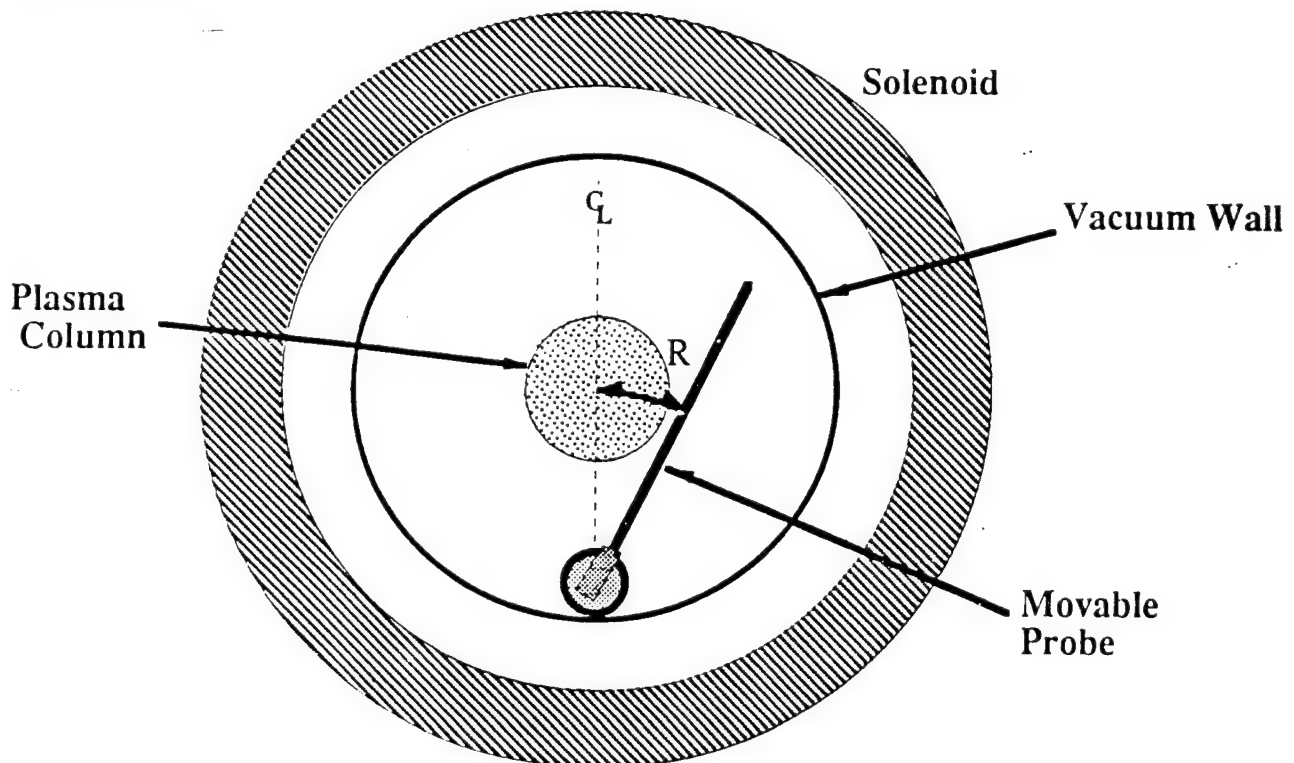
- Probe was operated in pulsed mode to measure temperature and in constant bias mode to measure electron saturation current.
- The probe consisted of a long thin tungsten wire. The current collected by the probe therefore represented the total current along a chord passing through the plasma. Measurements at many angles for a given axial position allowed estimation of the plasma radius for a given set of parameters.

# Schematic Diagram of Probe Arrangement:

Side View:

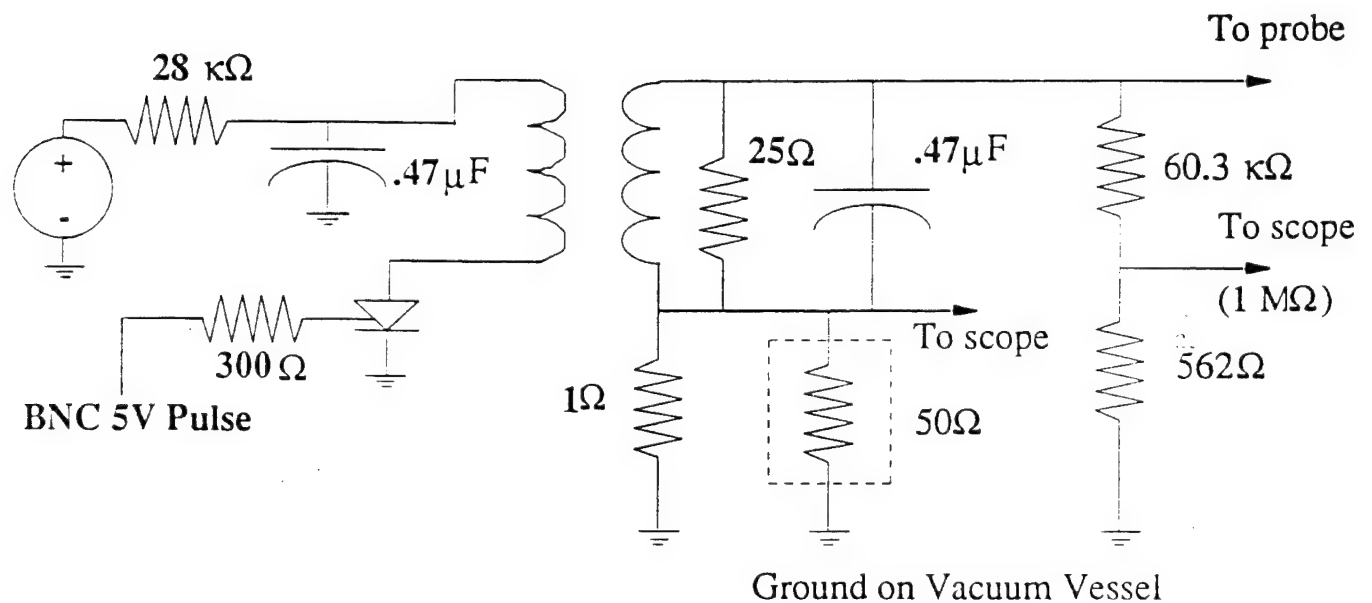


End View:

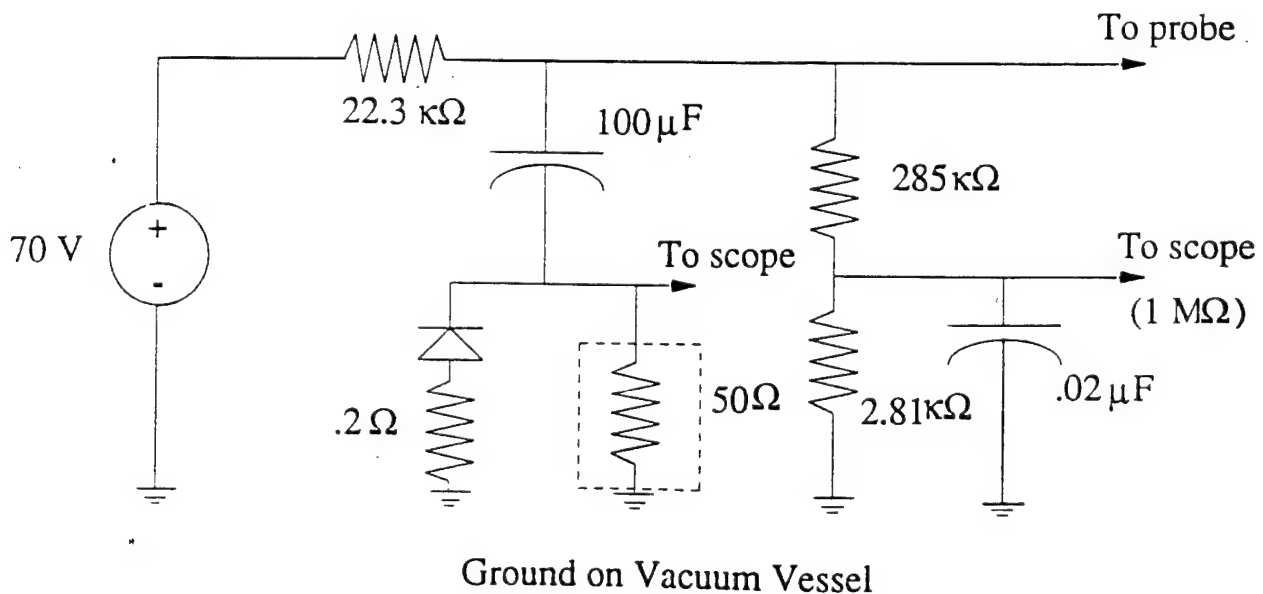


# Probe Bias Circuits for Plasma Measurement:

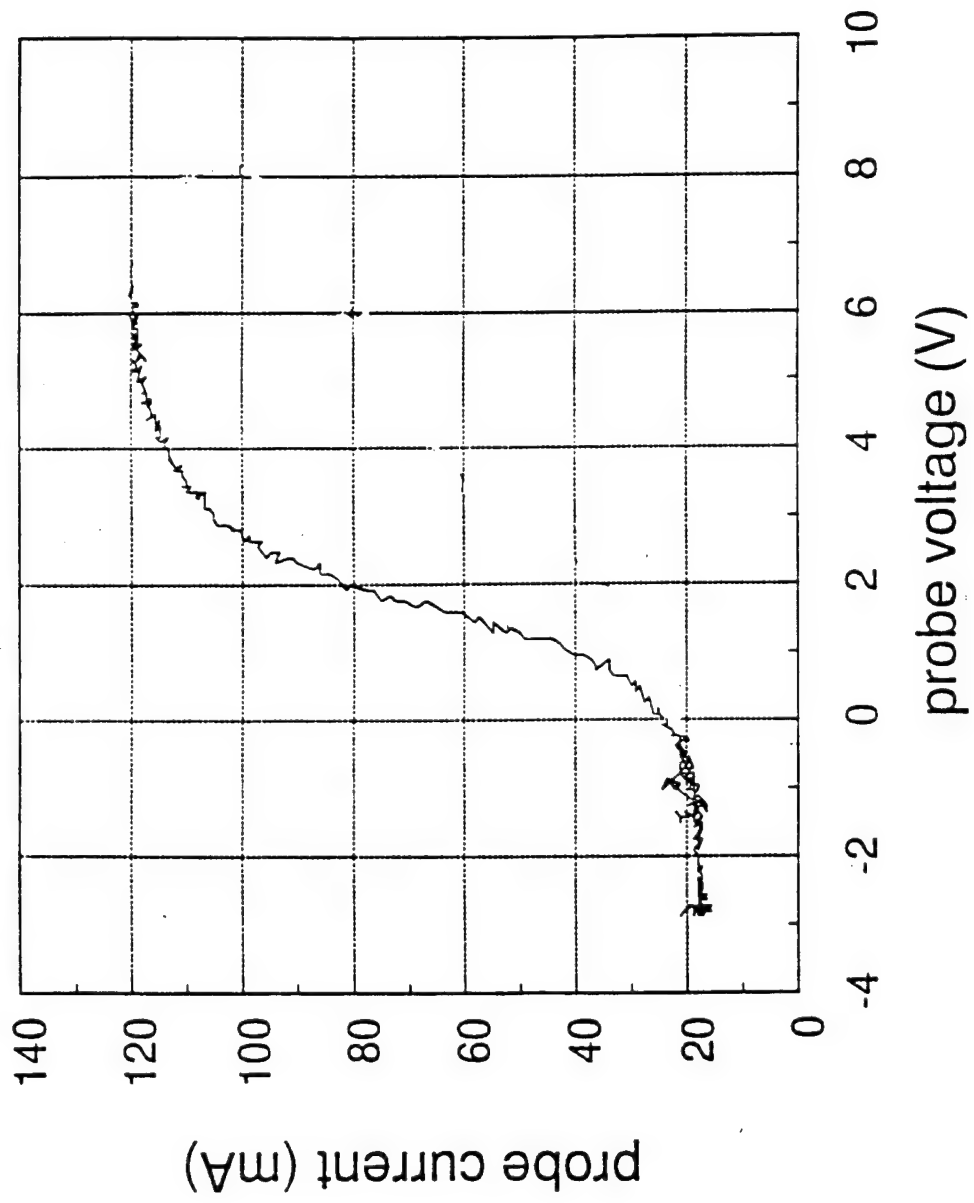
## Pulse Bias Circuit:



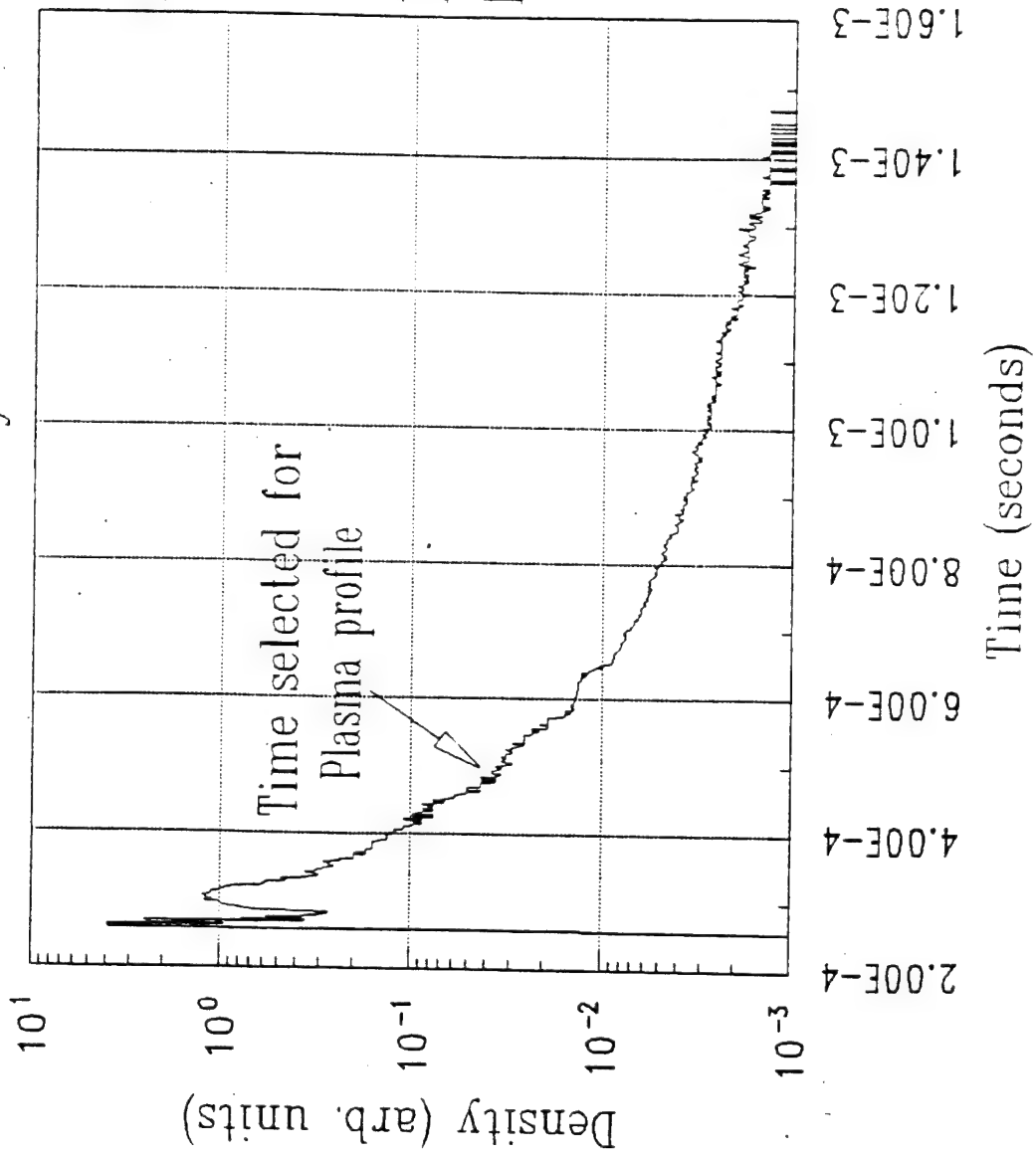
## D. C. Bias Circuit:



I-V characteristic of the probe



# Electron Density vs Time



Position  $R=0$  mm

B field = 14 kG

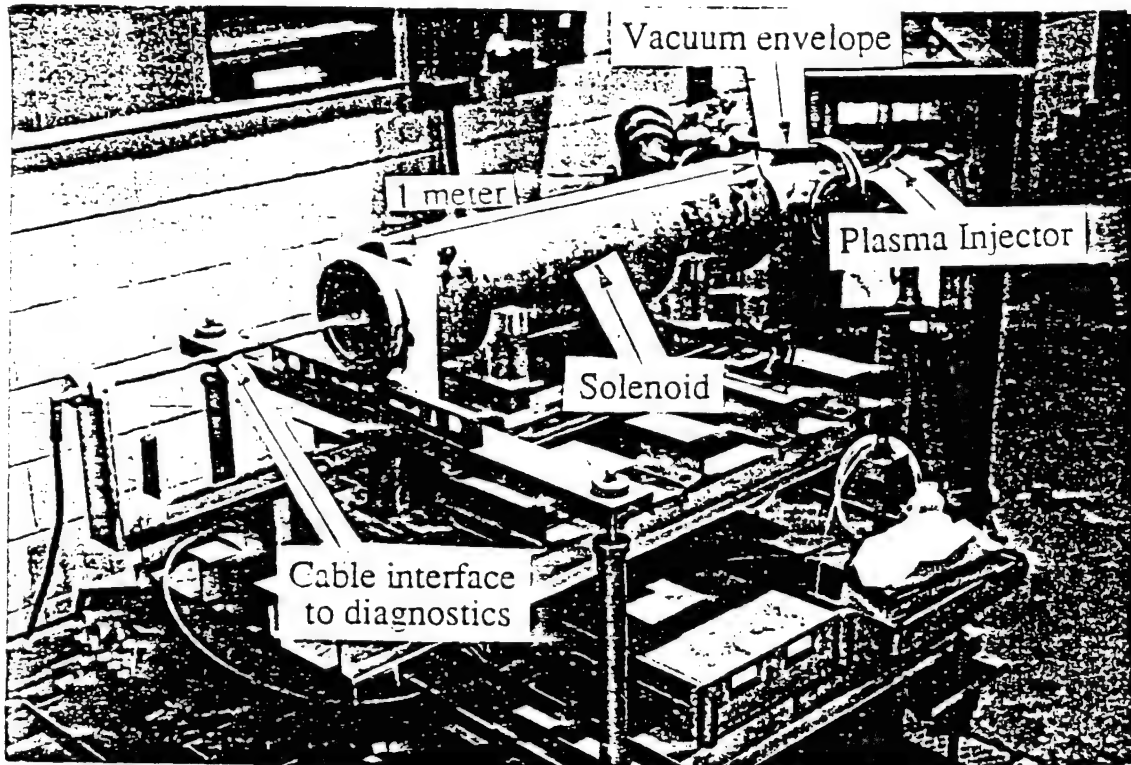
Probe distance  
from plasma gun:  
40 cm



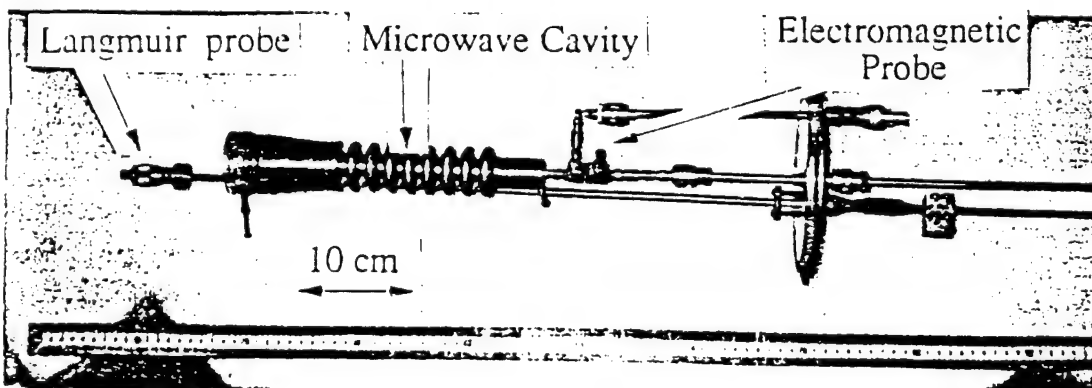


University of Maryland at College Park  
Institute for Plasma Research

## Measuring the Plasma Density Within the Microwave Generator



Overview

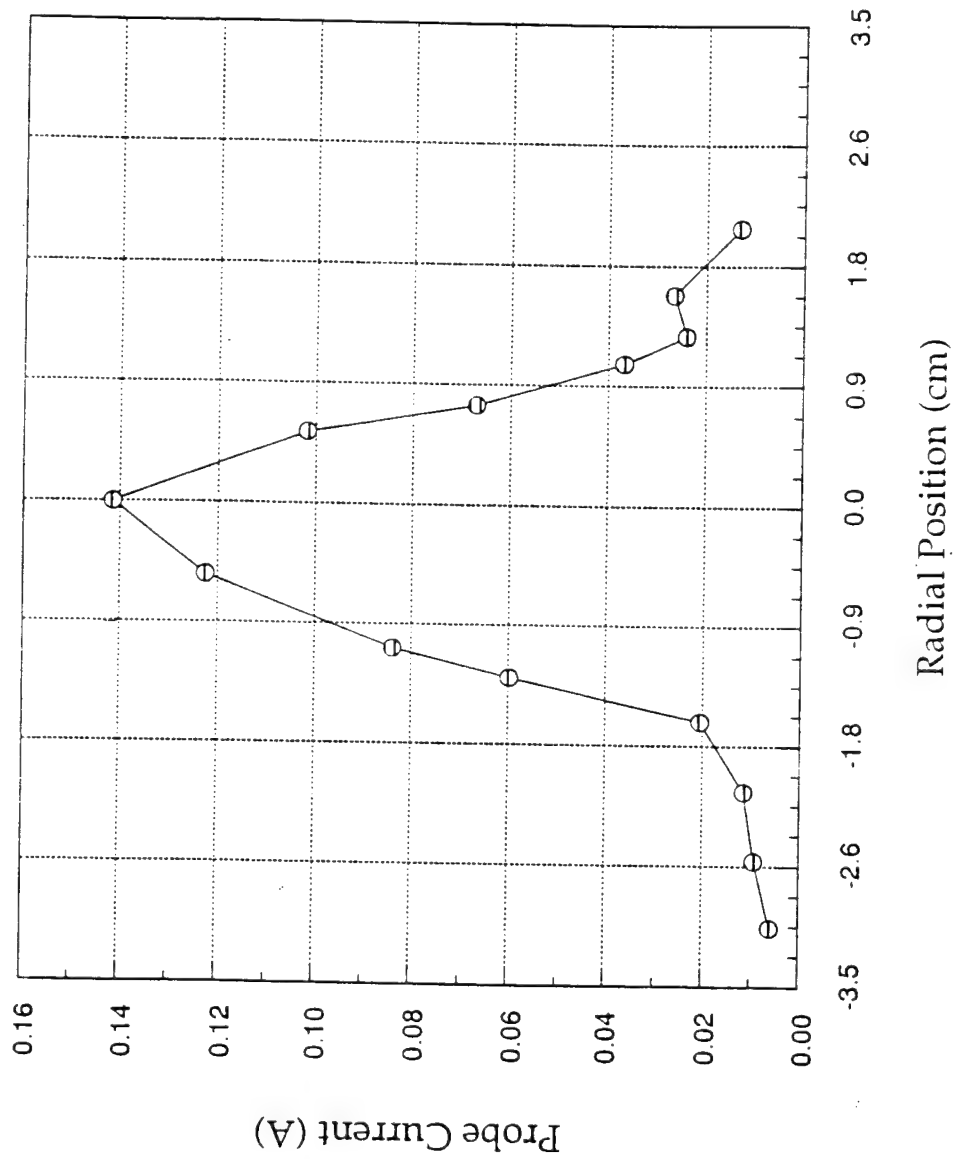


Components of  
the Diagnostics  
(inside the  
vacuum  
envelope)

## **Radial Plasma Density Profile**

The radial plasma density profile has been used to estimate the radius of the plasma column. The sample plot on the left illustrates the data. Analysis requires some important assumptions. The key point is that the probe actually measures the density along a chord through the column. The true radial distribution can be deconvolved from the current measurements under the assumption of axisymmetry. For the purposes of this experiment, an estimation of the plasma column radius was of main importance so only this parameter is presented. It has been estimated from the FWHM of data sets such as the one on the left.

# Radial Profile of Probe Current



Probe Position: 25 cm Gun Voltage: 12 kV

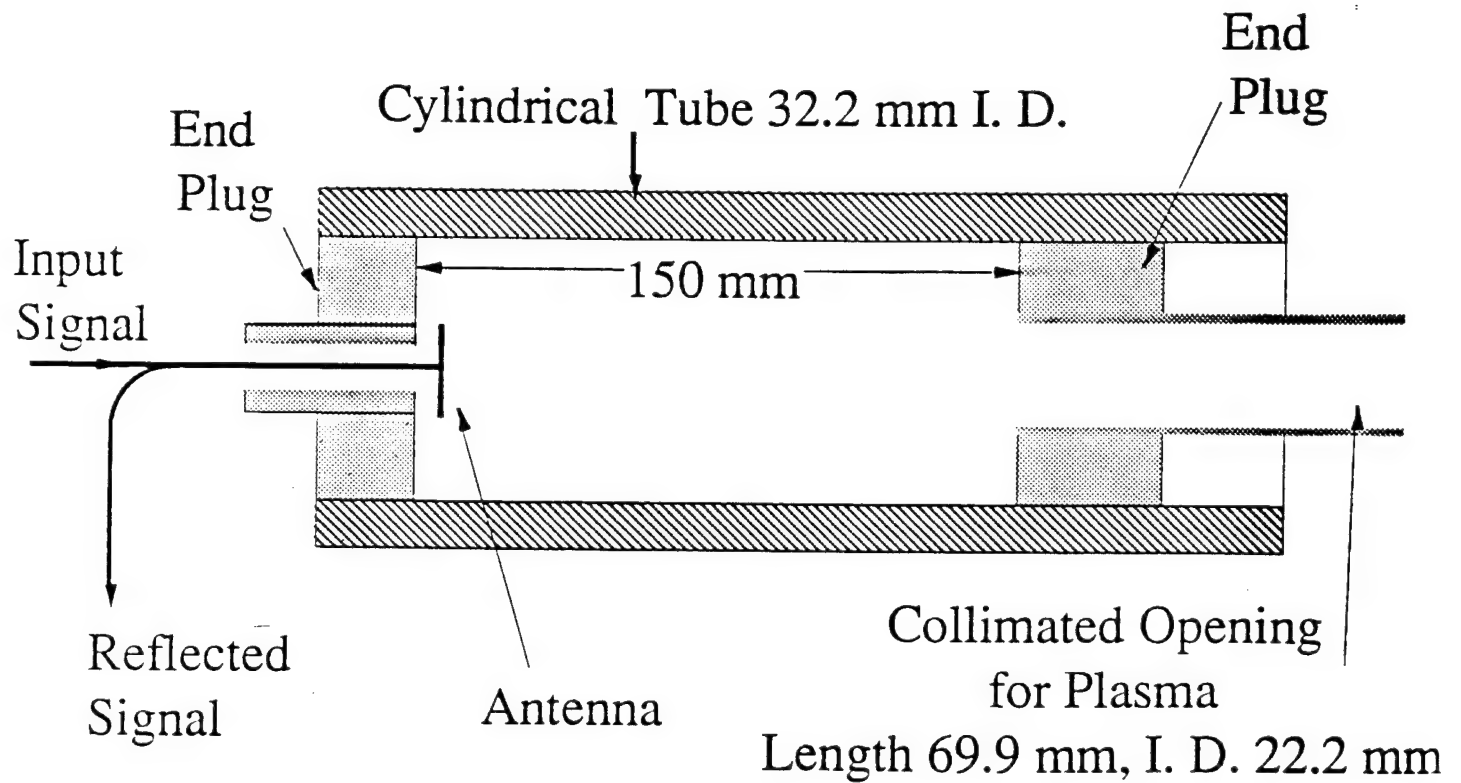
Gun Position: 32 cm Magnetic Field: 6.0 kG

## **Resonant Cavity**

Plasma density may also be measured by determining the amount of shift in the resonant frequency of a simple cavity due to the introduction of plasma into the volume of the cavity. The value obtained from such a method is used to calibrate the Langmuir probe measurement since the latter can measure relative density changes more accurately than the absolute value.

In these experiments, the rapidly changing plasma density caused the resonant conditions in the cavity to change in time. If a fixed frequency was injected into the cavity, various resonances could be seen via a one-port reflection measurement. The plasma density could be calculated by comparing the applied frequency and mode numbers observed to the predictions from a numerical model for the system. The details of this method were presented in session 1D03, by S. Kobayshi.

## Schematic Diagram of Resonant Cavity

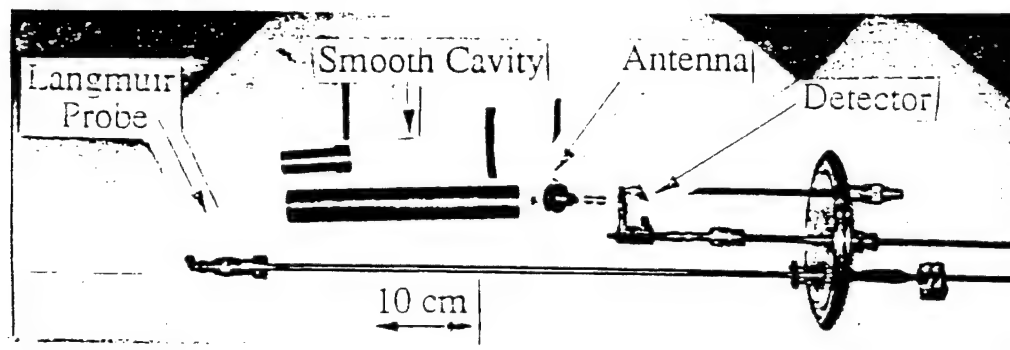




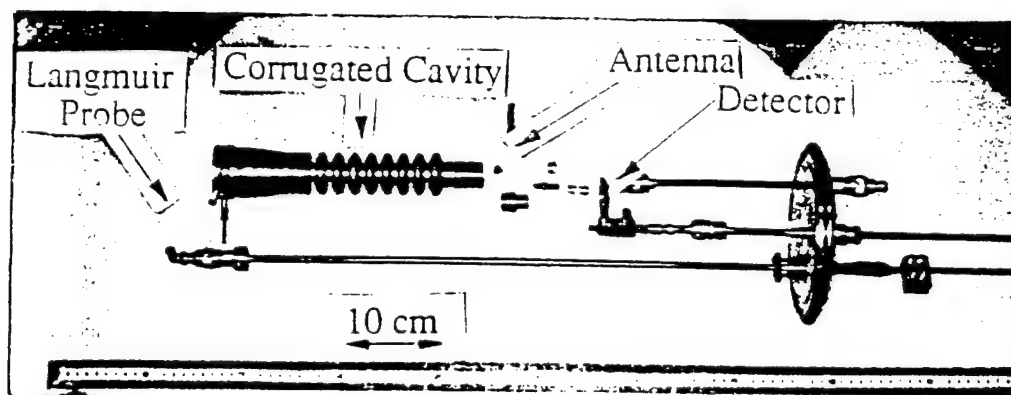
University of Maryland at College Park  
Institute for Plasma Research

## Measuring the Electromagnetic Characteristics of Plasma Loaded Cavities

Smooth-Walled Cavity

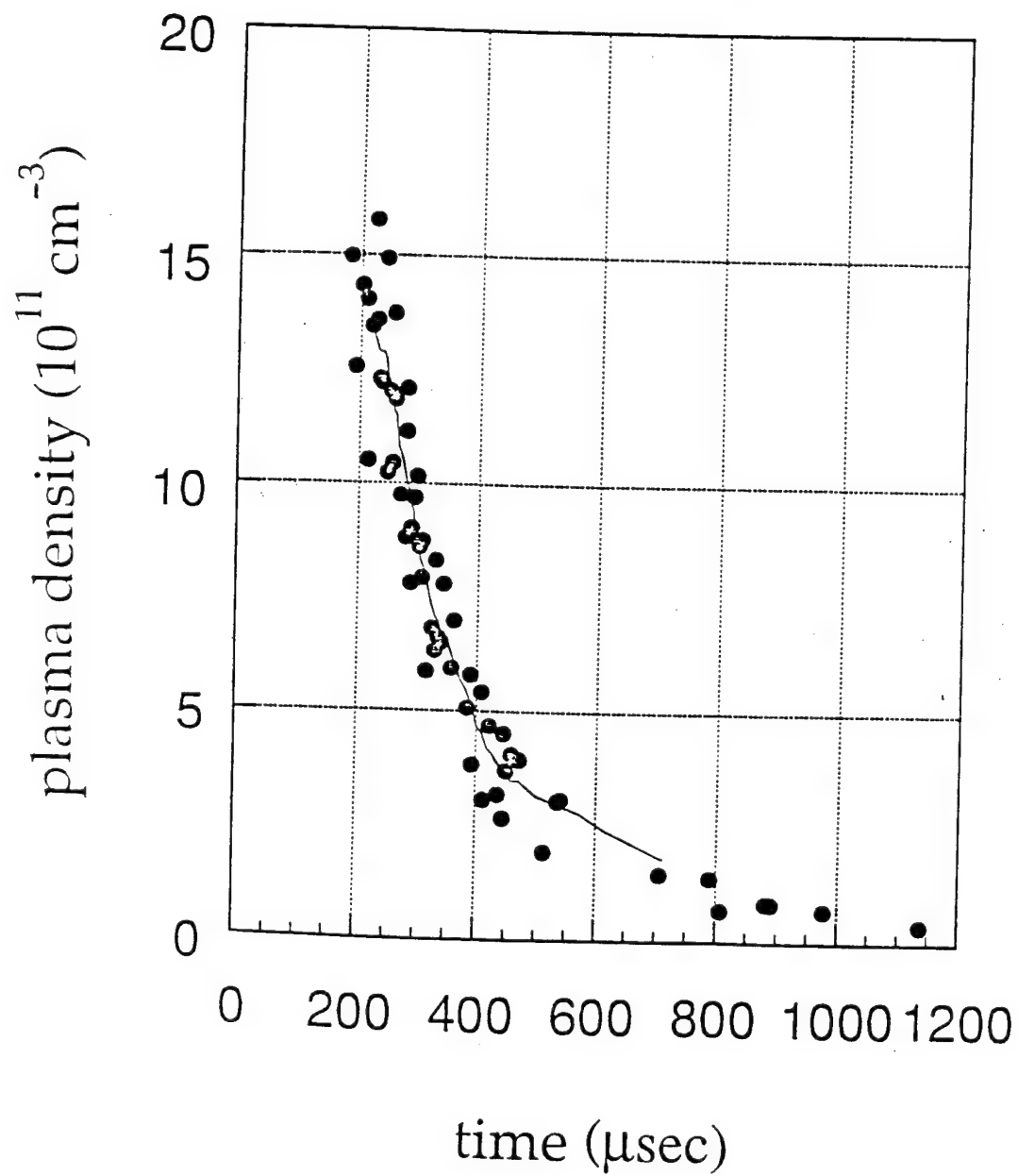


Corrugated Cavity

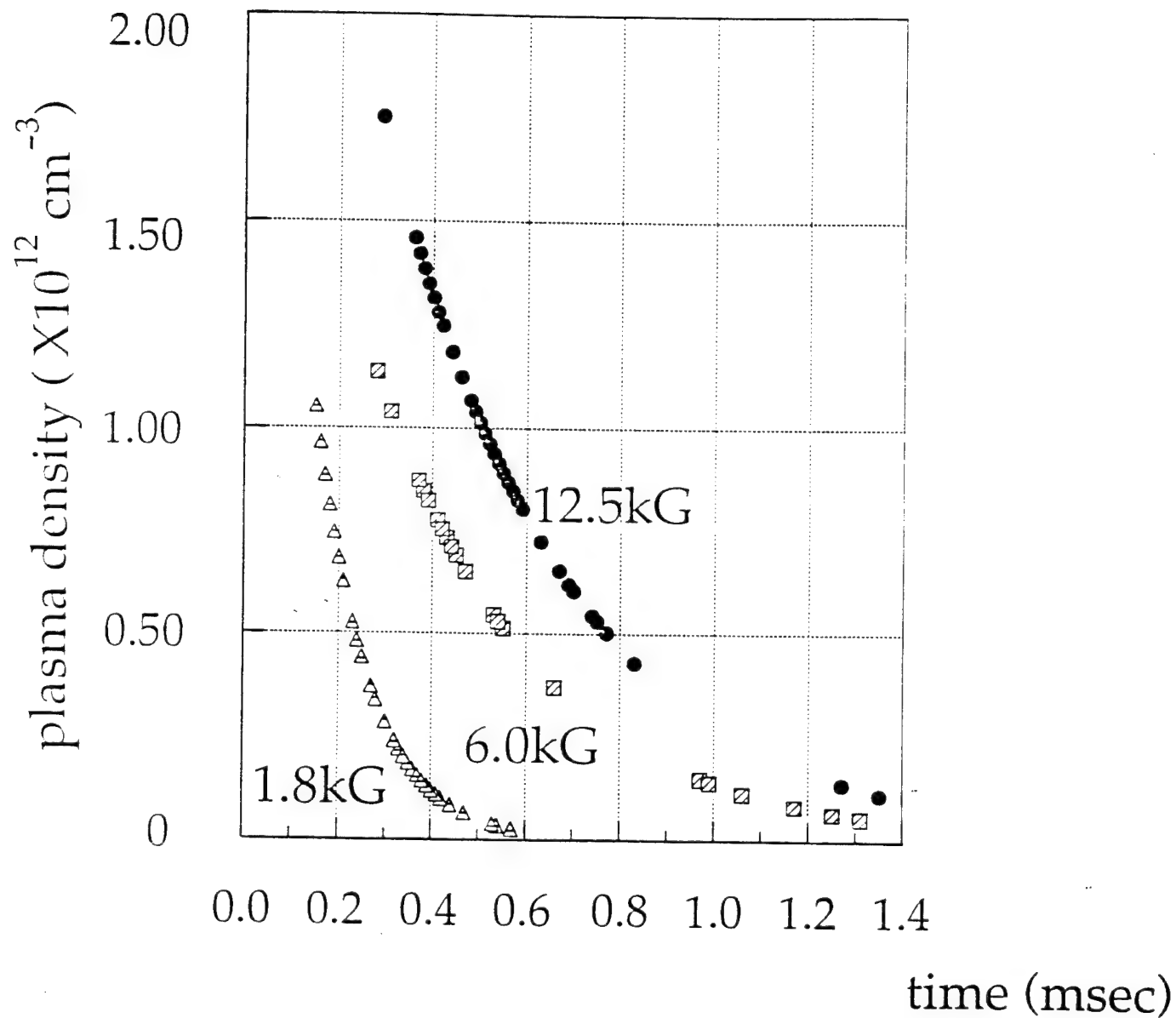




Plasma density v.s. time



# plasma density v.s. time

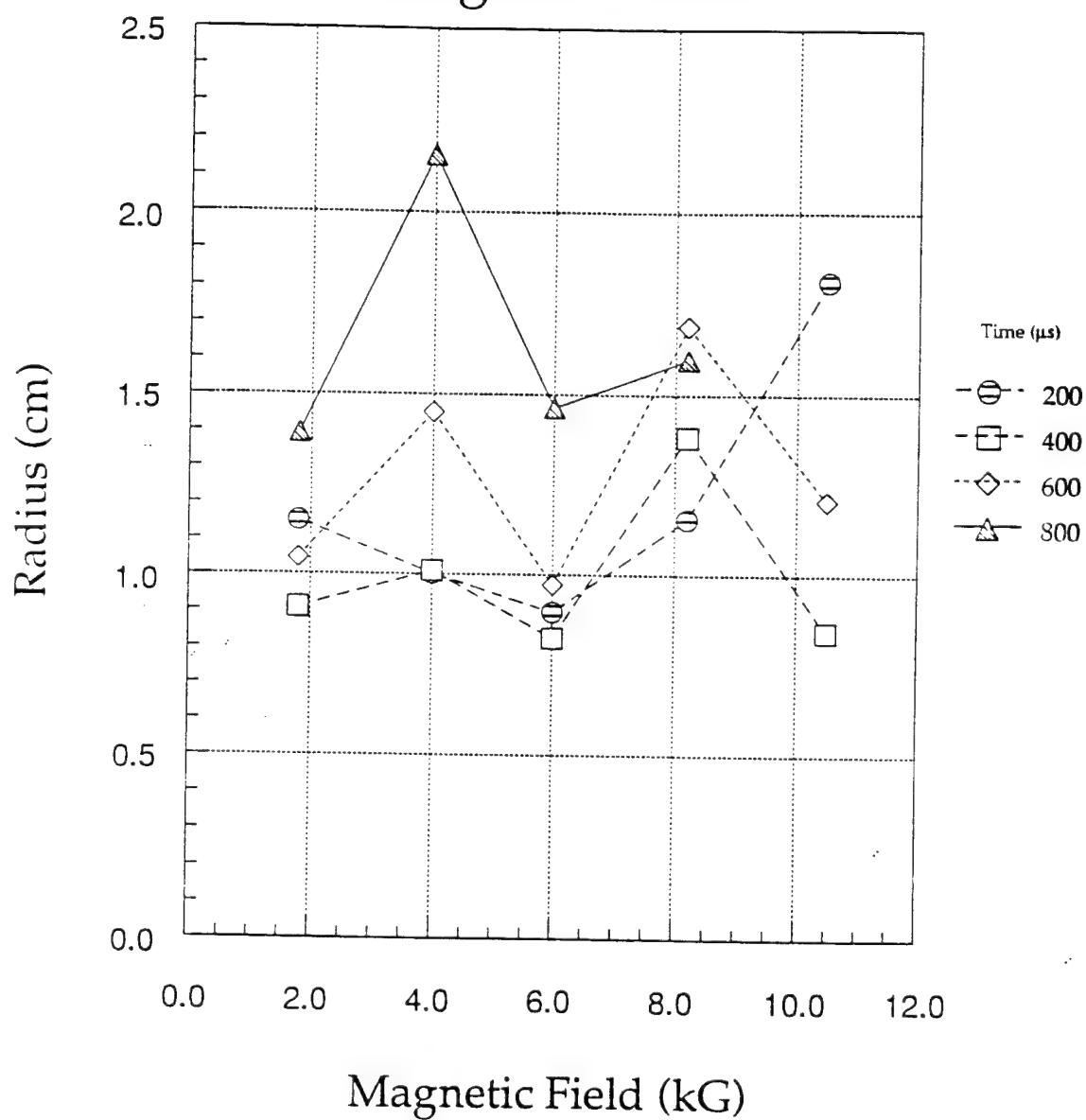


gun position 32 cm

gun voltage 12 kV

position 29 cm

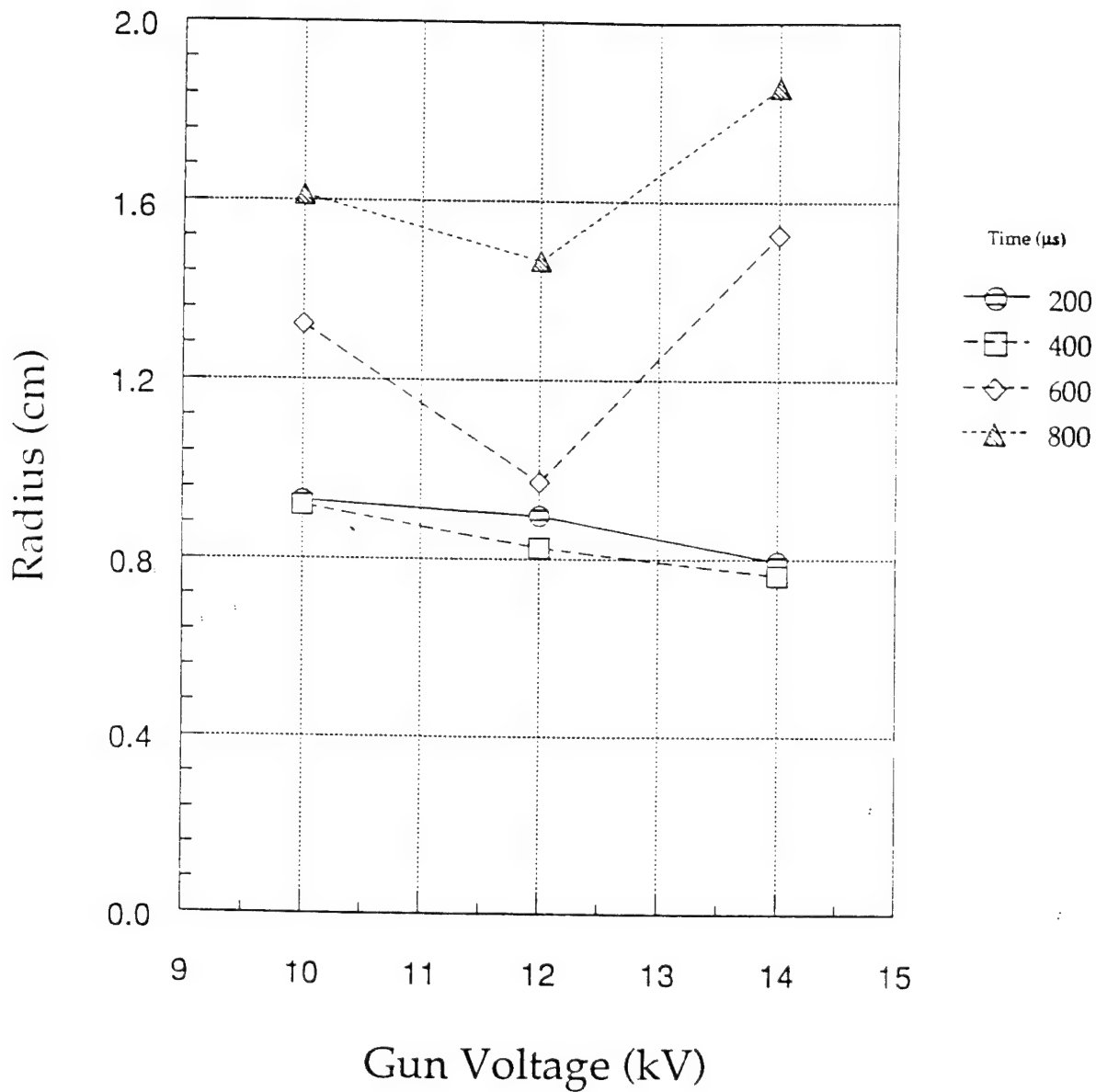
# Plasma Radius Vs. Applied Magnetic Field



Probe Position: 25 cm    Gun Position: 32 cm

Gun Voltage: 12 kV

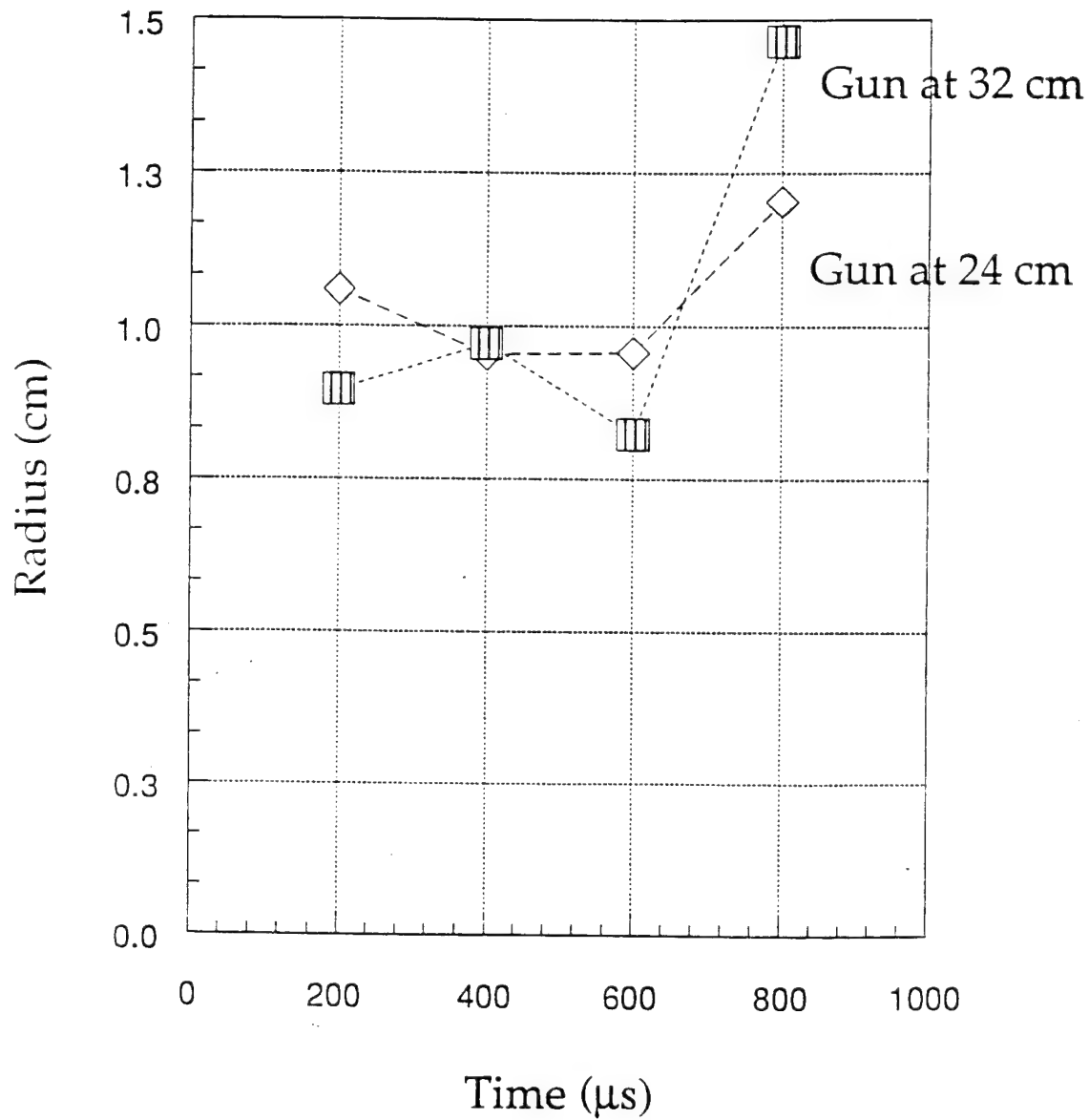
# Plasma Radius Vs. Applied Gun Voltage



Probe Position: 25 cm   Gun Position: 32 cm

Magnetic Field: 6.0 kG

## Plasma Radius Vs. Gun Position



Probe Position: 32 cm Magnetic Field: 6.0 kG

Gun Voltage: 12 kV

# Conclusions

- Langmuir probe was used to find the peak plasma density and the radial profile of the plasma column.
- Cavity technique provided an independent calibration of the plasma density.
- The following characteristics of the plasma column were established:
  - Peak plasma density decays from  $10^{12-3}$  to  $10^9$  cm<sup>-3</sup> on a time scale of roughly 1 ms.
  - An increase in the peak plasma density was observed with an increase in the applied magnetic field.
  - The plasma diameter was approximately 2 cm.
  - The plasma temperature was roughly 1 eV.
- Future experiments with the plasma-loaded backward wave oscillator can now select a particular plasma density through timing control of the plasma gun.



# Starting Energy and Current for a Large Diameter Finite Length Backward Wave Oscillator Operated at the Fundamental Mode

K. Minami, K. Ogura, Y. Aiba, M. R. Amin, X. D. Zheng, T. Watanabe, Y. Carmel, *Senior Member, IEEE*,  
W. W. Destler, *Fellow, IEEE*, and V. L. Granatstein, *Fellow, IEEE*

**Abstract**—We study the starting conditions for a large diameter (diameter/wavelength = 4.8) finite length backward wave oscillator designed for 24-GHz operation at the fundamental  $TM_{01}$  mode. This geometry is very promising for high power handling capability. We analyze two separate threshold conditions. First, finite length effects give rise to a threshold in electron beam energy below which oscillations cannot be sustained at any beam current. The second is the more familiar current threshold known as a start current. It is also found that the growth rate for the fundamental mode can be much larger than those of other higher order modes thus leading to coherent operation of large diameter sources free from mode competition.

## I. INTRODUCTION

HIGH-POWER MICROWAVE sources are important for a number of advanced applications ranging from current drive and RF heating of magnetically confined plasmas in fusion devices to high resolution nanosecond radars [1]–[3]. Pulsed high power microwave oscillators utilizing intense relativistic electron beams have been extensively studied in recent years [2]–[6]. Among various microwave sources, the multiwave Cerenkov generators (MWCG's) developed by [7] at the High Current Electronics Institute, Tomsk, Russia, have recently attained record outputs [7], [8]. Radiation powers of 7.5 GW at a wavelength  $\lambda = 9.7$  mm with an electronic efficiency of 20% were reported. The MWCG involves a slow wave structure (SWS) with an average diameter  $D$  much larger than  $\lambda$ . In the above example,  $D/\lambda = 13$ . This large diameter SWS enables a larger output power for a given RF energy density inside the SWS before breakdown occurs. Despite a possibility of mode competitions, efficient, high power single mode oscillation was attained in a device utilizing overmoded SWS [9]. Twenty years ago, high average power millimeter microwave sources (gyrotrons) were invented by combining an electron cyclotron maser and an overmoded open barrel cavity [2], [3]. The large diameter (overmoded) SWS in MWCG's may be an innovative key technology which corresponds to the overmoded open cavity employed

in gyrotrons, although the final evaluation of performance and the feasibility of using MWCG's in actual applications are yet to be established. The MWCG has a close relationship to conventional backward wave oscillators (BWO's), since both employ SWS's in common [4], [5], [7]–[14].

Although the physical processes involved in the MWCG's [7], [8] are complicated, we point out here that high-power millimeter microwaves can be generated without decreasing the mean diameter of the SWS. Both BWO's and large diameter BWO's can be operated in the fundamental  $TM_{01}$  mode as will be shown in this paper. The difference in SWS's between the two devices is as follows. The inner radius of the metal surface of the SWS,  $R(z)$ , is assumed to vary sinusoidally around the mean radius  $R_0$ , i.e.,  $R(z) = R_0 + h \cos K_0 z$ ,  $K_0 = 2\pi/z_0$ . Here,  $z_0$  and  $h$  are, respectively, the axial length of periodicity and the amplitude of corrugation. In BWO's [4], [5], [10]–[14], the mean radii,  $R_0 = D/2$ , were chosen such that  $D/\lambda = 2R_0/\lambda \sim 1$ , whereas, in the present large diameter BWO, the condition  $D/\lambda \gg 1$  is explored. The key point is that, in the latter, oscillation frequency is raised by carefully choosing small values of  $h$  and  $z_0$ , keeping  $R_0$  larger than  $\lambda$ . This situation is quite similar to the SWS design of MWCG's [7]–[9]. In the present paper, numerical studies are made within the scope of linear analysis for a large diameter SWS with  $D/\lambda \sim 4.8$ . Specifically, the starting energy and the starting current of the beams for initiating microwave oscillation in such a finite length SWS are analyzed in detail. Previously, the starting current conditions for finite length BWO's have been studied by various authors [5], [13], [15], [16]. Swegle analyzed the starting condition for a BWO [15]. In his treatment, 100% reflection at the beam entrance boundary and 0% reflection at the RF output boundary were assumed. This assumption was valid for the case of matched termination at the output end of the SWS. We consider here an alternative case of nonzero round trip reflection which may correspond to the experimental situations in [4] and [10]. Such nonzero round trip reflection produces discrete spectra of axial wavenumber of eigenmodes of an axisymmetric TM mode [13], [14], [17].

In Section II, we describe the model of our linear analysis. The difficulties to be overcome in the practical numerical computation in the case of  $D/\lambda \gg 1$  are discussed. Numerical results are shown in Section III. Discussion and conclusions are given in Section IV.

Manuscript received April 8, 1994; revised December 19, 1994.

K. Minami, K. Ogura, Y. Aiba, M. R. Amin, and X. D. Zheng are with the Graduate School of Science and Technology, Niigata University, Niigata City, 950-21, Japan.

T. Watanabe is with National Institute for Fusion Science, Nagoya 464-01, Japan.

Y. Carmel, W. W. Destler, and V. L. Granatstein are with the Institute for Plasma Research, University of Maryland, College Park, MD 20742 USA.

IEEE Log Number 9409799.

## II. FORMULATION AND DIFFICULTIES IN NUMERICAL ANALYSIS

The model of an axisymmetric large diameter SWS with length  $L$  shown in Fig. 1 is analyzed. The radius  $R(z)$  of perfectly conducting metal wall varies with  $R(z) = R_0 + h \cos K_0 z$ . The entire system is immersed in a strong longitudinal external magnetic field. The transverse motion of the beam electrons is assumed to be negligible. We also assume that an infinitely thin annular beam with radius  $R_b$ , monoenergetic beam energy  $V_b$  and current  $I_b$  is incident to the SWS. The linear dispersion relation for the system in Fig. 1 was derived previously [15], [18], [19] and the results are summarized here. The boundary condition that the tangential components of the RF electric field at the corrugated metal surface of the SWS must be zero gives

$$\sum_{m, n=-\infty}^{\infty} [1 + (n-m)Q_n] (B_n C_{mn}^J + C_n C_{mn}^N) = D_{mn} \cdot A_n = 0 \quad (1)$$

$$C_{mn}^J = \int_{-\pi/K_0}^{\pi/K_0} \exp[i(n-m)K_0 z] \cdot J_0[y_n(1 + \alpha \cos K_0 z)] dz \quad (2)$$

$$= \sum_{q=0}^{\infty} \frac{(y_n \alpha)^{(2q+|n-m|)} J_0^{(2q+|n-m|)}(y_n)}{2^{2q+|n-m|} q! (q+|n-m|)!}, \quad \alpha = h/R_0 \quad (3)$$

where  $Q_n = K_0 k_n / (\omega^2/c^2 - k_n^2)$ ,  $k_n = k + nK_0$ ,  $y_n^2 = R_0^2(\omega^2/c^2 - k_n^2)$  and  $c$  is the vacuum velocity of light. The RF field amplitudes,  $A_n$ ,  $B_n$ , and  $C_n$  of the Floquet harmonics are the same as those in (7) in [18]. The beam quantities such as  $I_b$  and  $V_b$  are involved in  $B_n$  and  $C_n$ . In (1),  $C_{mn}^N$  is obtained by replacing the Bessel function of the first kind,  $J_0$ , in  $C_{mn}^J$  by that of the second kind,  $N_0$ . In the above expressions, temporal and spatial phase factors  $\exp[i(k_n z - \omega t)]$  have been assumed for every RF quantity. The dispersion relation combining  $\omega$  and  $k$  is given from (1) as the determinant equation,

$$D(k, \omega) = \det [D_{mn}] = 0 \quad (4)$$

which is required to have nontrivial  $A_n$  in (1). As is well known,  $N_0$  goes to infinity at the origin which occurs in the case of light line in vacuum,  $\omega = ck_n$ . Because the roots of (4) are slow waves, they are located in the complex  $\omega$  and  $k$  planes considerably separated from where  $\omega = ck_n$ . Difficulty of  $N_0$  infinity does not occur for finding the roots.

We discuss here some peculiar difficulties that arise in the computation for the large diameter SWS. For the time being, we consider the simple case without the beam, i.e.,  $I_b = 0$ , and  $A_n = B_n$ ,  $C_n = 0$  in (1) accordingly [18]. Because no input energy is present in the SWS, oscillations cannot be expected. For a real  $\omega$ , real  $k$ 's are obtained in (4) and vice versa. Equations (2) and (3) were useful to compute the dispersion relation of a BWO [19], [20]. In the present case of large diameter BWO's, however, there exist

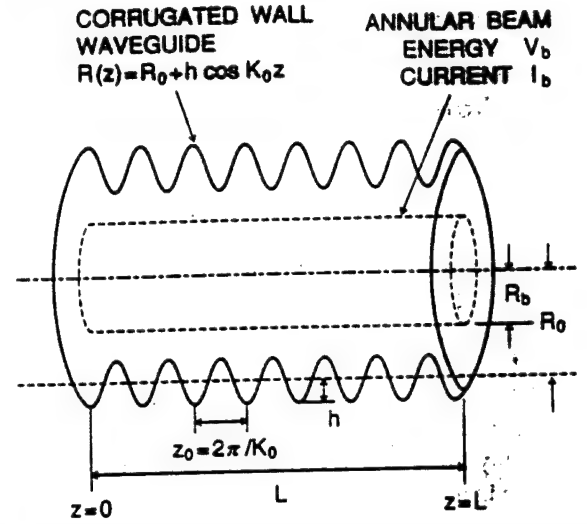


Fig. 1. Model of analysis. Annular beam of monochromatic energy  $V_b$  and current  $I_b$  is incident on the axisymmetric corrugated wall large diameter slow wave structure with length  $L$ .

some difficulties for computing (2) and (3). In order to get a large oscillation frequency  $\omega/2\pi$  without decreasing  $R_0$  we must choose a small  $h$  and  $z_0$  in Fig. 1 that results in a large  $K_0$  and that makes  $y_n^2 < 0$  in (2). For negative  $y_n^2$ , the Bessel function  $J_0$  becomes modified Bessel function  $I_0$  consequently, and the integrand of (2) is rewritten as  $\exp[i(n-m)K_0 z] I_0[y_n'(1 + \alpha \cos K_0 z)]$ , where  $y_n'^2 = -y_n^2$ . The modified Bessel function  $I_0$  in the integrand becomes extremely large, if  $y_n'$  is large. This effect causes an overflow in the process of numerical computation of (4). Such a difficulty arises often in the calculation of the large diameter SWS with small  $z_0$ . To avoid the difficulty, we express  $I_\nu(z)$  as

$$I_\nu = \frac{e^z}{(2\pi z)^{1/2}} \left( 1 - \frac{\mu-1}{8z} + \frac{(\mu-1)(\mu-9)}{2!(8z)^2} - \dots \right) \quad |\arg(z)| < \frac{\pi}{2}, \quad \mu = 4\nu^2.$$

Using this asymptotic expansion, (1) is expressed as

$$\sum_{m, n=-\infty}^{\infty} [1 + (n-m)Q_n] \frac{C_{mn}^J}{\exp(y_n')} G_n = D'_{mn} \cdot G_n \quad G_n = A_n \exp(y_n'), \quad D'(k, \omega) = \det [D'_{mn}] = 0. \quad (5)$$

The dispersion relation is given by (5) instead of (4). Equation (5) does not have problems with numerical overflow.

The next problem concerns the adequacy of the Taylor expansion used in (3). In general, numerical integration of (2) takes much computation time and the expanded form of (3) is preferable, as long as the sinusoidally corrugated SWS in Fig. 1 is considered. A large  $K_0$  again may result in  $|y_n \alpha| >$  in (3), and the summation does not converge rapidly. We find that tens of terms in (3) must be calculated to get a converge value of summation because of increased denominators. To avoid this difficulty, we truncate the rank of the determinant in (5) to as small a value as possible. This is because the value of  $k_n$  and accordingly  $y_n$  will not be very large for sma

rank of truncated determinant. For example,  $|y_n \alpha| \gg 1$  may be avoided, if one limits  $-1 \leq n, m \leq 0$  ( $2 \times 2$  determinant) or  $-1 \leq n, m \leq 1$  ( $3 \times 3$  determinant). Fig. 2 shows the result of the design study; the oscillation frequency  $f = \omega/2\pi$  versus the corrugation wavenumber  $K_0$  for several corrugation amplitudes  $h$ . Here,  $R_0 = 3.0$  cm has been assumed as a given parameter. Curves in the figure are obtained by computing the frequencies at the crossing point of the structure mode and the beam space charge line with  $I_b = 0$  for various values of  $K_0$  and  $h$ . The straight line,  $\omega = V_b K_0/2$ , in Fig. 2 is the boundary that divides the BWO (absolute instability) from the TWT (convective instability) for the case of  $\pi$ -mode operation ( $k = K_0/2$ ) with  $V_b = 100$  keV. Microwave oscillation can be expected in the cases of  $K_0$  to the left of the straight boundary line. Roughly speaking, BWO's and large diameter BWO's are expected, respectively, in cases of  $K_0 < 10$  cm $^{-1}$  and  $K_0 > 10$  cm $^{-1}$ . The black circle represents the parameters we have chosen for the present design study of a large diameter BWO with the following parameters:  $K_0 = 18.5$  cm $^{-1}$  ( $z_0 = 0.34$  cm),  $h = 0.17$  cm and  $f = 24$  GHz. The solid and dashed curves are, respectively, the calculations using (3) and (5) of the  $9 \times 9$  and  $2 \times 2$  approximate truncated determinants. The differences between both curves are less than 4%. For the chosen size parameters, the dispersion curves are calculated for various truncated ranks from 9 ( $9 \times 9$ ) to 2 ( $2 \times 2$ ) of the determinant in (5). For ranks larger than 6, the oscillation frequencies are almost unchanged, and the results are considered to be exact. Even in the case of rank 2, the deviations from exact values are less than several percent. These facts suggest that the truncation to the rank 2 of the determinant in (5) is almost correct for our purpose. Hence, in order to save computation time, we adopt the truncated determinant of rank 2 in the subsequent numerical analysis of complex  $\omega$  and  $k$  with incident beams, at the sacrifice of accuracy within a few percent.

### III. NUMERICAL RESULTS

#### A. Infinitely Long Slow Wave Structure

The parameters of the large diameter SWS used in the following numerical analysis are:  $R_0 = 3.0$ ,  $h = 0.17$ ,  $z_0 = 0.34$ , and  $R_b = 2.63$  cm. Beam energies of  $V_b = 100$  and 65 keV are used as typical values. The beam current  $I_b$  is mostly assumed to be 0.4 kA, unless specified otherwise.

The dispersion relation (5) for complex  $\omega/2\pi$  versus real wavenumber  $k$  is shown in Fig. 3 for two values of  $V_b$ , 100 and 65 keV represented, respectively, by solid and dashed curves. Real and imaginary parts of  $\omega/2\pi$  are shown, respectively, in (a) and (b). Here, the beam current of  $I_b = 0.4$  kA has been assumed. Because of Floquet's theorem, the dispersion curves have periodicity  $K_0$  for wavenumber  $k$ , in other words,  $\omega(k) = \omega(k + nK_0)$ . Usually, figures are shown for the first Brillouin zone  $-K_0/2 \leq k \leq K_0/2$ , however, we depict hereafter the curves for  $0 \leq k \leq K_0$ , because the important parts of the curves are located near  $k = K_0/2$ . As were pointed out previously, there exist generally 4 independent roots for the fundamental  $TM_{01}$  mode [18], [20]. They are the fast

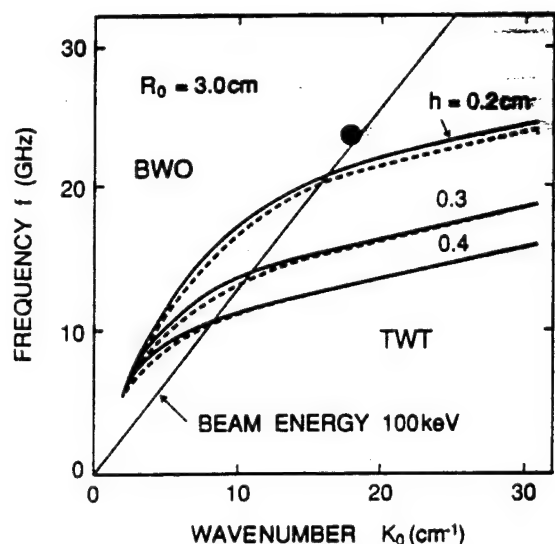


Fig. 2. Design study of the slow wave structure. Oscillation frequency for 100 keV beam versus corrugation wavenumber  $K_0$  for various corrugation amplitudes  $h$ . The mean radius is  $R_0 = 3.0$  cm. The solid and dashed curves are, respectively,  $9 \times 9$  and  $2 \times 2$  approximate results of the determinant of the dispersion relation. The black circle is the chosen parameters of our large diameter backward wave oscillator.

and slow space charge waves and the backward and forward structure waves. The first wave is always heavily damped and it is ignored entirely in the subsequent analysis. The second wave is the energy source for the third wave, i.e., the output radiation. The fourth wave can serve as a positive feedback mechanism in the case of a finite length SWS. For simplicity, the fourth wave is also ignored hereafter. For a real  $k$ , (5) can have a pair of complex conjugate roots of  $\omega$ . They are a growing slow space charge wave and a decaying fast space charge wave. The single beam line for infinitesimal currents is split into the fast (shown by F) and slow (shown by S) beam space charge waves in Fig. 3(a), because of nonzero beam current. Absolute instability can be found around the crossing point of the backward structure wave (shown by B) and the line S. It is noted in Fig. 3 that the ranges of  $k$  for instability, i.e., complex  $\omega$  shown by thick solid and dashed lines in Fig. 3(b), are much more limited than the previous case of BWO's [18], [19]. This is because the corrugation parameter  $\alpha = h/R_0$  is presently smaller than those in the conventional BWO's. In other words, the oscillation condition in large diameter BWO's with  $D/\lambda \gg 1$  is more restrictive or stringent than those in BWO's with  $D/\lambda \sim 1$ .

In our large diameter (overmoded) SWS, there exists a possibility of mode competition between various candidates including the fundamental and higher modes. Steady oscillation of the fundamental mode may not be realized because the beam energy may be fed to various modes with higher frequencies. In order to clarify the situation, we extended the analysis for the fundamental mode shown in Fig. 3 up to sixth higher modes. The oscillation frequency and the maximum temporal growth rate of the fundamental  $TM_{01}$  mode are compared with those of higher modes. We computed the dispersion curves similar to Fig. 3 for each higher mode. Fig. 4 shows the dispersion curves for an infinitesimal beam current,

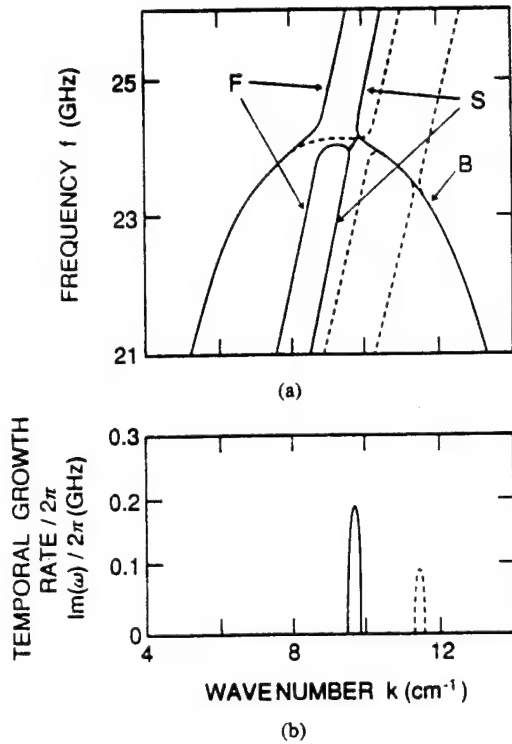


Fig. 3. Dispersion relation for complex  $\omega/2\pi$  versus real wavenumber  $k$ .  $I_b = 0.4$  kA. Solid curves are for  $V_b = 100$  keV and dashed curves are for  $V_b = 65$  keV. (a)  $f = \text{Re}(\omega)/2\pi$  versus  $k$ . (b)  $\text{Im}(\omega)/2\pi$  versus  $k$ .

from which the oscillation frequencies can be estimated. It is interesting to note that the dashed beam lines, 100 and 65 keV, intersect the curve of the fundamental  $\text{TM}_{01}$  mode at the positions where the group velocities are much smaller than those for higher modes. The results from complex analysis like Fig. 3 are summarized in Table I, where the maximum temporal growth rate, corresponding oscillation frequency and oscillation wavenumber are listed for six modes. Here, the beam current 0.5 kA has been assumed. As is clearly shown in the table, the maximum temporal growth rates of the higher modes are much smaller than that of the fundamental  $\text{TM}_{01}$  mode. Accordingly, oscillations of higher modes may be ignored in the scope of the present linear analysis. Of course, mode competitions may be expected in large diameter BWO's at the saturated level of oscillation in general. At the linear stage, however, mode competitions are insignificant in the large diameter SWS, if the size and beam parameters are carefully chosen. For this reason, we limit ourselves the subsequent analysis to the fundamental  $\text{TM}_{01}$  mode.

The dashed curves in Fig. 3 are for the case of  $V_b = 65$  keV. The temporal growth rate  $\text{Im}(\omega)$  for  $V_b = 65$  keV shown by the dashed curve in Fig. 3(b) is considerably smaller than that for  $V_b = 100$  keV shown by the solid curve. This difference suggests that, like conventional BWO's, there exists a starting energy threshold for oscillation in a finite length large diameter SWS as will be analyzed in the next subsection.

In Fig. 3, the real wavenumber  $k$  has been assumed. The real  $k$  means that we have assumed a sinusoidal small origin of oscillation with infinite extent in the  $z$  direction and have calculated its temporal evolution. On the other hand, in the case of a localized small origin of disturbance for the

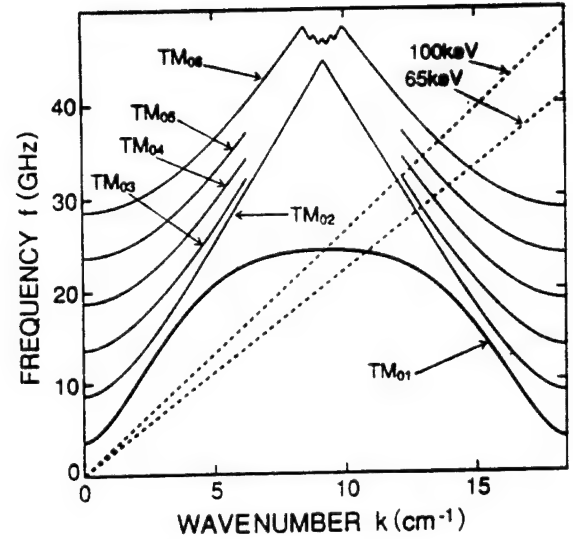


Fig. 4. The dispersion curves for  $\text{TM}_{01}$ , ...,  $\text{TM}_{06}$  modes. The two dashed lines are the beam lines for 100 and 65 keV with infinitesimal currents respectively. The crossing points of the beam lines and structure curves give possible oscillation frequencies.

TABLE I  
COMPARISON OF OSCILLATION OF SIX MODES INCLUDING THE FUNDAMENTAL  $\text{TM}_{01}$  MODE. THE OSCILLATION WAVENUMBER AND FREQUENCY AT THE MAXIMUM TEMPORAL GROWTH RATE ARE LISTED FOR OUR DESIGNED LARGE DIAMETER SLOW WAVE STRUCTURE. BEAM ENERGY AND CURRENT ARE, RESPECTIVELY 100 KEV AND 0.5 KA

Mode	Oscillation Wavenumber ( $\text{cm}^{-1}$ )	Oscillation Frequency (GHz)	Maximum Temporal Growth Rate (rad/ns)
$\text{TM}_{01}$	9.8	24.1	0.195
$\text{TM}_{02}$	12.3	30.4	0.0048
$\text{TM}_{03}$	12.5	30.9	0.0118
$\text{TM}_{04}$	12.8	31.8	0.0142
$\text{TM}_{05}$	13.3	33.1	0.0132
$\text{TM}_{06}$	14.0	34.8	0.0132

instability, the origin develops asymptotically with temporal and spatial factors  $t^{-1/2} \exp[-i(\omega_s t - k_s z)]$ , as was shown in (2.22) in [21]. Here,  $\omega_s$  and  $k_s$  are, respectively, the complex angular frequency and complex wavenumber at the saddle point  $\partial\omega_s/\partial k_s = 0$  in (5). The localized origin can monotonically grow up in time at every point in  $z$ . This is therefore an absolute instability. Once an unstable root of (5) in Fig. 3 is found, it is not very difficult to access the saddle point,  $\omega_s$  and  $k_s$ , which exists uniquely for a given set of parameters, by using the Newton-Raphson technique. In the saddle point analysis of the large diameter BWO, it is found that the oscillation frequency  $\text{Re}(\omega_s)/2\pi$  and the temporal growth rate  $\text{Im}(\omega_s)$  are, respectively, slightly decreasing and increasing functions of  $I_b$ , and the spatial growth rate  $\text{Im}(k_s)$  is almost unchanged with increase in  $I_b$ .

### B. Finite Length Slow Wave Structure

In a large diameter SWS with finite length  $L$  as shown in Fig. 1, the wave reflections (or leakages) at both ends are taken into account. The end reflections result in a feedback mechanism by the backward structure wave, and the distinct



tion between absolute and convective instabilities becomes somewhat ambiguous in the  $L$  finite case. The complex wavenumbers of the slow space charge wave and the backward structure wave are denoted, respectively, by  $a_+$  and  $a_-$ . In the limit of infinite  $L$ ,  $a_+$  ( $= a_-$ ) coincides with the saddle point of (5). For  $L$  finite cases, the following equations must be satisfied instead of (5), [20].

$$D(a_+, \omega) = 0 \quad (6)$$

$$D(a_-, \omega) = 0 \quad (7)$$

$$R \exp [-i(a_- - a_+)L] = 1. \quad (8)$$

Equation (8) comes from the requirement that the electromagnetic field must be a single value at every  $z$  point, when the propagating wave comes back after one round trip [20]. In (8),  $R$  is the one round trip reflection coefficient of wave fields at the both ends of the SWS, and assumed to be a given parameter. The length  $L$  is assumed to be  $L = 70z_0 = 23.8$  cm. In general, the reflection coefficient  $R$  in (8) must be a complex number, however, for simplicity it is approximately replaced by a real number  $0 < R < 1$  in the subsequent analysis. This is because the argument of the complex number causes only changes in equivalent structure length less than  $z_0$  much smaller than  $L$ . The additional requirement given by (8) results in the existence of the starting energy in addition to a nonzero starting current in finite  $L$  BWO's. Equation (8) is rewritten as

$$\text{Re}(a_- - a_+) = -2\pi N/L > 0 \quad (9)$$

$$\text{Im}(a_- - a_+) = -\ln(R)/L > 0 \quad (10)$$

where  $N$  is an integer. The following analysis is limited to the case  $N = -1$  in (9), because  $N = -1$  is the easiest case for initiating oscillation among various choices of  $N$  for a given  $L$ .

To solve (6)–(8) correctly, it is necessary to watch the movements of roots  $a_+$  and  $a_-$  on the complex  $k$  plane for various  $\omega$ 's with positive  $\text{Im}(\omega)$  approaching to zero [20], [21]. This is because the physical meaning (stable or unstable) of the each root is lost in the course of numerical calculation of (6)–(8). We must reconsider the physical meaning through watching the movement of the root on the complex  $k$  plane. If the particular root traverses the real axis during the change in  $\text{Im}(\omega)$  from a large positive number to zero, the root is unstable, otherwise it is stable. A pair of solutions  $a_+$  and  $a_-$  is shown on the complex  $k$  plane in Fig. 5(a) for the case of  $V_b = 100$  keV. The locations of the roots  $a_+$  and  $a_-$  are found at the centers of the contour mapping of  $|D'|$  given by (6)–(8) on the complex  $k$  plane. The corresponding common value of complex  $\omega/2\pi = 24.103 + i0.063$  is found in Fig. 5(b) for both  $a_+$  and  $a_-$  shown by black circles on the same complex  $k$  plane as Fig 5(a). The white circles in Fig. 5(b) are the locations of  $\text{Im}(\omega) = 0$  that give the boundary lines between BWO's ( $\text{Im}(\omega) > 0$ ), and TWT's ( $\text{Im}(\omega) < 0$ ). The arrows on the solid lines show the directions of decrease in  $\text{Im}(\omega)/2\pi$  toward zero for constant  $\text{Re}(\omega)/2\pi$ . The diamond is the saddle point of (5). In  $L$  infinite case, oscillation (absolute

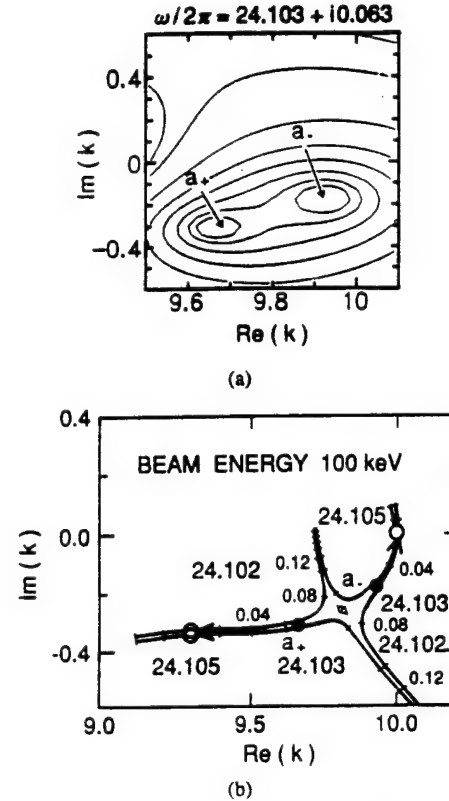


Fig. 5. Locations of the pair of roots,  $a_+$  and  $a_-$ , on the complex  $k$  plane for  $V_b = 100$  keV and  $I_b = 0.4$  kA,  $L = 23.8$  cm,  $N = -1$  and  $\omega/2\pi = 24.103 + i0.063$ . (a) Contour mapping of  $|D|$  where  $D$  is defined by (5). (b) Locations of the roots (black circles) that are in the oscillation region within border lines of  $\text{Im}(\omega) \geq 0$  shown by white circles. The diamond is the saddle point.

instability) is expected at the saddle point as was stated in the previous subsection, if it is located in  $\text{Im}(\omega) \geq 0$  region in complex  $k$  plane. In this case, oscillation is expected even for infinitesimal beam currents and no limitations exist for starting energy. In  $L$  finite case, however, the oscillation happens not at the saddle point but at  $a_+$  obtained from (6)–(8). Oscillation is impossible, if the pair of the roots are located in  $\text{Im}(\omega) \leq 0$  region. Because the black circles are located in the region  $\text{Im}(\omega) > 0$  in Fig. 5(b), the oscillation can be expected in the present case of  $V_b = 100$  keV. Since we have chosen  $L = 23.8$  cm and  $N = -1$ ,  $\text{Re}(a_- - a_+) = 0.264 \text{ cm}^{-1}$  from (9) is a fixed value, which is independent of the value of reflection coefficient  $R$ . The horizontal distance between  $a_+$  and  $a_-$  is a constant  $0.264 \text{ cm}^{-1}$  on the complex  $k$  plane shown in Fig. 5(b).

A pair of solutions  $a_+$  and  $a_-$  in (6)–(8) in the case of  $V_b = 65$  keV is shown on the complex  $k$  plane in Fig. 6. Other parameters are the same as those in Fig. 5. The corresponding common value of complex  $\omega/2\pi = 23.295 - i0.092$  is found in Fig. 6 for both  $a_+$  and  $a_-$  shown by black circles. In this case,  $a_+$  and  $a_-$  are located in the region of TWT's,  $\text{Im}(\omega) < 0$ , and oscillation cannot occur for  $V_b = 65$  keV, although the beam current  $I_b = 0.4$  kA is identical to that for  $V_b = 100$  keV in Fig. 5. Comparing Figs. 5(b) and 6, one finds that there may exist a threshold value in the beam energy  $V_b$  below which oscillation in the BWO's stops, no matter how

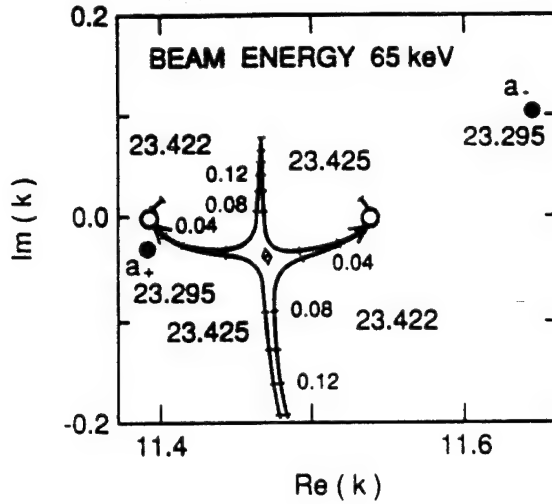


Fig. 6. Locations of the pair of roots,  $a_+$  and  $a_-$ , on the complex  $k$  plane for  $V_b = 65$  keV and  $I_b = 0.4$  kA,  $L = 23.8$  cm,  $N = -1$  and  $\omega/2\pi = 23.295 - i0.092$ . Locations of the roots (black circles) are outside the oscillation region  $\text{Im}(\omega) \geq 0$  shown by white circles. The diamond is the saddle point.

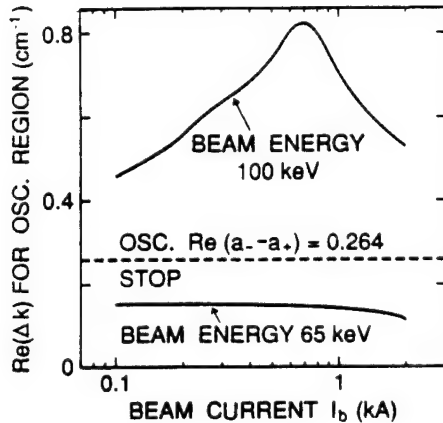


Fig. 7. Allowable oscillation regions of two solid curves for  $V_b = 100$  and 65 keV, i.e., horizontal separation of open circles as shown in Figs. 5(b) and 6 versus beam current  $I_b$ . The dashed line is the horizontal separation  $\text{Re}(a_- - a_+) = 0.264 \text{ cm}^{-1}$  of the roots for  $I_b = 0.4$  kA,  $L = 23.8$  cm, and  $N = -1$  in (9).

large the beam current  $I_b$ . This statement is clarified in Fig. 7, where the fixed horizontal separation between two black circles  $\text{Re}(a_- - a_+) = 0.264 \text{ cm}^{-1}$  given from (9) is shown by a horizontal dashed line. Two solid curves are the horizontal separations  $\text{Re}(\Delta k)$  between two white circles, respectively, as shown in Figs. 5(b) and 6 as functions of  $I_b$ . Here,  $\text{Re}(\Delta k)$  is the allowable range of oscillation for a given  $I_b$ . In the case

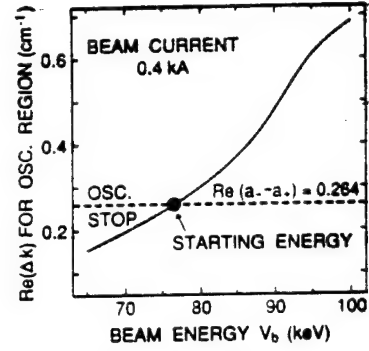


Fig. 8. Oscillation region versus beam energy  $V_b$ . The dashed line is the horizontal separation  $\text{Re}(a_- - a_+) = 0.264 \text{ cm}^{-1}$  for  $I_b = 0.4$  kA,  $L = 23.8$  cm, and  $N = -1$ . The black circle is the starting energy.

of  $V_b = 100$  keV, the solid curve always lies above the dashed line. This fact suggests that the oscillation is possible. On the other hand, in the case of  $V_b = 65$  keV, the curve stays below the dashed line, and oscillation does not occur.

For a given current  $I_b = 0.4$  kA, the starting energy for oscillation is found in Fig. 8, where the horizontal separations  $\text{Re}(\Delta k)$  of white circles such as those in Fig. 5(b) or 6 versus  $V_b$  are plotted. It is clearly shown that the starting energy denoted by the black circle is 76.5 keV for the given parameters of the present large diameter SWS. The larger length  $L$ , the smaller starting energy, because the dashed line becomes lower. It must be emphasized, however, that the starting energy is not a sufficient condition, but a necessary condition for initiating oscillation in the finite length SWS. In order to have oscillation, the pair of roots  $a_+$  and  $a_-$  must also satisfy (10) in addition to (9). This additional condition yields the starting current for oscillation. Equation (10) includes the reflection coefficient  $R$  as a given parameter, and the starting current  $I_{st}$  is affected sensitively by  $R$ . The results are shown in Fig. 9, where  $I_{st}$  versus  $R$  is calculated for  $V_b = 100$  keV and  $L = 23.8$  cm. It is reasonably shown that  $I_{st}$  is decreasing function of  $R$ . If we take into account the effect of the fourth wave (forward structure wave) as an additional feedback mechanism in (8), an oscillatory nature arises in the curve  $I_{st}$  versus  $L$ , as was pointed out in [13], [16].

#### IV. DISCUSSION AND CONCLUSIONS

A large diameter backward wave oscillator of  $D/\lambda \sim 4$  has been designed and analyzed numerically in detail. The key point of the design study is to raise the oscillation frequency without decreasing the mean diameter of the SWS. In our linear analysis, parameter selection for such purposes has been readily performed.

It was shown in the previous section that there existed a starting current of the beam required to withstand the leakage of radiation at both ends of SWS. Moreover, there existed a starting energy of the incident beam, below which oscillation could not occur, because of the finite length of the SWS. These two statements are never trivial and the distinction between both conditions has not been clarified in the literatures in the past. The former condition for the starting current giver

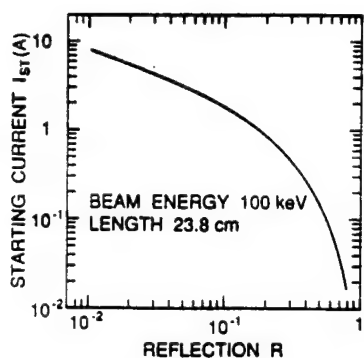


Fig. 9. Starting current  $I_{st}$  versus reflection coefficient  $R$  for beam energy  $V_b = 100$  keV,  $L = 23.8$  cm, and  $N = -1$ .

by (10) arises from the requirement that the radiation loss depending on  $I_b$  at the ends of the SWS must be smaller than a threshold value. In other words, the external  $Q$  value of the corrugated wall resonator shown in Fig. 1 must be large enough for the occurrence of oscillations. The resonator must store a minimum amount of RF energy for oscillation. On the other hand, the latter condition for the starting energy given by (9) arises from the requirement that the coupling condition of real wavenumbers,  $\text{Re}(a_+)$  and  $\text{Re}(a_-)$ , between the donor of RF energy  $a_+$  (slow space charge wave) and the acceptor  $a_-$  (backward structure wave) becomes stringent, when  $L$  is small. The locations of the  $a_+$  and  $a_-$  on the complex  $k$  plane are considerably separated in relatively short  $L$  case, and the coupling condition, namely, phase matching condition of the waves at the ends may not be satisfied. This restriction,  $\text{Re}(\Delta k)$ , is relaxed in the case of large  $V_b$  as was shown in Fig. 8. This is the reason for the existence of the minimum starting energy for oscillation. This oscillation condition for  $V_b$  is peculiar to the finite  $L$  case, and such additional requirement for the coupling of waves did not occur in conventional infinite  $L$  case shown in Fig. 3. It is well known that beam wave interaction is strong near  $\pi$  or  $2\pi$  mode operation, where the group velocity of the backward structure wave is small. In  $L$  finite case, the oscillation may stop somewhere between two mode operations because of increased group velocity. This qualitatively well known fact is for the first time analyzed quantitatively in the present paper, and it is the significance of the starting energy analyzed in this paper.

The diffraction of the radiation at the ends of large diameter SWS relating the value of reflection coefficient  $R$  is a complicated problem to analyze, and it is not treated here. In our numerical analysis,  $L = 23.8$ ,  $R_0 = 3.0$ , and  $\lambda = 1.25$  cm. The structure length  $L$  may be considered to be longer enough than  $R_0$  and  $\lambda$ , and our analysis ignoring end diffraction problem may be qualitatively valid. The practical value of the reflection coefficient  $R$  of the large diameter SWS can be measured by means of vector network analyzers for a real fabricated sample. The coefficient  $R$  is estimated to be 0.2 at 20 GHz from a straight cylindrical waveguide assuming that the corrugation parameter  $\alpha = h/R_0 = 0.0567$  is small enough. Then, the starting current  $I_{st} = 1$  A is found in Fig. 9. In the previous section, we assumed the typical beam

current  $I_b = 0.4$  kA, which is 400 times larger than  $I_{st}$ . In such cases, overbunch instability may occur in the oscillation and degradation of the microwave output may result as was predicted and observed in [5] and [13]. In order to suppress the instability, we may raise  $I_{st}$  by decreasing the length  $L$  under the restriction that the pair of roots in (9) remain in the oscillation region shown in Fig. 5(b). On the other hand, space charge limiting current in a cylindrical pipe for the average radius  $R_0 = 3$  cm and beam radius  $R_b = 2.68$  cm is calculated to be  $17(\gamma^{2/3} - 1)^{3/2}/2 \ln(R_b/R_0) = 2.9$  kA, which is much larger than the present  $I_b$ , where  $\gamma$  is the relativistic factor. The nonlinear analysis [22] or numerical simulation [13] is required to predict the power level and the performances of the designed large diameter BWO.

The energy sources in gyrotrons are the beam velocity  $v_\perp$  perpendicular to the axial magnetic field. Electron beams with  $v_\perp/v_\parallel = 1.5 \sim 2$  are usually required for high efficiency operation in gyrotrons [2], [3]. For that purpose, a sophisticated technology to generate such spiral beams was devised by means of magnetron injection gun, and analytically and empirically adjusted nonuniform axial magnetic field profiles for optimized performance. In contrast to gyrotrons, BWO's are easy to operate, because beams with  $v_\perp/v_\parallel \ll 1$  are available, and uniform axial magnetic fields are usually applicable.

The growth rates of the large diameter BWO analyzed in the present paper are smaller than those in the conventional BWO's. This is mainly because we have chosen small  $\alpha = h/R_0$ . In fact, we carried out a preliminary measurement of BWO operation of our designed large diameter SWS. It was found that the microwave output at 21 GHz was quite small and that the operation was made in linear regime. It may be important to explore a possibility of enhancing the growth rates of radiation from the large diameter BWO. Our analysis has been confined to the case of very strong applied magnetic field. An extension of the present linear analysis to the finite magnetic field case, especially the case  $\omega \sim \Omega$ , is very important [6]. Here,  $\Omega$  is the relativistic electron cyclotron frequency.

Reference [23] pointed out that, in slow wave cyclotron devices with  $v_\parallel < \omega/k < c$ , the beam energy can be converted to wave energy through a transformation from  $v_\parallel$  to  $v_\perp$ . This device was called the slow wave electron cyclotron maser. Although they assumed a dielectric loaded smooth cylindrical configuration, their statement can be applied to a metal wall SWS [24], [25]. In fast wave devices such as gyrotrons, the normal Doppler shifted beam cyclotron wave,  $\omega = kv_\parallel + \Omega$ , is used to interact with structure TE modes. On the other hand, the anomalous Doppler shifted beam cyclotron wave,  $\omega = kv_\parallel - \Omega$ , may be available to interact with structure TM modes in our large diameter SWS. The growth rates in the large diameter BWO in the present paper may be resonantly enhanced by the novel effect suggested by Kho and Lin [23]. Moreover, they showed in their Fig. 6 that the slow wave electron cyclotron maser was more tolerant of beam momentum spread than a fast wave device (CARM) for high efficiency operation. Their results are especially encouraging in the case of high beam current in which beam qualities such



as momentum spread and emittance are greatly inferior to the beams generated from thermoionic cathodes [26].

In conclusion, the slow wave devices such as MWCG's will be a hopeful candidate for the purpose of generating multi-MW millimeter microwaves for a variety of advanced applications. The large diameter BWO studied in the present paper may be helpful for that purpose.

## REFERENCES

- [1] A. V. L. Gaponov-Grekhov and V. L. Granatstein, Ed., *High Power Microwave Applications for the 21st Century*. Dedham, MA: Artech House, 1994.
- [2] V. L. Granatstein and I. Alexeff, Ed., *High-Power Microwave Sources*. Dedham, MA: Artech House, 1987.
- [3] J. N. Benford and J. A. Swegle, *High Power Microwaves*. Boston, MA: Artech, 1992.
- [4] R. A. Kels *et al.*, "A high power backward-wave oscillator driven by a relativistic electron beam," *IEEE Trans. Plasma Sci.*, vol. PS-13, pp. 559-562, Dec. 1985.
- [5] Y. Carmel *et al.*, "From linearity toward chaos: Basic studies of relativistic backward-wave oscillators," *Phys. Rev. Lett.*, vol. 69, no. 11, pp. 1652-1655, Sept. 1992.
- [6] A. Vlasov *et al.*, "Relativistic backward-wave oscillators operating near cyclotron resonance," *Phys. Fluids B*, vol. 5, no. 5, pp. 1625-1638, May 1993.
- [7] S. P. Bugaev *et al.*, "Investigation of a millimeter-wavelength-range relativistic diffraction generator," *IEEE Trans. Plasma Sci.*, vol. 18, pp. 518-524, June 1990.
- [8] ———, "Relativistic multiwave Cerenkov generators," *IEEE Trans. Plasma Sci.*, vol. 18, pp. 525-536, June 1990.
- [9] D. K. Abe, "Experimental studies of overmoded high power microwave generators," Ph.D. dissertation, Univ. Maryland, College Park, 1992.
- [10] Y. Carmel *et al.*, "High-power microwave generation by excitation of a plasma-filled rippled boundary resonator," *IEEE Trans. Plasma Sci.*, vol. 18, pp. 497-506, June 1990.
- [11] X. Zhai *et al.*, "Observation of Trivelpiece-Gould modes in a plasma filled backward wave oscillator," *Phys. Rev. A*, vol. 45, no. 12, pp. R8336-R8339, June 1992.
- [12] J. A. Swegle *et al.*, "Scaling studies and time-resolved microwave measurements on a relativistic backward-wave oscillator," *IEEE Trans. Plasma Sci.*, vol. 21, pp. 714-724, Dec. 1993.
- [13] B. Levush *et al.*, "Theory of relativistic backward-wave oscillators with end reflections," *IEEE Trans. Plasma Sci.*, vol. 20, pp. 263-280, June 1992.
- [14] Y. Carmel *et al.*, "Relativistic plasma microwave electronics: Studies of high-power plasma-filled backward-wave oscillators," *Phys. Fluids B*, vol. 4, no. 7, pp. 2286-2292, July 1992.
- [15] J. A. Swegle, "Starting conditions for relativistic backward wave oscillators at low currents," *Phys. Fluids*, vol. 30, no. 4, pp. 1201-1211, Apr. 1987.
- [16] K. Minami *et al.*, "Analysis of starting currents in a backward wave oscillator with finite structure length," *J. Phys. Soc. Jpn.*, vol. 61, no. 10, pp. 3566-3575, Oct. 1992.
- [17] M. R. Amin *et al.*, "Analysis of the electromagnetic waves in an overmoded finite length slow wave structure," *IEEE Trans. Microwave Theory Tech.*, vol. 43, Apr. 1995.
- [18] J. A. Swegle *et al.*, "Backward wave oscillators with rippled wall resonators: Analytic theory and numerical simulation," *Phys. Fluids*, vol. 28, no. 9, pp. 2882-2894, Sept. 1985.
- [19] K. Minami *et al.*, "Linear theory of electromagnetic wave generation in a plasma-loaded corrugated-wall resonator," *IEEE Trans. Plasma Sci.*, vol. 18, pp. 537-545, June 1990.
- [20] M. M. Ali *et al.*, "Linear analysis of a finite length plasma-filled backward wave oscillators," *Phys. Fluids B*, vol. 4, no. 4, pp. 1023-1032, Apr. 1992.
- [21] R. J. Briggs, *Electron-Stream Interaction with Plasmas*. Cambridge, MA: MIT Press, 1964.
- [22] T. Watanabe *et al.*, "Effect of beam energy spread on radiation intensity in a high-power backward wave oscillator with finite length," *J. Phys. Soc. Jpn. Lett.*, vol. 61, no. 4, pp. 1136-1140, Apr. 1992.
- [23] T. H. Kho and A. T. Lin, "Slow-wave electron cyclotron maser," *Phys. Rev. A*, vol. 38, no. 6, pp. 2883-2888, Sept. 1988.
- [24] E. Jerby and G. Bekefi, "Cyclotron-maser experiments in a periodic waveguide," *Phys. Rev. E*, vol. 48, pp. 4637-4641, Dec. 1993.
- [25] K. P. Maheshwari *et al.*, "Cherenkov-cyclotron resonance interaction in a high-power plasma-filled backward-wave oscillator," *Phys. Rev. A*, vol. 45, pp. 5866-5871, Apr. 1992.
- [26] W. W. Desler and S. K. Guharay, Eds., *High Brightness Beam for Advanced Accelerator Applications*. New York: AIP press, 1992.



K. Minami was born in Japan in 1938. He received the B.S. (EE) degree at Nagoya Institute of Technology in 1962, the M.S. (EE) degree at the Tokyo Institute of Technology in 1964, and the Ph. D. degree at Nagoya University in 1969.

Since 1986, he has been a Professor in the Electrical Engineering Department of Niigata University, Japan. His research interests include the generation of high-power microwave radiation, and interactions between powerful microwaves and plasmas.



K. Ogura was born in Japan in 1957. He received the B.Sc. degree in physics from Okayama University in 1981, and the M.Sc. and D.Sc. degrees in physics from Kyoto University in 1983 and 1989, respectively.

He is as an Associate Professor in the Electrical and Electronic Engineering Department of Niigata University. His research interests include high-power microwave oscillators and their applications to plasma heating.

Y. Aiba, photograph and biography not available at the time of publication.



M. R. Amin was born in Rangpur, Bangladesh in 1959. He received the B.Sc. (EEE) degree from the University of Rajshahi in 1984 and the M.Sc. (EEE) degree from Bangladesh University of Engineering and Technology, Dhaka, Bangladesh in 1987. He is pursuing the Ph.D. degree at Niigata University, Japan.

He is now on sabbatical from Bangladesh Institute of Technology, Rajshahi, where he is an Assistant Professor in the Electrical and Electronic Engineering Department. His research interests include

theoretical and experimental investigations of high-power microwave devices and semiconductor power electronic drives.

Mr. Amin is a member of the Institution of Engineers Bangladesh (IEB) and the Physical Society of Japan.



X. D. Zheng was born in Shandong, China in 1962. He received the B.S. and the M.S. degrees in optical engineering from Zhejiang University, Hangzhou, China in 1982 and 1986, respectively. He is pursuing the Ph.D. degree at Niigata University, Japan.

His research interests include theoretical and experimental investigations of high-power microwave devices, and optical measurements.



T. Watanabe was born in Japan in 1941. He received the B.S. degree in physics from the Tokyo Institute of Technology in 1964, and the M.S. and Ph.D. degrees from Nagoya University in 1966 and 1969, respectively.

He is currently with the National Institute for Fusion Science, Nagoya. His research interests include nonlinear plasma dynamics, and a generalized scheme to solve numerically a variety of systems of nonlinear equations.

W. W. Dettler (M'84-SM'90-F'92), photograph and biography not available at the time of publication.

V. L. Granatstein (S'59-M'64-Sm'86-F'92), for a photograph and biography, see page 524 of the October 1994 issue of this TRANSACTIONS.

Y. Carmel (S'66-M'69-SM'90), for a photograph and biography, see page 577 of the October 1994 issue of this TRANSACTIONS.

# Analysis of the Electromagnetic Waves in an Overmoded Finite Length Slow Wave Structure

Md. Ruhul Amin, K. Ogura, H. Kitamura, K. Minami, T. Watanabe, Y. Carmel, *Senior Member, IEEE*,  
W. Main, J. Weaver, W. W. Destler, *Fellow, IEEE*, and V. L. Granatstein, *Fellow, IEEE*

**Abstract**—The electromagnetic fields of the higher order axial resonant modes in a slow wave structure are analyzed and found to have considerably different characteristics from those of the conventional fundamental mode. Here, the reflections at both ends produce axial resonant modes corresponding to axisymmetric transverse magnetic (TM) modes. The period of field modulation of some of the higher order axial modes is shorter than that of the usual mode in a cylindrical waveguide, which could be of practical interest for higher power, higher frequency operation of backward wave oscillators. A perturbation technique is used to ascertain the field distribution inside the resonant cavity, and the numerical results thus obtained are compared to some experimental data.

## I. INTRODUCTION

THE growing need for coherent, efficient, and high power microwaves has led to the development of a number of innovative devices, including backward wave oscillators (BWO's), which are a promising class of devices having a number of useful features, namely: high spectral purity microwave power, frequency tunability, high efficiency, etc. [1]–[5]. For example, for an overmoded structure,  $D/\lambda > 1$ , 7% frequency tunability in the frequency range 5.2–5.6 GHz has been reported [6]. Here,  $D$  is the mean diameter of the waveguide and  $\lambda$  is the wavelength. Microwave radiations on the order of 1 GW at a frequency up to 30 GHz have been obtained [7], [8]. Continuous efforts are being made to enhance the power and frequency level of the devices.

In the slow wave devices, the interaction of electromagnetic (EM) quantities takes place inside the slow wave structures (SWS). In order to understand the physics of the mechanism involved, it is necessary to analyze the SWS in a realistic way. Resonators are also used in linear accelerator (linac), but their geometries are considerably different from those used in BWO's. The EM behaviors of the linac cavities have been extensively studied by many researchers using numerical computational techniques. In order to study the accelerator cavities with complex geometries, computational codes such as SUPERFISH [9], URMEL-T [10], etc., have

been developed. These codes are based on the discretization techniques of Maxwell's and Helmholtz's equation, in general. The computational time of these codes depends on the number of mesh points, geometry of the cavity, boundary conditions, and accuracy demanded for the particular purpose. A brief description of the numerical codes generally used in linac studies is presented in [11] by Cooper and Jones. In this work, an attempt has been made to explore the EM quantities of a sinusoidally corrugated SWS typically used in the BWO experiments in the simplest way, by using analytic equations derived for this purpose. In the BWO's, the finite axial dimension of the SWS causes reflections from the ends and, thereby, quantization of the axial wavenumber results in axial resonant modes. The finite transverse dimension of the SWS limits the power handling capability due to the internal RF breakdown. In order to overcome such a problem, one can increase the mean diameter of the SWS, thus creating an overmoded system. In general, many higher modes can be oscillated in such an overmoded SWS. It is still possible to operate the BWO preferentially at a particular mode with higher frequency by carefully selecting the beam and size parameters. This is because the respective modes have different starting current for oscillation with each other. This difference can be carefully used to select the particular mode for oscillation. In fact, recent experiments have shown that efficient and high power output can be achieved in such devices operating in a single mode [6]. Despite the numerous studies on conventional, weakly relativistic microwave tubes, more detailed studies of the resonant modes in the finite length SWS's intended for operation with highly relativistic electron beams are required. The motivation of the present work is the recent interest in the generation of high power microwave radiation employing overmoded slow wave systems. Most of the analyses of such systems were performed assuming infinite length systems or perfectly matched finite length systems, which are far from the actual experiments. Moreover, their analyses have been restricted mainly to the fundamental mode [12]–[18]. In this paper, we model a finite length SWS consistent with real experiments and include higher order modes in our computations. Specifically, we consider the two wave interaction process with 100% round-trip reflection. Under this assumption, our SWS becomes an SWS cavity with perfectly shorted ends. Detailed field calculations along with higher harmonic analysis of the axial resonant modes in the SWS have been made. For the higher order axisymmetric TM modes ( $TM_{0s}$ ,  $s > 1$ ), some unusual and novel phenomena

Manuscript received March 11, 1994; revised August 4, 1994.

M. R. Amin, K. Ogura, H. Kitamura, and K. Minami are with the Graduate School of Science and Technology, Niigata University, Niigata City, 950-21, Japan.

T. Watanabe is with the National Institute for Fusion Science, Nagoya, 464-01, Japan.

Y. Carmel, J. Weaver, W. W. Destler, and V. L. Granatstein are with the Institute for Plasma Research, University of Maryland, College Park, MD 20742 USA.

W. Main is with ACCURAY Inc., Santa Clara, CA USA.

IEEE Log Number 9408564.

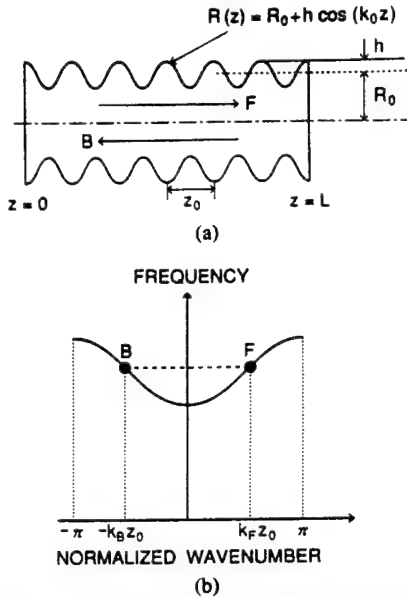


Fig. 1. Schematic diagram of a spatially periodic slow wave structure (SWS) showing the directions of forward propagating wave  $F$  and backwardly propagating wave  $B$ . (a) SWS shorted at  $z = 0$  and  $z = L$  and (b) locations of the  $F$  and  $B$  waves in the dispersion curve in the first Brillouin zone.

have been found for the first time regarding the amplitude of the spatial harmonic components of the resonant modes for particular values of the axial wavenumber. Cavity perturbation technique [19] has been employed to calculate the resonant frequency shift of the cavity. Some of the present numerical results are compared to experimental and numerical results obtained by using SUPERFISH in [20], and are found to be in excellent agreement.

The organization of the paper is as follows. In Section II, we present the mathematical formulation of the SWS. Section III describes the numerical results of the analysis. The cavity perturbation technique and the corresponding numerical and experimental results are given in Section IV. In Section V, discussion and conclusion of the present works are presented.

## II. MATHEMATICAL FORMULATION

First, we consider an infinite length SWS; next, after imposing additional axial boundary condition to the system, we will obtain the EM field quantities in a finite length SWS. As depicted in Fig. 1(a), the SWS is assumed to be sinusoidally corrugated in the axial direction with radius  $R(z) = R_0 + h \cos k_0 z$ , where  $k_0 = 2\pi/z_0$ . Physical quantities associated with an EM mode are represented by a spatial harmonic series satisfying Floquet's theorem. For axisymmetric TM modes, the axial electric field  $E_z$  can be expressed as [14], [16]

$$E_z(z, r, t) = \sum_{n=-\infty}^{\infty} A_n J_0\left(\frac{x_n}{R_0} r\right) e^{i(k_n z - \omega t)} \quad (1)$$

where  $J_0$  is the 0th-order Bessel's function of the first kind,  $x_n^2 = R_0^2(\omega^2/c^2 - k_n^2)$ ,  $k_n = k + nk_0$ ,  $k$  is the axial wavenumber, and  $n$  is an integer. For slow spatial harmonic waves with  $x_n^2 < 0$ , Bessel's function  $J_0$  becomes the modified Bessel's function  $I_0$ . Although the contributions of these

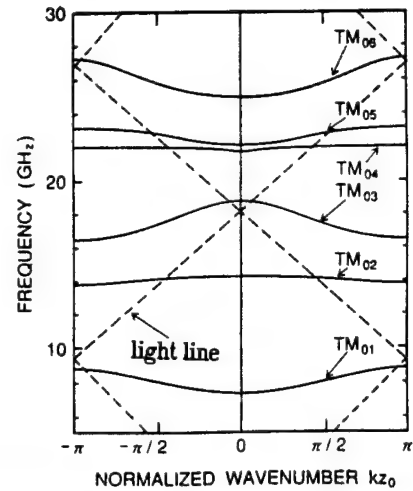


Fig. 2. Numerically obtained dispersion relations of the SWS for  $-\pi \leq k z_0 \leq \pi$  in the first Brillouin zone. The parameters of the SWS are:  $R_0 = 1.4499$  cm,  $z_0 = 1.67$  cm, and  $h = 0.406$  cm. Light lines ( $\omega/k = c$ ) are shown by dashed lines.

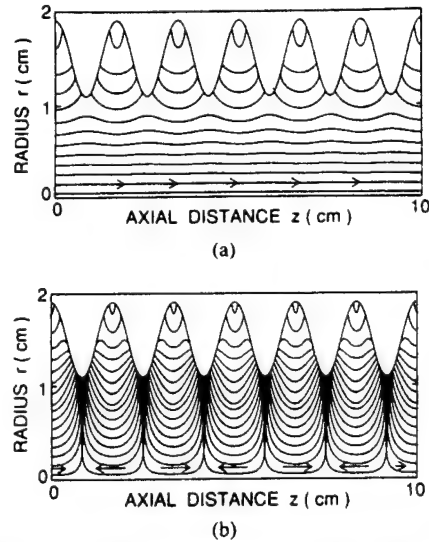


Fig. 3. Electric field patterns of the  $TM_{01}$  mode. SWS parameters are:  $R_0 = 1.499$  cm,  $z_0 = 1.67$  cm, and  $h = 0.406$  cm. Arrows indicate the direction of the electric field. The density of the field lines indicates the strength of electric field qualitatively. (a)  $TM_{01}(0\pi/6)$  mode and (b)  $TM_{01}(6\pi/6)$  mode.

harmonics are substantial inside the deep corrugation ( $r \sim R_0 + h$ ), this region is so small that we can still determine the EM characteristics inside the SWS correctly. The other components,  $E_r$  and  $H_\theta$ , are derived from  $E_z$ . The dispersion relation is obtained from the boundary condition at the wall of the structure, i.e., the tangential component of electric field should be zero at  $r = R(z)$ . The  $m$ th spatial Floquet harmonic components of this boundary condition can be expressed as

$$\sum_{n=-\infty}^{\infty} A_n \int_{-z_0/2}^{z_0/2} e^{i(n-m)kz} \left( 1 + \frac{ik_n}{(\omega^2/c^2 - k_n^2)} \frac{\partial}{\partial z} \right) \cdot J_0\left(\frac{x_n}{R_0} R\right) dz = 0.$$

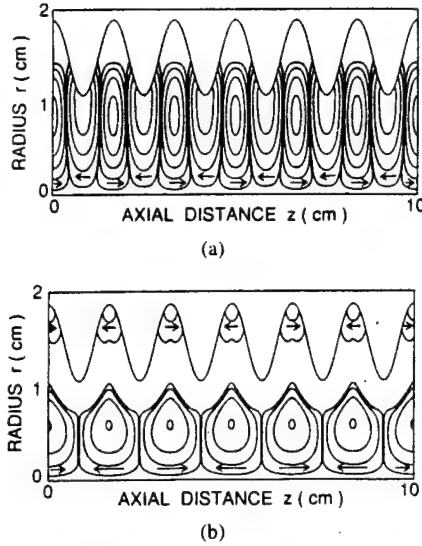


Fig. 4. Electric field patterns of the  $TM_{04}$  mode. SWS parameters are the same as in Fig. 3. Arrows indicate the direction of electric field. The density of the field lines indicates the strength of the electric field qualitatively. (a)  $TM_{04}(0\pi/6)$  mode and (b)  $TM_{04}(6\pi/6)$  mode.

In order to evaluate this integral, we used Taylor series expansion of the Bessel's function around  $R = R_0$ , since direct integration takes much time for computation. The radial boundary condition is imposed into the following matrix form:

$$[D] \cdot [A] = 0 \quad (2)$$

where  $[A]$  is a column vector with elements  $A_n$ , and  $[D]$  is a matrix of an infinite rank with each element given by  $D_{mn} = [1 + (n-m)Q_n]C_{mn}$  where

$$C_{mn} = \sum_{q=0}^{\infty} \frac{(x_n \alpha)^{2q+|n-m|} J_0^{(2q+|n-m|)}(x_n)}{2^{2q+|n-m|} q! (q+|n-m|)!} \quad (3)$$

$Q_n = k_0 k_n / (\omega^2/c^2 - k_n^2)$  and  $a = h/R_0$ . The dispersion relation is determined from the condition that (2) should have nontrivial solutions, and is given by

$$D(k, \omega) = \det[D] = 0. \quad (4)$$

In our practical calculation, the value of  $n$  is limited to  $-4 \leq n \leq 4$ , and  $2q + |n-m| \leq 10$  is chosen in (3). By comparing to direct integration, we have confirmed that the Taylor expansion of the Bessel's function converges quite rapidly and that the numerical errors are less than 1% for the fundamental mode with the parameters later described.

In the case of a finite length SWS, the additional boundary condition at both ends of the structure must be included. Referring to Fig. 1(a), a forward propagating wave  $F$  in the  $z$ -direction is reflected at  $z = L$  and becomes a backwardly propagating wave  $B$ . The locations of the waves on the dispersion curve are shown in Fig. 1(b). Both  $F$  and  $B$  waves have to satisfy (4). The  $F$  wave propagates from the  $z = 0$  boundary. After a round-trip with reflection at  $z = L$ , the resultant wave at the  $z = 0$  boundary should be "single" valued. This is a two wave interaction process, and the axial boundary condition can be expressed as [16]

$$Re^{i(k_F - k_B)L} = 1 \quad (5)$$

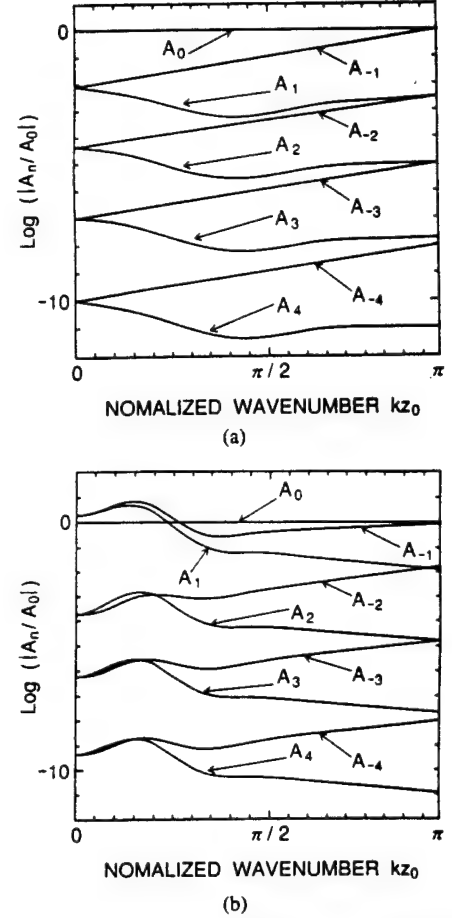


Fig. 5. Relative magnitude of the amplitude of the Floquet harmonics  $A_n$  versus normalized wavenumber for  $0 \leq kz_0 \leq \pi$ . (a)  $TM_{01}$  mode and (b)  $TM_{04}$  mode.

where  $R$  is the total reflection coefficient at the ends of the SWS, and  $k_F$  and  $k_B$  are the wavenumbers of the  $F$  and  $B$  waves, respectively. If the cavity is lossless and the ends are shorted with perfectly conducting metal plates, then  $R = 1$  and  $k_F = -k_B$  as shown in Fig. 1(b). Hence, from (5),  $k_F = N\pi/L$ , where  $N$  is an integer. Except for the propagating direction, the wave  $B$  is the same as the wave  $F$ . They satisfy identical radial boundary conditions and have the same energy. Therefore, in (1), the relationship between the coefficients  $A_n$  can be written as  $A_n^F = A_{-n}^B$ . By summing the  $F$  and  $B$  waves, the expressions of the EM fields in the SWS cavity become

$$E_z(z, r, t) = e^{-i\omega t} \sum_{n=-\infty}^{\infty} 2A_n J_0\left(\frac{x_n}{R_0} r\right) \cos(k_n z) \quad (6)$$

$$E_r(z, r, t) = R_0 e^{-i\omega t} \sum_{n=-\infty}^{\infty} \frac{2A_n k_n}{x_n} J_1\left(\frac{x_n}{R_0} r\right) \sin(k_n z) \quad (7)$$

$$H_\theta(z, r, t) = -i\epsilon_0 \omega R_0 e^{-i\omega t} \sum_{n=-\infty}^{\infty} \frac{2A_n}{x_n} J_1\left(\frac{x_n}{R_0} r\right) \cos(k_n z). \quad (8)$$

Once the dispersion relation (4) is solved numerically, the

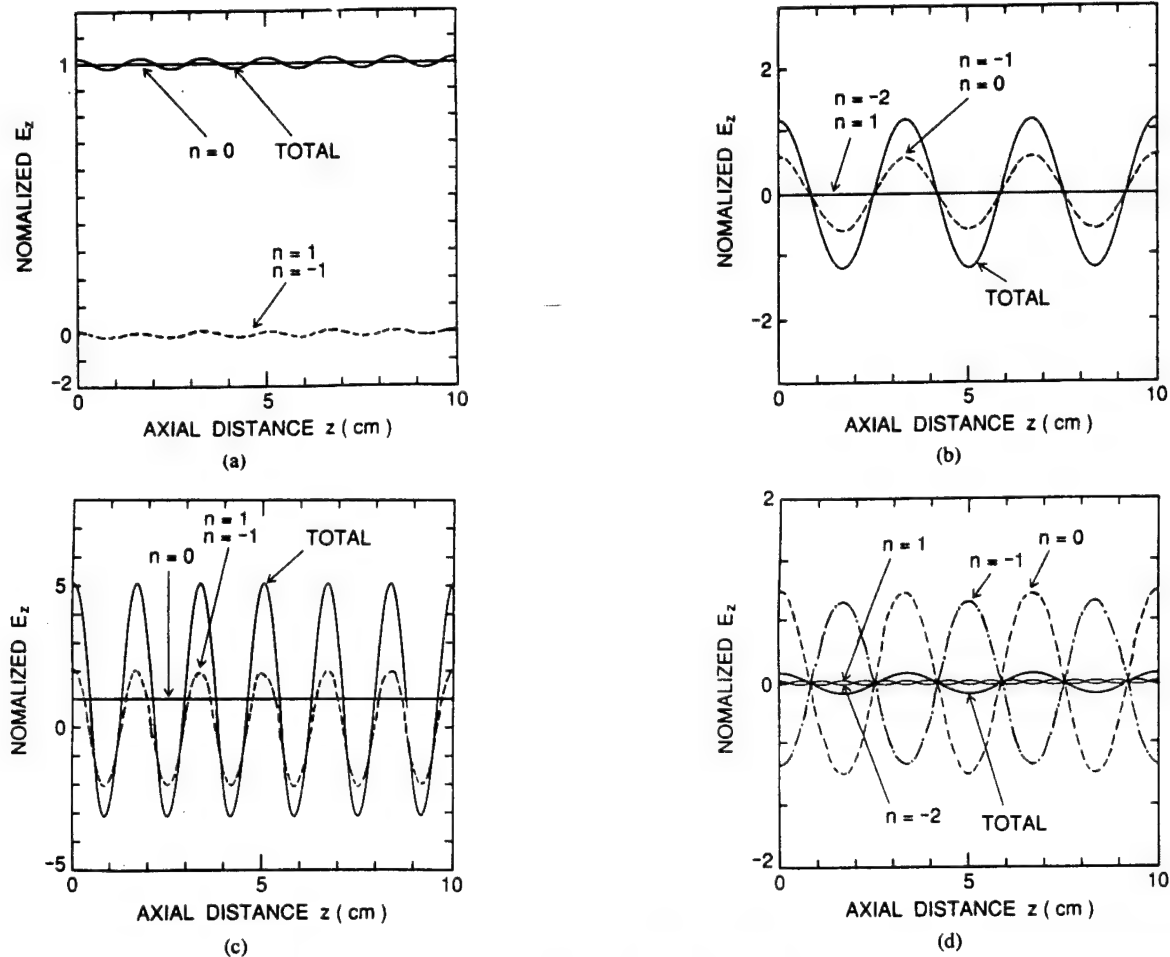


Fig. 6. Axial profiles of Floquet harmonics of field  $E_z$  at radial position  $r = 0$  for  $TM_{01}$  and  $TM_{04}$  modes. The higher order harmonics of small amplitudes are not shown in the figures. Thick, solid curves represent the total value of the electric field  $E_z$ . Thin, dashed and chained curves represent the Floquet harmonics as indicated by  $n$  in the figures. (a)  $TM_{01}(0\pi/6)$  mode, (b)  $TM_{01}(6\pi/6)$  mode, (c)  $TM_{04}(0\pi/6)$  mode, and (d)  $TM_{04}(6\pi/6)$  mode.

relative magnitudes between the  $A_n$  factors are determined from (2). With a known set of values of  $A_n$ , the normalized values of the fields  $E_z$ ,  $E_r$ , and  $H_\theta$  can be calculated from (6), (7), and (8), respectively.

### III. NUMERICAL RESULTS

In the present analysis, a six-period SWS having the following size parameters is considered: the mean radius  $R_0 = 1.499$  cm; the period of corrugation  $z_0 = 1.67$  cm; and the corrugation amplitude  $h = 0.406$  cm. These dimensions correspond to the experimental values used by our research group at the University of Maryland [20]. Fig. 2 depicts dispersion relations computed from (4). The dashed lines in the figure are the light lines in free space. The end reflections cause the six-period SWS to resonate at seven distinct frequencies corresponding to the particular TM modes. For the first Brillouin zone ( $-\pi < kz_0 < \pi$ ) of the dispersion relation, the values of the normalized wavenumber  $kz_0$  which correspond to the seven resonant axial modes are  $0\pi/6, \pi/6, 2\pi/6, 3\pi/6, 4\pi/6, 5\pi/6$ , and  $6\pi/6$ , respectively. We will designate these axial modes by  $TM_{0s}(N\pi/6)$  hereafter.

#### A. Electric Field Lines of the Fundamental Mode

Using the derived field equations in the SWS, the electric field lines are calculated. The method of computation is identical to that developed by Ogura *et al.* [18], with a modification for the higher order modes. Examples of the electric field patterns of the  $TM_{01}$  mode are depicted in Fig. 3(a) and (b), respectively, for  $TM_{01}(0\pi/6)$  and  $TM_{01}(6\pi/6)$  modes. The separations  $\Delta r$  between the field lines in the radial direction are so chosen that  $E_z \Delta r = \text{constant}$  at the axial position  $E_r = 0$ . The density of the field lines in the radial direction represents the strength of the electric field qualitatively. For the  $TM_{01}(0\pi/6)$  mode in Fig. 3(a), the electric field is fairly uniform in the axial direction, and the radial variation of the field has a maximum on the axis of the structure. The axial pattern of the fields has six zero points ( $E_z = 0$ ) for the  $TM_{01}(6\pi/6)$  modes as shown in Fig. 3(b). The periodic nature of the field lines depicted in Fig. 3(b) can be explained by the contribution of the Floquet harmonics for  $n = 0$  to the resonant axial modes.

#### B. Field Patterns of Higher-Order Modes

The numerical calculation of the field patterns for the higher order modes [ $TM_{0s}(s > 1)$ ] is complicated. We followed



an improved technique from the case of the fundamental mode [18], and have tried to calculate the electric field lines for the  $TM_{02}$ ,  $TM_{03}$ , and  $TM_{04}$  modes. Some of the results for the  $TM_{04}$  mode are presented in Fig. 4(a) and (b), respectively, for the case of  $TM_{04}(0\pi/6)$  and  $TM_{04}(6\pi/6)$  modes. The field patterns have fine and peculiar structures and differ considerably from those of the  $TM_{01}$  mode in Fig. 3. The radial distribution of the electric field lines in Fig. 4 is localized and separated into two parts: the peripheral and the central axis regions. The possible explanations for this difference can be given by the contribution of the Floquet harmonics involved in the SWS. This will be discussed in detail in the following subsection.

### C. Floquet Harmonics of the Electromagnetic Fields in the Structure

The number of Floquet harmonics to represent the EM fields are practically limited by the computation time and the relative magnitude of the amplitude factor  $A_n$ 's. The values of  $A_n$  differ from mode to mode as shown in Fig. 5(a) and (b), respectively, for  $TM_{01}$  and  $TM_{04}$  modes. In general,  $A_n$  decreases with increasing  $|n|$ , namely,  $A_0$  within the first Brillouin zone of the dispersion relation is the largest. In Fig. 5(a), at  $kz_0 = 0$ , the relation between  $A_n$ 's becomes  $|A_n| = |A_{-n}|$  and  $|A_n| \approx |A_{-n-1}|$  at  $kz_0 = \pi$ . At  $r = 0$ , the nonzero field component is  $E_z$ , and it is proportional to  $A_0 + A_{-1} \exp[-i(2\pi/z_0)z] + A_1 \exp[i(2\pi/z_0)z] + \dots$ . As shown in Fig. 5(a), the contribution of the  $n = 0$  Floquet harmonic to  $E_z$  is predominant, and the amplitudes of the higher order harmonics are very small except at  $kz_0 \approx \pi$  for the  $TM_{01}(6\pi/6)$  mode. For this reason, the field lines of the  $TM_{01}(0\pi/6)$  mode, as shown in Fig. 3(a), are almost straight lines for  $r \leq R_0$ . On the other hand, the field lines of the  $TM_{01}(6\pi/6)$  mode are determined by the  $n = 0$  and  $n = -1$  Floquet harmonics. These two harmonics have the same field variations in the  $z$ -direction with a period of  $2z_0$  and, hence, we obtain the field pattern with the periodicity depicted in Fig. 3(b).

For the  $TM_{04}$  mode in Fig. 5(b), the values of  $A_{\pm 1}$  become greater than  $A_0$  for small values of  $k$  within the first Brillouin zone of the dispersion curve. This result is novel and was not known in the previous works [14]–[16], [18]. The effects of this unusual behavior are observed in the electric field patterns of the structure shown in Fig. 4. In Fig. 5(b), as  $k$  increases,  $|A_n|$  approaches  $|A_{-n-1}|$  at  $kz_0 = \pi$ , as is observed for the  $TM_{01}$  mode in Fig. 5(a). The field quantities of the  $TM_{04}(0\pi/6)$  mode in Fig. 5(b) are nearly proportional to  $A_{-1} \exp[-i(2\pi/z_0)z] + A_1 \exp[i(2\pi/z_0)z]$ , which is periodic with period  $z_0$ . This fact can be seen from the field patterns of the  $TM_{04}(0\pi/6)$  mode as shown in Fig. 4(a). As  $kz_0$  approaches  $\pi$ , the field patterns of the  $TM_{04}(6\pi/6)$  mode near  $r = 0$  as shown in Fig. 4(b), have a periodicity  $2z_0$ , which is similar to that for the  $TM_{01}(6\pi/6)$  mode in Fig. 3(b).

The harmonic components of  $E_z(r = 0, z)$  are shown in Fig. 6(a) and (b) for the  $TM_{01}$  mode and in Fig. 6(c) and (d) for the  $TM_{04}$  mode. The EM fields are normalized by  $A_0$ . The thick, solid curves in the figures represent the total value

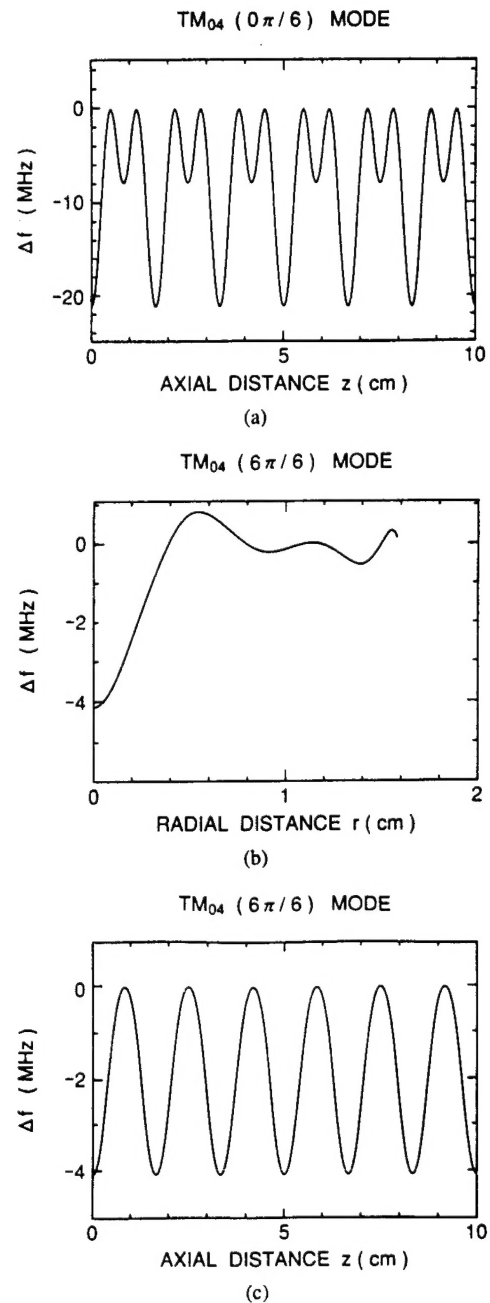


Fig. 7. Resonance frequency shift  $\Delta f$  of the axial resonant modes for the  $TM_{04}$  mode due to perturbation by a spherical metallic bead. (a) Axial changes in  $\Delta f$  of the  $TM_{04}(0\pi/6)$  mode for the bead at  $r = 0$ ; (b) radial changes in  $\Delta f$  of the  $TM_{04}(6\pi/6)$  mode for the bead at  $z = Nz_0$ ; (c) axial changes in  $\Delta f$  of the  $TM_{04}(6\pi/6)$  mode for the bead at  $r = 0$ . Here,  $N = 1, 2, \dots, 6$ .

of  $E_z$ . The thin, dashed and chained curves in Fig. 6 express  $E_z$  components at  $r = 0$  denoted by the harmonic number  $n$  in (1), which can be understood if one compares to the values of  $A_n$  at  $kz_0 = 0$  and  $kz_0 = \pi$  in Fig. 5(a) and (b). The amplitudes of the higher order harmonics not expressed are very small compared to those shown in Fig. 6. The  $z$ -direction periodicities of  $E_z$ —as depicted in Fig. 6(a)–(d)—correspond, respectively, to those of Figs. 3(a) and (b), and 4(a) and (b). In Fig. 6(a), the contribution of the  $n = \pm 1$  harmonics to  $E_z$  results in a small superimposed perturbation in the  $z$ -direction.

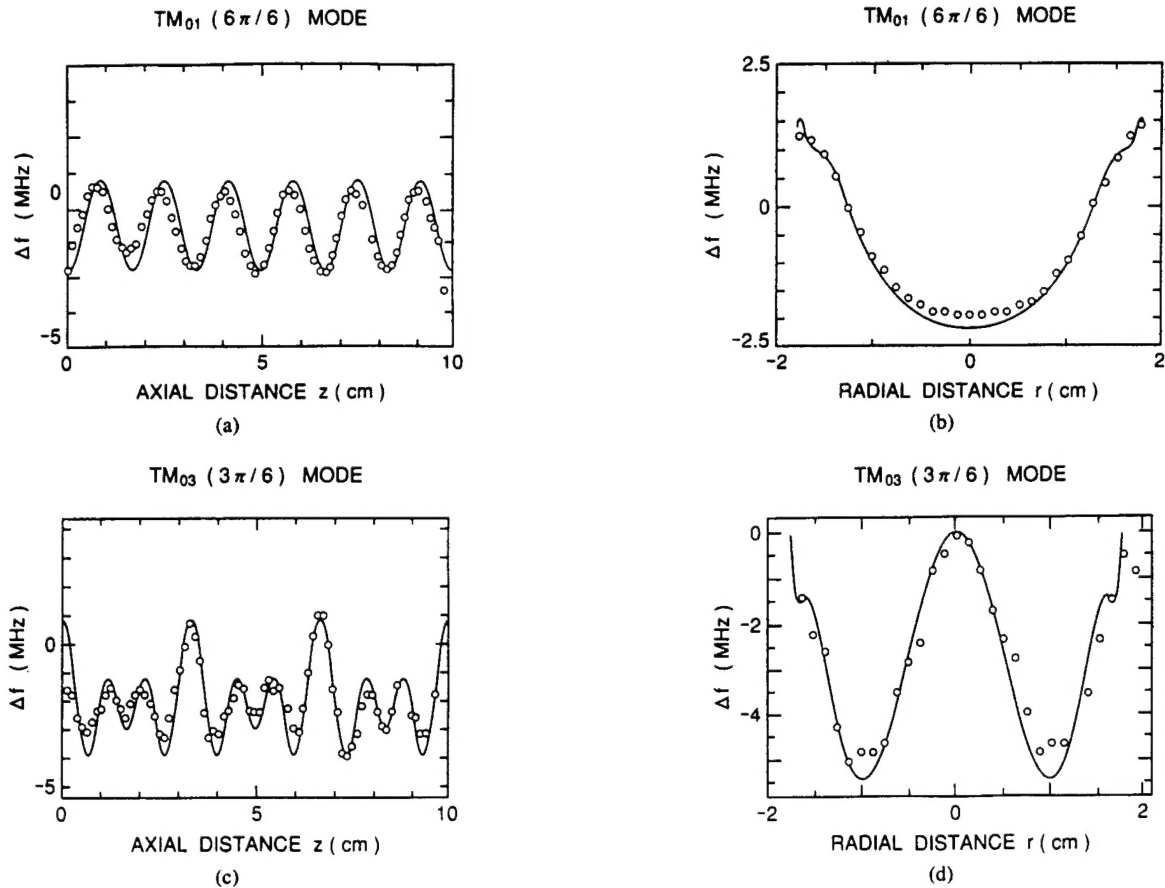


Fig. 8. Comparison of numerical and experimental results of frequency shift  $\Delta f$  by the displaced bead in axial and radial directions. The solid curves indicate the numerical results, and the open circles represent the corresponding experimental results. The axial data were measured by the bead at a radial position  $r = 0.543$  cm. (a) Axial changes in  $\Delta f$  for the  $TM_{01}(6\pi/6)$  mode; (b) radial changes in  $\Delta f$  for the  $TM_{01}(6\pi/6)$  mode; (c) axial changes in  $\Delta f$  for the  $TM_{03}(3\pi/6)$  mode; (d) radial changes in  $\Delta f$  for the  $TM_{03}(3\pi/6)$  mode.

The effect of this perturbation can easily be observed in the field lines for the  $TM_{01}(0\pi/6)$  mode in Fig. 3(a).

The above results for the  $TM_{04}$  mode are never trivial and have not been clarified in the past in the literature [14]–[18]. In usual cases, the fundamental  $A_0$  term is dominant in (1) as shown in Fig. 6(b) and (d); the shortest axial period of  $E_z$  is  $2z_0$  for  $kz_0 = \pi$ , as was shown by Fig. 3(b) and Fig. 4(b). On the other hand, in the special case where  $|A_{\pm 1}|$  is larger than  $A_0$ , as shown in Fig. 5(b), the axial period can become as small as  $z_0$  for  $kz_0 \approx 0$ , which is much shorter than the usual minimum period of  $2z_0$ .

#### IV. PERTURBATION TECHNIQUE

The perturbation technique is a powerful method to measure EM field variations inside the resonant cavity [19]. This technique has been employed in the following analysis of SWS cavity, and the numerical results have been compared to experimental ones obtained at the University of Maryland [20].

When there exists a small metallic sphere bead with radius  $r_0$  in the cavity, the EM fields in the cavity are perturbed and the resonance frequency of the cavity changes by an amount of  $\Delta f$ . If the perturbation is small enough,  $\Delta f$  can be calculated approximately with the unperturbed field quantities  $E_z, E_r,$

and  $H_\theta$  given by (6)–(8). The resultant expression for  $\Delta f$  becomes [19], [20]

$$\frac{\Delta f}{f_0} = \frac{\frac{4}{3}\pi r_0^3 (\frac{3}{2}\mu_0 |H_\theta|^2 - 3\epsilon_0 (|E_z|^2 + |E_r|^2))}{\int_V (\mu_0 |H_\theta|^2 + \epsilon_0 (|E_z|^2 + |E_r|^2)) dV}. \quad (9)$$

From (9), the field quantities are closely related to the frequency shift of the SWS cavity due to the bead. In the case of a spherical bead, the EM field quantities cannot be determined separately, because an unidirectional perturbation is impossible to achieve with the spherical bead perturber. The perturbation in  $E$  is always accompanied by a perturbation in  $H$ .

The calculated values of the frequency shift  $\Delta f$  for the  $TM_{04}$  mode, with a bead radius of 0.1195 cm, are presented in Fig. 7. The axial changes in  $\Delta f$  in Fig. 7 are calculated with the perturber at  $r = 0$ . The axial changes in  $\Delta f$  for the  $TM_{04}(0\pi/6)$  mode are shown in Fig. 7(a). The radial and axial changes in  $\Delta f$  for the  $TM_{04}(6\pi/6)$  mode are shown in Fig. 7(b) and (c), respectively. At  $r = 0$ ,  $E_r = H_\theta = 0$  and the only nonzero field component in (9) is  $E_z$ , and, hence,  $\Delta f$  in the axial direction as shown in Fig. 7(a) and (c), respectively, for  $TM_{04}(0\pi/6)$  and  $TM_{04}(6\pi/6)$  modes are directly proportional to  $-|E_z|^2$ . In other words, the results presented in Fig. 7(a) and (c) are proportional to the square of the axial profiles of total  $E_z$  in Fig. 6(c) and (d). Hence, at  $r = 0$ , we can obtain the quantitative information about



the axial electric field in the SWS from the  $\Delta f$  data. It should be noted that the solid curve in Fig. 6(c) is not symmetric regarding  $E_z$  ( $r = 0$ ) = 0. The curve in Fig. 7(a) is therefore not simply sinusoidal. For  $r \neq 0$ , however, using the spherical perturber, it is impossible to measure quantitatively the individual fields involved in  $\Delta f$ . The radial variations of  $\Delta f$  are dependent on  $E_z$ ,  $E_r$ , and  $H_\theta$ . In the case of  $r \neq 0$ , at the axial positions where  $E_r = 0$ , both contributions from  $E_z$  and  $H_\theta$  to  $\Delta f$  cannot be ignored as is seen from (9). The positive region in the radial profile of  $\Delta f$  for the  $TM_{04}(6\pi/6)$  mode, in Fig. 7(b), is ascribed to  $H_\theta$ . The axial variations of  $\Delta f$  for the  $TM_{04}(0\pi/6)$  mode, in Fig. 7(a), are very rapid compared to those for the  $TM_{01}(6\pi/6)$  mode, as shown in Fig. 8(a) by the solid curve. Experimentally, it is difficult to measure axial changes in  $\Delta f$  for the  $TM_{04}(0\pi/6)$  mode, in Fig. 7(a), because of the very rapid variation of the fields in the axial direction. However, the  $TM_{04}(6\pi/6)$  mode in Fig. 7(c) has variations of  $\Delta f$  similar to those observed for the  $TM_{01}(6\pi/6)$  mode in Fig. 8(a). These modes have field variations which are not very rapid in the axial direction as depicted in Fig. 6(b) and (d). The numerical results of  $\Delta f$  have been compared to experimental measurements [20], and some of these results are shown in Fig. 8. The axial and radial changes in  $\Delta f$  for the  $TM_{01}(6\pi/6)$  mode are shown in Fig. 8(a) and (b), respectively. The axial and radial changes in  $\Delta f$  for the  $TM_{03}(3\pi/6)$  mode are shown in Fig. 8(c) and (d), respectively. The open circles represent the experimental data, and the solid curves are the present numerical results. The numerical data presented in Fig. 8(a) and 8(c) are for the bead at a radial position  $r = 0.543$  cm from the axis. By comparing the frequency shift to the field profiles, one can determine the axial resonant modes in the SWS to be  $TM_{01}(6\pi/6)$  and  $TM_{03}(3\pi/6)$  modes. The agreement between the numerical and experimental results can be clearly estimated from the figures. The discrepancy between them lies within the range of 10–20%.

## V. DISCUSSION AND CONCLUSION

We have numerically analyzed the EM quantities of fundamental and higher order axial TM modes in a finite length SWS. It is found that, for the higher order modes, the amplitudes of the Floquet harmonics show unusual behavior as depicted in Fig. 5(b) for the  $TM_{04}$  mode. For the  $TM_{04}(0\pi/6)$  mode ( $kz_0 = 0$ ), the field quantities are mainly determined by the Floquet harmonics with  $n = -1$  and 1, and the fields have an unusual short period of  $z_0$  as shown in Figs. 4(a) and 6(c). This indicates that the period of field modulations can decrease to  $z_0$ , which is small compared to that for the usual modes in cylindrical waveguides where the period is larger than  $2z_0$ . Such a mode with short field modulations may become important for higher frequency operation of BWO's.

The numerical results presented in this paper are being verified experimentally at the University of Maryland [20]. Generally speaking, it is impossible to reconstruct the field distributions including phase change by the frequency shift measurements only, because the frequency shift is related to only the absolute values of the EM fields, as is seen from

(9). In some cases, however, the experimental results can be compared to the numerical calculations as shown in Fig. 8. It is concluded that the measured resonant modes are  $TM_{01}(6\pi/6)$  in Fig. 8(a) and (b), and  $TM_{03}(3\pi/6)$  in Fig. 8(c) and (d). The agreement between the numerical and experimental data is quite satisfactory.

To determine the dispersion characteristics of an SWS cavity, shorted plates are placed at both ends and the resonant modes are excited by a suitable mode launcher at one of the end plates. The degree of coupling between the mode launcher and the SWS determines the type of mode launcher to be used in the experiment. If the coupling between the mode launcher and the cavity is strong, complete reflection on the input antenna side cannot be expected. For a disc-type mode launcher, the reflection coefficient at the input end will be small, and consequently our assumption of perfectly shorted ends of the SWS becomes inapplicable. Hence, we prefer a short wire antenna at the center of the plate as a mode launcher to excite the cavity. However, it is difficult to excite the surface wave modes near  $kz_0 = \pi$ , as was reported in [20].

## REFERENCES

- [1] V. L. Granatstein and I. Alexeff, *High-Power Microwave Sources*. Boston, MA: Artech House, 1987.
- [2] R. A. Kehs, A. Bromborsky, B. G. Ruth, S. E. Graybill, W. W. Destler, Y. Carmel, and M. C. Chang, "A high power backward wave oscillator driven by a relativistic electron beam," *IEEE Trans. Plasma Sci.*, vol. PS-13, pp. 559–562, Dec. 1985.
- [3] Y. Carmel, K. Minami, R. A. Kehs, W. W. Destler, V. L. Granatstein, D. K. Abe, and W. L. Lou, "Demonstration of efficiency enhancement in a high power backward wave oscillator by plasma injection," *Phys. Rev. Lett.*, vol. 62, pp. 2389–2392, May 1989.
- [4] J. A. Swegle, R. A. Anderson, J. F. Camacho, B. R. Poole, M. A. Rhodes, E. T. Rosenbury, and D. L. Shaeffer, "Scaling studies and time-resolved microwave measurements on a relativistic backward-wave oscillator," *IEEE Trans. Plasma Sci.*, vol. 21, pp. 714–724, Dec. 1993.
- [5] X. Zhai, E. Garate, R. Prohaska, G. Benford, and A. Fisher, "Experimental Study of a plasma-filled backward wave oscillator," *IEEE Trans. Plasma Sci.*, vol. 21, pp. 142–150, Feb. 1993.
- [6] D. K. Abe, "Experimental studies of overmoded high power microwave generators," Ph.D. dissertation, Univ. of Maryland, 1992 (unpublished).
- [7] S. P. Bugaev *et al.*, "Investigation of millimeter wavelength range relativistic diffraction generator," *IEEE Trans. Plasma Sci.*, vol. 18, pp. 518–524, June 1990.
- [8] ———, "Relativistic multiwave Cerenkov generators," *IEEE Trans. Plasma Sci.*, vol. 18, pp. 525–536, June 1990.
- [9] K. Halbach and R. F. Holsinger, "SUPERFISH—A computer program for evaluation of RF cavities with cylindrical symmetry," *Particle Accelerator*, vol. 7, pp. 213–222, 1976.
- [10] U. Van Rienen and T. Weiland, "Triangular discretization method for the evaluation of rf fields in waveguides and cylindrically symmetric cavities," *Particle Accelerators*, vol. 20, pp. 239–265, 1987.
- [11] R. K. Cooper and M. E. Jones, "The physics of codes," in *High-Brightness Accelerators*, A. K. Hyder, M. F. Rose, and A. H. Guenter, Eds. New York: Plenum, 1988, pp. 233–255.
- [12] A. Bromborsky and B. Ruth, "Calculation of  $TM_{0n}$  dispersion relations in a corrugated cylindrical waveguides," *IEEE Trans. Microwave Theory Tech.*, vol. MTT-32, pp. 600–605, June 1984.
- [13] J. A. Swegle *et al.*, "Backward wave oscillators with rippled wall resonator," *Phys. Fluids*, vol. 28, pp. 2882–2894, 1985.
- [14] K. Minami *et al.*, "Linear theory of electromagnetic wave generation in a plasma-loaded corrugated-wall resonator," *IEEE Trans. Plasma Sci.*, vol. 18, pp. 537–545, June 1990.
- [15] M. M. Ali *et al.*, "Linear analysis of a localized plasma loaded backward wave oscillator driven by an annular intense relativistic electron beam," *J. Phys. Soc. Japan*, vol. 60, pp. 2655–2664, Aug. 1991.
- [16] M. M. Ali, K. Ogura, K. Minami, T. Watanabe, W. W. Destler, and V. L. Granatstein, "Linear analysis of a plasma-filled backward wave oscillator," *Phys. Fluids*, vol. B4, pp. 1023–1032, Apr. 1992.

- [17] R. Sawhney, K. P. Maheshwari, and Y. Choyal, "Effect of plasma on efficiency enhancement in a high-power relativistic backward wave oscillator," *IEEE Trans. Plasma Sci.*, vol. 21, pp. 609-613, Dec. 1993.
- [18] K. Ogura, K. Minami, M. M. Ali, K. Kan, T. Nomura, Y. Aiba, A. Sugawara, and T. Watanabe, "Analysis of field lines and Poynting vectors in corrugated wall waveguides," *J. Phys. Soc. Japan*, vol. 61, pp. 3966-3975, Nov. 1992.
- [19] L. C. Maier, Jr., and J. C. Slater, "Field strength measurement in resonant cavities," *J. Appl. Phys.*, vol. 23, pp. 68-77, Jan. 1952.
- [20] W. Main, Y. Carmel, K. Ogura, J. Weaver, G. S. Nusinovich, J. P. Tate, J. Rodgers, A. Bromborsky, S. Watanabe, M. R. Amin, K. Minami, W. W. Destler, and V. L. Granatstein, "The electromagnetic properties of open and closed overmoded slow wave resonators for interaction with relativistic electron beams," *IEEE Trans. Plasma Sci.*, vol. 22, no. 2, pp. 566-577, Oct. 1994.



**Md. Ruhul Amin** was born in Rangpur, Bangladesh, in 1959. He received the B.Sc. (EEE) degree from the University of Rajshahi in 1984, and the M.Sc. (EEE) degree from Bangladesh University of Engineering and Technology, Dhaka, Bangladesh, in 1987.

He is now on sabbatical from Bangladesh Institute of Technology, Rajshahi, where he is an assistant professor in the Electrical and Electronic Engineering Department. He is presently working toward the Ph.D. degree at the Graduate School of Science and Technology, Niigata University, Japan. His research interests include theoretical and experimental investigations of high-power microwave devices, and semiconductor power electronic drives.

Mr. Amin is a member of the Institution of Engineers Bangladesh (IEB) and the Physical Society of Japan.

**H. Kitamura**, photograph and biography not available at time of publication.

**K. Minami**, photograph and biography not available at time of publication.

**T. Watanabe**, photograph and biography not available at time of publication.

**Y. Carmel**, (S'66-M'69-S'71-M'74-SM'90) photograph and biography not available at time of publication.

**W. Main**, (M'93) photograph and biography not available at time of publication.

**J. Weaver**, photograph and biography not available at time of publication.

**W. W. Destler**, (M'84-SM'90-F'92) photograph and biography not available at time of publication.

**V. L. Granatstein**, (S'59-M'64-M'84-SM'86-F'92) photograph and biography not available at time of publication.

**K. Ogura**, photograph and biography not available at time of publication.